Short Fatigue Crack Growth And Durability Modeling Of Resistance Spot Welded 5754 And 6111

by

Vir S. Nirankari

A dissertation submitted in partial fulfillment
of the requirements for the degree of
Doctor of Philosophy
(Materials Science and Engineering)
in The University of Michigan
2017

Doctoral Committee:

Professor John E. Allison, Chair
Professor Pingsha Dong
Professor J. Wayne Jones
Dr. Mei Li, Ford Motor Company
Professor Alan Taub

Acknowledgements

First and foremost, I would like to express my gratitude to my academic advisor and committee chair, Professor John Allison, for his support and guidance, without which this thesis would not have been possible. I would also like to thank the rest of my committee members, Professor J. Wayne Jones, Professor Pingsha Dong, Professor Alan Taub and Dr. Mei Li for their insights and helpful critiques.

In addition I wish to thank our collaborators at the Ford Motor Company Research and Innovation Center. Dr. Bita Ghaffari, Dr. Elizabeth Hetrick, and Dr. Xuming Su provided the materials used in this research along with countless helpful discussions. Sainan Wu and Li Huang for conversations and advice with spot welds and finite element analysis. Special thanks also to Dr. Steven Yalisove, for giving me permission to utilize the femtosecond laser equipment.

I would also like to thank my numerous colleagues, all of whom who provided support, thoughtful discussions, camaraderie and encouragement that have made this work more pleasant and productive: Dr. Tracy Berman, Dr. Michael Kimiecik, Dr. Jared Tracy, Dr. Jiashi Miao, Dr. Xianfeng Ma, Dr. Alfred Okello, Dr. Jason Geathers, Dr. Zhe Chen, Dr. Qianying Shi, Dr. Surendra Makineni, Erin Deda, Jacob Adams, Sinsar Hsie, Aeriel Murphy, Maya Nath, Anna Trump and Zhihua Huang.

I would also like to thank my family and friends for their love, support encouragement, and prayers. All of this would have been impossible without you.

Finally, I gratefully acknowledge the funding of this work from Ford Motor Company. This work was supported by the University of Michigan – Ford Alliance Program. I would like to thank the Horace H. Rackham Graduate School for financial travel awards that supported travel to conferences throughout my work. A final thanks to Dr. Shaopin Song for his tireless work to help me with finite element analysis, Dr. Michael Abere and Rico Cahyadi for helping me with femtosecond notching, John Lasecki for his help in the lab and MTS frames, and Marv Cressey and Kent Pruss for helping me with sample fabrication.

Table of Contents

List of Tables

List of Figures

Abstract

Short Fatigue Crack Growth And Durability Modeling Of Resistance Spot Welded 5754 And 6111 Aluminum Alloys

By

Vir S. Nirankari

Chair: John E. Allison

The growing demand for more fuel-efficient vehicles to reduce energy consumption and air pollution is a challenge for the automotive industry. Aluminum alloys are of interest due to their favorable cost, density, strength, and production methods, leading to improved fuel efficiency and exhaust emissions when such alloys are used to reduce the weight of automobiles and trucks. The alloys 5754 (Al-3Mg) and 6111 (Al-1Mg-1Si) are used as inner and outer automotive body panels, respectively, and overlapping sheets are frequently joined together using resistance spot welding. Resistance spot welding (RSW) is one of the most widespread and practical joining techniques in the automotive industry for sheet metal components. Despite its widespread use, little is known about the propagation behavior of short cracks within the spot welds. This investigation provides insight into the factors affecting propagation of physically

short cracks within the spot weld regime and applies that information to develop a new approach for modeling joint durability.

Short crack propagation rates in the parent sheet materials were found to be similar for the two aluminum alloys. However, crack propagation rates in the RSW regions were observed to be as much as 100x faster than the parent alloys. This was determined to be due to the interactions of cracks with pores that form in the weld fusion zone. A unified, dislocation based short crack model was modified to account for this effect. The short crack data was incorporated into an analytical master fatigue life relationship for predicting the lifetime of spot-welded components using a structural stress methodology. The durability model consists of finite element analysis calculations of structural stresses, adjusted short fatigue growth relationships and a calibration procedure based on fatigue lifetime data of aluminum RSW joints. This methodology was validated by application to experimentally determined fatigue lives of lap-shear joints in a wide variety of weld and sheet geometries in both alloys. Implementation into a full scale vehicle model can aid in the optimization of the size, location and number of RSW joints and enable weld process optimization via Integrated Computational Materials Engineering (ICME).

Chapter 1

Introduction

The growing demand for more fuel-efficient vehicles to reduce energy consumption and air pollution is a challenge for the automotive industry. Aluminum alloys are of interest due to their favorable cost, density, strength, and production methods [1], leading to improved fuel efficiency and exhaust emissions [2] when such alloys are used to reduce the weight of automobiles and trucks. The aluminum alloys 5754 (Al-3Mg alloy) and 6111 (Al-1Mg-1Si alloy) are of particular interest as inner and outer automotive body panels, respectively.

Resistance spot welding (RSW) is one of the most widespread and practical joining methods for joining sheet metal assemblies in the automotive industry. RSW is a joining process for thin metal sheets during which, in contrast to other welding processes, no filler metals or fluxes are used. Instead, pressure exerted by electrodes joins the contacting metal surfaces utilizing heat obtained from electrical resistance to the electrical current flow [3]. Over the years, traditional RSW processes have been successfully used for various steel grades to deliver high-quality joints [4]. Typically, a modern vehicle in North America contains between 4000 and 5000 spot welds and the joint quality can dramatically alter the structural performance. Because spot weld joints provide localized connection, and thus lead to high stress concentration in the joined plates, any improper design may result in excessively high stresses and premature failure

[5]. When a vehicle is operating, these spot welds will endure fatigue loading as a result of cyclic loading and vibrations [6] and thus an understanding of this failure mechanism is imperative.

Fatigue cracks may initiate from micropores or inclusions of the microstructural scale within the welded joint, leading to theoretical fatigue lives that are underestimated by traditional fatigue life calculations. Furthermore, the phenomena of 'eyebrow' cracking (crack growth through the edge of the spot weld into the parent sheet material) necessitates the use of a durability model to predict failure for future welded components of varying geometry for weld optimization. Due to the mass production of spot welds, optimizing the location and number of overall spot welds can lead to a tremendous amount of savings [7]. Additionally, application of a unifying short crack model proposed by Shyam et al. [8], which depends on a few easily obtainable mechanical properties, could be utilized with other design approaches to further predict and optimize material welded components via Integrated Computational Materials Engineering (ICME).

There are three objectives in this research work. First, this study seeks to understand the behavior of physically short fatigue cracks in the parent and spot welded 5754 and 6111 aluminum alloys. Second, the ability of the unifying model to account for welding imperfections that can lead to lower lifetimes is investigated and adjusted to broaden its potential applicability. The third objective is to model the eyebrow failure phenomenon such that failure of future spot welded joints with different geometries and alloying variables can be predicted.

Chapter 2 provides a review of the literature that is relevant to the present work, including previous short crack and durability models. In Chapter 3, the experimental methods used to investigate the short crack growth behavior is described. The short fatigue crack growth

behavior of aluminum 5754 and 6111 and its spot welded components are discussed in Chapter 4, along with adjustments to the unifying parameter to account for welding porosity. A structural stress based master fatigue life curve is constructed and discussed in Chapter 5. Finally, conclusions and recommendations for future work are detailed in Chapter 6.

References

[1] Miller W., Zhuang L, Bottema J, Wittebrood A., De Smet P, Haszler A, et al. Recent development in aluminium alloys for the automotive industry. Mater Sci Eng A 2000;280:37–49. doi:10.1016/S0921-5093(99)00653-X.

[2] Pereira AM, Ferreira JM, Loureiro A, Costa JDM, Bártolo PJ. Effect of process parameters on the strength of resistance spot welds in 6082-T6 aluminium alloy. Mater Des 2010;31:2454–63. doi:10.1016/j.matdes.2009.11.052.

[3] Florea RS, Solanki KN, Bammann DJ, Baird JC, Jordon JB, Castanier MP. Resistance spot welding of 6061-T6 aluminum: Failure loads and deformation. Mater Des 2012;34:624–30. doi:10.1016/j.matdes.2011.05.017.

[4] Wu SN, Ghaffari B, Hetrick E, Li M, Jia ZH, Liu Q. Microstructure characterization and quasi-static failure behavior of resistance spot welds of AA6111-T4 aluminum alloy. Trans Nonferrous Met Soc China (English Ed 2014;24:3879–85. doi:10.1016/S1003-6326(14)63546-9.

[5] Ertas AH, Sonmez FO. Design optimization of spot-welded plates for maximum fatigue life. Finite Elem Anal Des 2011;47:413–23. doi:10.1016/j.finel.2010.11.003.

[6] Chang B, Du D, Sui B, Zhou Y. Effect of forging force on fatigue behavior of spot welded joints of aluminum alloy 5182. J 2007.

[7] Zhang Y, Taylor D. Optimization of spot-welded structures. Finite Elem Anal Des 2001;37:1013–22. doi:10.1016/S0168-874X(01)00046-4.

[8] Shyam A, Allison JE, Szczepanski CJ, Pollock TM, Jones JW. Small fatigue crack growth in metallic materials: A model and its application to engineering alloys. Acta Mater 2007;55:6606–16. doi:10.1016/j.actamat.2007.08.022.

Chapter 2

Literature Review

In this chapter, a review of the literature relevant to understanding the objectives, the approach and the results of this study in this dissertation is provided. Section 2.1 characterizes the two alloys studied in this dissertation, Al 5754 and Al 6111, and covers the spot welding process. A review of the anomalous nature of short cracks and modeling of this behavior is presented in Section 2.2 and Section 2.3. The effect of porosity on fatigue life and short crack growth is discussed in Section 2.4. The failure mode of lap-shear specimens is covered in Section 2.5. Finally, structural stress theory and methodology to aid in the creation of master fatigue life curve is covered in Section 2.6.

2.1 Aluminum Alloys 5754 And 6111 And The Resistance Spot Welding Process

Aluminum, is the second most abundant metallic element in earth's crust [1], has a wide range of engineering applications due to its combination of cost, strength and weight. Its density (ρ = 2.7 g/cm^3) is approximately a third that of steel (ρ = 7.75 to 8.05 g/cm^3). Pure aluminum is quite soft (σ_{YS} = 7 to 11 MPa [2]), limiting its commercial usefulness, and thus alloying is employed to improve its strength. The primarily alloying elements are copper, manganese, silicon, magnesium, or zinc. These strengthening provided by these elements are primarily

through: (a) solid solution hardening (non-heat treatable alloys) or (b) precipitation hardening (heat treatable alloys) [3].

Two wrought sheet alloys, Al 5754 (Al-3Mg) a non-heat treatable alloy, and Al 6111 (A-1Mg-1Si) a heat-treatable alloy, are of particular interest to the automotive industry to be used as inner and outer body panels, respectively. These alloys are joined together using a process known as resistance spot welding (RSW). The following sections describe each of these alloys and the resistance spot welding procedure used to fabricate joints.

2.1.1 Aluminum Alloy 5754

The non-heat treatable alloy 5754 (Al-3Mg) are used in the automotive industry for inner structural panels where strength, good deep drawing and stretch behavior are important issues [4]. The 5000 aluminum family is desirable for industrial applications because they provide an excellent balance of solid-solution strengthening of Mg in the Al matrix, appreciable ductility during cold working, and high weldability [5]. For 5754, the Mg content is optimized for satisfactory mechanical properties and low susceptibility to stress corrosion cracking [6].

For this alloy, the primary hardening mechanisms are solid solution strengthening, grain size strengthening and strain hardening. Magnesium, the primary alloying element, provides the highest degree of hardening from solid solution strengthening. These alloys also contain minor additions of Cr, Mn and Ti, which hinder grain growth during heating and assist in grain refinement during rolling [1]. Dispersed Mn-containing particles (Al_6Mn) are present in several 5000 series aluminum alloys and have been determined to be un-dissolvable in the solid state, making it effective at preventing high temperature grain growth in solid state welding applications [7]. Additions of Fe and Si form intermetallics, which have been found to serve as

crack initiation sites. Small amounts of Cu are also added for additional solid solution strengthening [8].

These alloys are also hardened through strain hardening. Processing through cold rolling, drawing or stretching is an effective means of increasing the strength of these alloys. The increase in strength usually comes at the cost of ductility, and reduced formability in operations such as bending and drawing. For those operations, the material is partially annealed or stabilized to enhance the formability in those materials. The microstructure of several 5000 series alloys, displayed in Figure 2.2, is primarily characterized by elongated grains in the ND-RD and ND-TD planes due to the rolling processes.

This alloy has traditionally displayed the serrated (discontinuous) yielding effect [9–11], also known as the dynamic strain aging (DSA). During deformation, solute atoms preferentially segregate into the stress field around the dislocations, restricting the overall dislocation motion [12]. This leads to the observation of "jerky" motion seen in a stress-strain curve. Studies of this effect on the fatigue behavior has produced inconsistent conclusions. Weisse et al. [13] , in a low cycle fatigue study of low carbon steel, that the effect of DSA enhances the fatigue life. Srinivasan et al. [14] found in 316L stainless steel that DSA caused a reduction in fatigue life due to cyclic hardening effects. Babu et al. [15] has suggested that, in P91 steel, DSA may lead to an increase in the fatigue crack growth threshold.

2.1.2 Aluminum Alloy 6111

The heat treatable alloy 6111 (Al-1Mg-1Si), developed by Alcan [16], is of interest to the automotive industry for outer body panels, where high strength, dent resistance and shock absorption are required [17]. This family of aluminum alloys is primarily alloyed with

magnesium and silicon. Alloying with silicon reduces the melting temperature and improves the overall fluidity during slab casting. Alloying with magnesium results in an increase in material strength through solid solution strengthening and improves the strain hardenability. The addition of magnesium and silicon to aluminum produces the compound magnesium-silicide (Mg_2Si) [18]. The use of copper provides an increase in solid solution strengthening [10]. This alloy is strengthened through precipitation of several metastable phases produced through artificial aging. The precipitation sequence for 6000 series aluminum is known to depend on the Mg to Si ratio and the concentration of Cu present in the system [19–21]. Research specifically on alloy 6111 [22] has shown a precipitation sequence of:

$$\text{Clusters / GP zones} \rightarrow \beta'' + Q' \rightarrow \text{equilibrium } Q + Mg_2Si$$

In the context of this research, the aging times of Al 6111 that are being investigated are the T4 (solution heat treated and naturally aged to a substantially stable condition), paint baked (PB: artificial aging at 180 ° C for 30 minutes) and the overaged (OA: artificial aging at 210 ° C for 12 hours). Esmaeili et al. [17] found, for these heat treatments, that the β" (fine needle shaped) phase is the main strengthening phase of AA6111. β" precipitates are needle-shaped lying along the <100> direction and have a composition of Mg_5Si_6 [23]. The paint bake heat treatment is of particular interest, as a similar heat treatment is used to expedite the drying and curing process of painted automotive structures [24]. Standard microstructures of other 6000 series aluminum alloys, presented in Figure 2.3, are primarily characterized by elongated grains in the ND-RD and ND-TD planes due to the rolling processes

In the context of this work, different aging conditions were examined in order to understand the effect of slip character on short fatigue propagation behavior. It has been noted that the ability of a precipitate to shear is the main determinant in slip character [10,17,25,26],

and can affect fatigue crack initiation and propagation. Zaiken et al. [27] have noted that, for an underaged microstructure, the resulting crack morphology follows that of coarse planar slip, with a low number of slip systems being activated yielding a heterogeneous crack morphology. They have also noted that, conversely, for an overaged microstructure, the resulting deformation follows a homogenous morphology due to the activation of multiple slip planes with a common slip direction.

An alternate method for homogenizing slip is thru generation of dispersoids during high temperature processing (e.g. solution treatment). Mn-containing dispersoids such as Al_4Mn or $Al–Al_{12}Mn_3S$ are introduced primarily to inhibit recrystallization and control grain growth. Edwards et al. [28], however, have found that in Al-Mg-Si-Mn alloys, the slip character is also affected by the presence of manganese bearing dispersoids. These dispersoids result in more homogenous deformation and reduction in fatigue crack growth rates and have been found to be incoherent with the matrix. Thus, a higher concentration of dispersoids increases obstacles that cannot be sheared through dislocation motion [29,30]. This changes the slip character from heterogeneous slip in the case of the underaged alloys to homogenous slip.

2.1.3 Resistance Spot Welding

Resistance spot welding (RSW) is a process of joining sheet metal components through the fusion at the interface between the components. It is one of the most widespread and practical methods of sheet joining in a variety of industries due to its ease of automation [31]. Over the years, traditional RSW processes have been successfully used for various steel grades to deliver high-quality joints [32]. A typical steel vehicle in North America contains between 4,000 and 5,000 spot welds [33,34].

During the resistance spot welding operation, the metal sheets to be joined are held together under pressure exerted by two copper electrodes (Figure 2.4 (a)). Once the desired clamping force has been reached, an electrical current is passed through between the electrodes. The resistance offered by the sheets to the current (based on Joule's law) generates thermal energy. The concentration of heat melts the material in the middle of the sheet stack-up (Figure 2.4 (b)). Once the current is removed, the melted material re-solidifies, forming a weld nugget that joins the sheet metal together (Figure 2.4 (c)) [35]. The resistance and temperature distribution present in the sheets is displayed schematically in Figure 2.5. For this type of welding, shielding gases are not needed because air is squeezed out of the interface between sheets due to the electrode force [36]. The combination of welding parameters (electrode shape, electrode pressure, welding current, welding time) are responsible for generating the weld size and properties. The spot weld displays a cast microstructure: an equiaxed dendritic region in the weld center and a columnar dendritic region at the weld edge. Representative EBSD maps of the different regions for a 6061-T6 aluminum spot weld is displayed in Figure 2.6.

Due to the thermomechanical and metallurgical factors present in the creation of a spot weld, there are inherent discontinuities that have an effect on the fatigue properties of the RSW joints. There may be external discontinuities such as: excessive indentation (defined as greater than 30% of the stack-up thickness [36]) or expulsion (ejection of molten material generally due to a large amount of thermal energy) [6,35]. Internal discontinuities, mainly porosity, have been found to have a significant effect on fatigue behavior of spot welds. Amar et al. [37] has characterized the types of porosity associated with cast systems as two portions: shrinkage porosity and gas porosity. Shrinkage porosity is due to cooling at both the liquid and solid states in the weld, generating a reduction in volume with Al shrinking more so in the solid state (solid

Al is ~7.1% denser than liquid Al [38]). Gas porosity is the formation of bubbles within the casting, due to gaseous pressure in the nugget at a liquid, after it has cooled. They occur because most liquid materials can hold a large amount of dissolved gas, but the solid form of the same material cannot, and thus pores are formed because gases are far less soluble in solid metals than in liquid metals [39]. For aluminum, the dissolved gas is usually hydrogen that comes from dissolved water vapor. In the aluminum alloys present in this study, Mg has been found to increase the hydrogen solubility in the molten state. Thus, gas porosity is more predominant in 5754 spot welds than the 6111 spot welds.

2.2 Behavior Of Short Cracks

The basis for the quantification of failure from fracture is traditionally defined through fatigue crack growth measurements. The basis for this theory begins with linear elastic fracture mechanics theory (LEFM), which provides the empirical framework for describing the fatigue crack growth phenomenon [40]. LEFM characterizes crack growth in three stages (see Figure 2.7): (1) the threshold region, or the region that crack propagation can be expected to first occur; (2) the Paris region, where stable macroscopic crack growth occurs, and (3) the fracture region, where the fatigue crack growth rates will accelerate as they approach instability and eventual fracture occurs.

The Paris region is where the applications of LEFM concepts are applied. In the simplest form, the crack growth rate, da/dN (crack extension per cycle of applied load), is related to the stress intensity factor, ΔK (the driving force for crack propagation) by a power law relationship first proposed by Paris et al. [41,42].

[2.1] $\frac{da}{dN} = C(\Delta K)^m$

The phenomenon of "short" fatigue cracks was first investigated by Pearson [43], who observed that short crack growth rates and long crack growth rates did not correlate using LEFM theory. In general short cracks are defined in one of the following ways [40]:

a) Microstructurally short: Cracks are short compared to microstructural dimensions (such as the grain size)
b) Mechanically short: Cracks are short compared to the scale of local plasticity
c) Physically short: Cracks are simply physically short (< 1 – 2 mm)
d) Chemically short: Cracks can be up to 10 mm long, depending on the crack-tip environment

This dissertation work focuses on physically short cracks. Since Pearson's work, other researchers [44–47] have studied short cracks using fracture mechanics and have found that short cracks can grow at higher crack growth rates than long cracks under the same ΔK and can grow at ΔK values below the traditional threshold ("small crack effect"). A schematic fatigue crack growth rate da/dN vs. ΔK plot that presents this phenomenon is displayed in Figure 2.8.

The cause of the short crack effect is not well understood. Suggested explanations have been proposed to account for the anomalous behavior displayed of short cracks: crack closure, breakdown in microstructural similitude and plasticity effects [40]. In long cracks, crack closure reduces the driving force due to the crack remaining in a closed position despite being under the effect of a tensile force. Various mechanisms for closure have been identified, including roughness, plasticity and oxide induced closure [48]. Short cracks, however, do not experience the same levels of crack closure.

Another explanation for the observed variability of crack growth rates for short cracks growing in the near threshold regime is microstructure dissimilitude, in which the crack front of short cracks does not sample enough grains to be representative of the average material properties. In such cases, the properties of the individual grain in which the crack is growing become critical to crack growth behavior. As a result, short cracks exhibit fluctuating (acceleration/retardation) propagation behavior, due to the reduction of the crack tip driving force when obstacles such as grain boundaries are encountered [47,49,50].

Small scale yielding ahead of the crack tip is generally assumed in using the linear elastic parameter ΔK. This assumption is violated for small cracks when the size of the plastic zone ahead of the crack tip is comparable to the size of the crack. The violation of small scale yielding makes ΔK an inappropriate parameter for correlation small crack growth, and the increased plasticity experienced at higher stress levels can partially account for the influence of stress on small crack growth rates.

2.3 Short Crack Models

Designing structural components against fatigue failure remains a crucial engineering challenge [40]. The ability to better understand the cause behind fatigue failure would lead to an improved understanding of how to better design components. Furthermore, accurate prediction methods of component lifetime would lead to improved part inspection and renewal procedures. The growth of small fatigue cracks, however, is generally not amenable to characterization by LEFM theory [51]. The challenge in establishing a uniform short crack growth law, however, is that the fatigue phenomenon is strongly sensitive to microstructure. Researchers over the years have made advances to better predict the behavior of short cracks through LEFM adjustments,

dislocation mechanics and atomistic models. Several of these modeling approaches for short cracks will be discussed further.

The original and most significant crack growth model is the classic LEFM model proposed by Paris et al. [41,42] (Equation [2.1). This law has been found applicable for a wide spectrum of materials and is still widely used in industrial settings to provide engineers with quick estimations with relatively simple measurable parameters [52]. Due to the general applicability of the Paris law, many researchers have determined analogous relationships to estimate the effect of microstructure by accounting for crack deflection or crack tip radius. For example, Suresh [53,54] rationalized the effect of microstructure on the basis of crack path tortuosity. The author posited that the lower observed long crack growth rates for tortuous cracks compared to flatter crack paths (i.e. underaged vs. overaged cracks [55]) was due to crack path deviations from the macroscopic crack plane (see Figure 2.9) and required greater ΔK to propagate:

$$[2.2]\ \frac{da}{dN} = \left\{\frac{D\ cos\theta + S}{D+S}\right\}\left(\frac{da}{dN}\right)_{long\ crack}$$

While this model and other LEFM model adjustments provide better correlations for fatigue crack growth data, they still do not account for the lack of small scale yielding. Plastic accumulation is well known to have a significant influence on crack advancement, and it has been quantified that for small cracks, the ratio of the plastic zone size to the crack size is on the order of unity, while it is much less than 1 for large cracks [56].

In order to fully account for the effect of microstructure on short cracks, the role of microstructural barriers to plastic flow needs to be examined. This would require plastic deformation mechanisms to be considered. These mechanisms are governed by dislocation-slip

interactions [57]. It is well known that fatigue crack growth is governed by slip phenomena and thus accounting for the variables controlling dislocation-slip interactions should result in more accurate short crack growth models. Rice et al. [58] determined that slip emission at a crack tip leaves a permanent displacement equal to the collective Burger's vectors. Bilby, Cottrell and Swinden [59] developed a concept of slip distribution at a crack tip (the so-called BCS model - Figure 2.10). The authors postulated that, for a crack in a thin sheet under uniaxial tension, the edge dislocation density at the crack tip is sufficiently high enough to be represented by a continuous distribution function, B(x), as defined by Weertman [60]:

$$[2.3]\ B(x) = \frac{4\sigma_{YS}(1-\upsilon^2)}{\pi E} ln \left| \frac{x\sqrt{c^2-a^2}+a\sqrt{c^2-a^2}}{x\sqrt{c^2-a^2}-a\sqrt{c^2-a^2}} \right|$$

Where x = a represents the crack tip and x = c represent the tip of the plastic zone. In the plastic zone, the sum of the applied and dislocation field stresses is found to be the tensile yield stress, σ_{YS} of the material for uniaxial mode I loading [61]. The monotonic crack tip opening displacement, ϕ_m, based on the BCS theory is derived by integrating Equation [2.1 from the edge of the crack tip (x = a) to the edge of the monotonic plastic zone (x = c):

$$[2.4]\ \phi_m = \frac{8\sigma_{YS}(1-\nu^2)a}{\pi E} \ln\left(\sec\left(\frac{\pi\sigma_{max}}{2\sigma_{YS}}\right)\right)$$

This parameter accounts for the emission of slip due to uniaxial tension and can be correlated to the fatigue damage process. In addition to the monotonic plastic zone, there is a region of reverse flow at the edge of the crack tip denoted at the cyclic plastic zone [62]. In the case of reverse flow, it was rationalized that σ_{max} becomes $\Delta\sigma_{app} = \sigma_{max}(1\text{-}R)$ and σ_{YS} becomes $2\sigma_{YS}$ [61]. Substituting these parameters in Equation [2.4 results in the cyclic crack tip opening displacement, ϕ_c:

[2.5] $\phi_c = \frac{16\sigma_{YS}(1-\nu^2)a}{\pi E} \ln\left(\sec\left(\frac{\pi\sigma_{max}(1-R)}{4\sigma_{YS}}\right)\right)$

The crack tip opening displacement terms utilize dislocation dynamics in the plastic zone of the crack tip to represent the local crack tip strain, and are thus a more complete correlating parameter to describe short crack growth behavior for a variety of alloys.

Fatigue crack growth has been postulated [63,64] to be depend on two synergistic processes: the accumulation of irreversible damage at the crack tip, and crack extension through the decohesion at the crack tip due to the strain energy inside the monotonic plastic zone.

[2.6] $\frac{da}{dN} = \mathrm{f}(monotonic\ damage, cyclic\ damage)$

A unified short crack model proposed by Shyam et al. [65] is designed to account for these two effects by relating the short crack growth rate to a linear relationship that is the product of the monotonic (crack extension) and cyclic (damage accumulation) crack tip opening displacements (Equations [2.4 and [2.5):

[2.7] $\frac{da}{dN} = \mu\phi_m\phi_c\sigma_{YS}$

Where the fitting parameter, μ, is defined as the damage susceptibility parameter that describes the rate at which damage accumulation and crack advance can occur in a given microstructure ahead of the crack tip, and is comprised of the slip irreversibility factor, f, (defined as the fraction of dislocations that contribute to extension of a fatigue crack [61]), a geometric scaling factor, α, and the critical crack damage to cause crack extension, ϕ_{cr}.

[2.8] $\mu = \frac{f\alpha}{\phi_{cr}}$

The assumptions are made such that α is approximately constant for most structural metals and ϕ_{cr} is constant throughout the crack growth life and therefore, the critical parameter μ is the slip irreversibility.

In order to test this unified model, short crack growth testing was performed on cast A356 and W319 aluminum at R = -1, 0.1, 0.3 and f = 30Hz, Ti-6246 at R = 0.05 and f = 20 kHz and Rene' 88 superalloy at R = 0.05 and f = 20 kHz. Each material system has a wide range of microstructures and strengths, and was tested at differing load ratios and frequencies. da/dN was plotted against ΔK, presented in Figure 2.11. As expected, the difference short crack growth rates across different alloy systems is considerable when utilizing ΔK as a correlating parameter. Plotting da/dN vs. the unified parameter (Equation [2.7), as displayed in Figure 2.12, shows a much more closely matching trend between the alloys, despite a difference in microstructure, mechanical properties, and loading conditions. Thus it can be inferred that the unified parameter, on average, accounts in a comprehensive way for microstructure, alloy, R-ratio and stress level effects on the short crack data for a wide range of engineering alloys.

While the unified parameter does not account for the observed short crack behavior of cessation at grain boundaries [50,66–68] due to slip blockage, it is expected to predict the average growth rates over the short crack regime. Furthermore, compared to other models that utilize dislocation mechanics, application of the separate roles of monotonic and cyclic plasticity have not been considered. This model can be used in practical applications as an initial reference for the short crack response of existing engineering alloys or to aid in the design of new structural materials and can be applied to other applications through Integrated Computational Materials Engineering (ICME).

2.4 Effect Of Porosity

Porosity is a major microstructural feature controlling fatigue properties because it introduces very high stress concentrations within fatigue specimens. In general, porosity has been found to override any influence from other factors such as oxides, eutectic particles and slip bands [69] on fatigue life in cast aluminum components. In fatigue lifetime studies, porosity serves as primary sites for fatigue crack initiation [70] and reduces the time for crack initiation [71,72]. Ammar et al [37] investigated cast Al-Si alloys and suggested that the pores reduce the time for crack initiation through an increase in the stress concentration in the matrix adjacent to the pore and that the majority of fatigue life is comprised of fatigue crack propagation. The implication is that porosity reduces fatigue resistance. In a study of cast W319-T6 Al [73], a comparison of hot isostatically pressed (HIP) specimens, a process which greatly lowers porosity, compared to non-HIP specimens shows the presence of porosity reduces fatigue lifetimes by a factor of 10.

Literature on the effect of porosity on fatigue crack growth remain limited. In the same study by Ammar et al. [37] it was also found that a fracture plane containing a high fraction of small pores resulted in higher life than a fracture surface containing low volume fraction of large pores. It was posited that this was due to the crack having to travel through the matrix from pore to pore, where each pore is not a significant stress concentrator, while the higher stress concentration provided by the larger pore provides enough increase in the crack growth rate. Wang et al. [71] investigated the fracture surfaces of cast A356-T6 aluminum, found high fractions of porosity on the fracture surface, particularly the overload region, and attributed this to the fact that the fatigue crack always seeks the weakest path and porosity provides an easy

path for crack propagation. Gerard et al. [74], in a study of the effect of porosity in powder metallurgy titanium, suggested that short crack growth rates are temporarily accelerated by the plastic zone adjacent to pores. The accelerated growth was due to the crack front encountering a defect that, on a local scale, generates a plastic zone that is much greater than the nominal strain amplitude in the matrix. Moffet [75] investigated Al-Si castings with X-ray computed tomography on Al-Si castings and found that pores played a dominant role in short fatigue crack propagation. It was suggested that pores provide a weak path for fatigue cracks to propagate, and that when a fatigue crack approaches a pore it is "attracted" towards it, as long as it is beneficial in terms of the crack driving force. Gall et al. [76] believed that porosity has an "indirect" influence on fatigue crack growth rates. They found that, under nominally identical loading conditions, isolated microstructurally small cracks grew, on average, two orders of magnitude faster in a sample containing a higher fraction of porosity. It was suggested that porosity enhances the nominal stress field experienced by the microstructurally small cracks and this enhancement led to relatively higher small crack growth rate even in the absence of explicit interaction between the small cracks and pores.

2.5 Lap-Shear Specimen Failure Modes

In service, spot welded joints experience both tensile and bending stresses, and this stress state coupled with joint geometries leads to stress concentrations and eventual fatigue failure. Three competing modes of fatigue failure have been observed: interfacial failure (fracture via crack propagation through the weld nugget), nugget pullout (the weld nugget is completely pulled out from one of the metal sheets), [35,77] and eyebrow cracking. The dominant mode is dependent on the applied stress level and cyclic life.

For quasi-static and low cycle fatigue testing, the dominant failure modes are the interfacial failure and nugget pullout. For steels it has been observed that, for the highest applied stress levels and large nugget diameters, nugget pullout is the dominant failure mode. This failure mode is characterized by the weld nugget completely pulled out from one of the metal sheets, such that the weld nugget is left intact (see Figure 2.13 (a)). For this failure mode, it has been found that the strain in the base steel is greater than that developed at the weld interface [78].

At lower failure stresses and smaller nugget diameters in steel, it has been observed that interfacial failure is the dominant failure mechanism. Interfacial failure is defined as propagation through the weld nugget (see Figure 2.13 (b)) and is associated with a lower load carrying capacity and considerably less energy absorption capability, and is thus considered unsatisfactory and most industrial standards design to avoid this type of failure [77]. It should be noted that at the intermediary loads and nugget diameters, a combination of nugget pullout and interfacial failure could occur. In general though, any interfacial failure is indicative of poor weld manufacturing processes and necessitates adjustments to the spot welding parameters.

At moderate stress levels and lives of at least 10^4 cycles, the most commonly observed failure mode is eyebrow cracking. This type of failure is defined by crack initiation at the edge of the spot weld and propagation through the sheet thickness [79]. This failure mode occurs primarily due to the stress concentration provided by the "notch" that occurs due to sheet separation from indentation at the faying surface (Figure 2.14)

2.6 Structural Stress And The Master Fatigue Life Curve

In an effort to consolidate experimentally determined data to aid engineers in design through estimation, a number of techniques have been proposed for estimating fatigue life in welded structures [80]. The most prevalent technique for estimation of fatigue life in resistance spot weld is a method known as structural stress. The structural stress technique is a method to represent the local stress state at a region of interest within a structure. These are not the true stresses, but linearized stresses to simplify the complicated stress state [81–84] that exists through the volume of a welded region and the complex microstructure that forms in and around the spot weld. Stress linearization simplifies durability analysis and makes it tractable from a computational perspective on total structure durability analysis. The stress linearization process decomposes the stress state into two components: (1) a membrane component and (2) a bending component. Figure 2.15 details the process of stress linearization for a lap-shear specimen.

The aim of utilizing the structural stress approach is to generate a "master" fatigue life curve. This master curve methodology is based upon generating a single structural stress based fatigue life curve that represents the fatigue life of a large variety of welded structures with varying geometric and loading conditions in a robust calculation procedure [85].

The structural stress approach uses FEA to represent the weld nugget with rigid beam elements to transmit the forces and moments between the finite elements. Sheppard [81,86] was one of the first to propose this solution for spot-welded steel specimens with lap-shear geometry. Fatigue testing was performed on low-strength steel lap-shear specimens with different thicknesses, nugget diameters and load amplitudes. The load-life curve displayed different trends

for the different conditions, as expected. Plotting the fatigue lifetimes (normalized for R-ratio) versus the structural stress range, however, unified the data (see Figure 2.16).

Another prevalent structural stress methodology is a method proposed by Rupp et al. [82]. They observed that steel spot welded connections experienced local plastic deformation during the first few load cycles, and posited that using elasticity theory would not be effective as a correlating parameter. Thus, they determined the local structural stresses using beam, sheet and plate theory. With this approach, the spot weld was modeled as a rigid inclusion in an FE model, while the outer edges of the plate are treated as fixed (see Figure 2.17). The previous approaches, however, utilize stresses derived from reference points and extrapolate these to the points of interest and are thus fictitious stresses at the hot spot of interest.

Dong et al. [84,87,88] proposed a structural stress method, known as the Battelle method. The work in this dissertation uses this method as part of the master fatigue life curve creation (Chapter 5). In this structural stress FE approach, the spot weld is modeled with shell elements and rigid beams forming a spoke pattern, presented in Figure 2.18. In this method, the structural stresses are calculated from nodal forces and moments derived from linear elastic FEA. This methodology, in contrast to the previous structural stress approaches, is that the components satisfy the far-field equilibrium conditions and are considered real stresses. These nodal forces and moments, calculated in the global coordinate system, are then transferred into the local coordinate system. This is done because the structural stress is defined as components normal to the weld line of the spot weld. The next step is converting the nodal forces and moments to distributed forces through line forces and moments; that is, forces that are distributed along the weld line between the nodes (see Figure 2.19 (a) and (b)). These line forces and moments along the weld nugget periphery can then be used to quantify the structural stress components. The

Battelle method then utilizes fracture mechanics, assuming a Paris Law relationship to take into account the effects of loading mode and sheet thickness, suggesting that Mode I loading is the most critical mode for fatigue crack propagation for sheet metal in the through thickness direction. This methodology has proven successful for a variety of welded components, including spot welds.

Due to the fact that the structural stress technique is meant as an approximation, it is not without its limitations. These include the inability to accurately estimate large deflections from contacts between overlapping sheets [89], the inability to accurately account for material inhomogeneity, residual stress and other imperfections [88] as well as not accounting for varying crack initiation and propagation processes, such as crack closure [79]. Nevertheless, the structural stress technique has shown to be sufficiently accurate for engineering design estimations.

References

[1] J.R. Davis & Associates., ASM International. Handbook Committee. Aluminum and aluminum alloys. ASM International; 1993.

[2] Polmear IJ. Light alloys : from traditional alloys to nanocrystals. Elsevier/Butterworth-Heinemann; 2006.

[3] Standard Practice for Heat Treatment of Wrought Aluminum Alloys. Annu B ASTM Stand 2012:1–14. doi:10.1520/B0918.

[4] Hausöl T, Höppel HW, Göken M. Microstructure and mechanical properties of accumulative roll bonded aluminium alloy AA5754. J Phys Conf Ser 2010;240:12128. doi:10.1088/1742-6596/240/1/012128.

[5] Hatch J, Association A. Aluminum: properties and physical metallurgy. 1984.

[6] Zhang H, Senkara J, Wu X. Suppressing Cracking in Resistance Welding AA5754 by Mechanical Means. J Manuf Sci Eng 2002;124:79. doi:10.1115/1.1418693.

[7] Mishra RS, Partha SDNK. Friction stir welding and processing. Switzerland: Springer International Publishing; 2014.

[8] Brosi JK. Mechanical property evolution of Al-Mg alloys following immediate temperature thermal exposure. Case Western Reserve University, 2010.

[9] Kaufman JG (John G. Properties of aluminum alloys : tensile, creep, and fatigue data at high and low temperatures. ASM International; 1999.

[10] Burger GB, Gupta AK, Jeiirey W, Lloyd DJ. Microstructural Control of Aluminum Sheet Used in Automotive Applications. Mater Charact 1995;5803.

[11] Abbadi M, Hähner P, Zeghloul A. On the characteristics of Portevin - Le Chatelier bands in aluminum alloy 5182 under stress-controlled and strain-controlled tensile testing. Mater Sci Eng A 2002;337:194–201. doi:10.1016/S0921-5093(02)00036-9.

[12] A. van den Beukel. Theory of the effect of dynamic strain aging on mechanical properties. 1975. doi:10.1002/pssa.2210300120.

[13] Weisse M, Wamukwamba CK, Christ HJ, Mughrabi H. The cyclic deformation and fatigue behaviour of the low carbon steel SAE 1045 in the temperature regime of dynamic strain ageing. Acta Metall Mater 1993;41:2227–33. doi:10.1016/0956-7151(93)90392-6.

[14] Srinivasan VS, Sandhya R, Valsan M, Rao KBS, Mannan SL. Comparative evaluation of strain controlled low cycle fatigue behaviour of solution annealed and prior cold worked 316L(N) stainless steel. Int J Fatigue 2004;26:1295–302. doi:10.1016/j.ijfatigue.2004.05.003.

[15] Nani Babu M, Sasikala G, Shashank Dutt B, Venugopal S, Albert SK, Bhaduri AK, et al. Investigation on influence of dynamic strain ageing on fatigue crack growth behaviour of modified 9Cr-1Mo steel. Int J Fatigue 2012;43:242–5.

doi:10.1016/j.ijfatigue.2012.02.022.

[16] Fortin PE, Bull MJ, Moore DM. An Optimized Aluminum Alloy (X6111) for Auto Body Sheet Applications. SAE Int. Congr. Expo., 1983. doi:10.4271/830096.

[17] Esmaeili S, Wang X, Lloyd DJ, Poole WJ. On the Precipitation-Hardening Behavior of the Al-Mg-Si-Cu Alloy AA6111. Metall Mater Trans A 2003;34A:751–63.

[18] Bryant JD. The Effects of Preaging Treatments on Aging Kinetics and Mechanical Properties in AA6111 Aluminum Autobody Sheet. Metall Mater Trans A 1999;30A.

[19] Murayama M, Hono K, Miao WF, Laughlin DE. The effect of Cu additions on the precipitation kinetics in an Al-Mg-Si alloy with excess Si. Metall Mater Trans A 2001;32:239–46. doi:10.1007/s11661-001-0254-z.

[20] Chakrabarti DJ, Peng Y, Laughlin DE. Precipitation in Al-Mg-Si alloys with Cu additions and the role of the Q' and related phases. Mater Sci Forum 2002;396–402:857–62. doi:10.4028/www.scientific.net/MSF.396-402.857.

[21] Miao WF, Laughlin DE. Effects of Cu content and preaging on precipitation characteristics in aluminum alloy 6022. Metall Mater Trans A 2000;31:361–71. doi:10.1007/s11661-000-0272-2.

[22] Lloyd DJ, Evans DR, Gupta AK. Precipitation reactions and the Differential Scanning Calorimetry response of AA6111 alloy. Can Metall Q 2000;39:475–82. doi:10.1179/000844300794388732.

[23] Andersen SJ, Zandbergen HW, Jansen J, TrÆholt C, Tundal U, Reiso O. The crystal structure of the β″ phase in Al–Mg–Si alloys. Acta Mater 1998;46:3283–98. doi:10.1016/S1359-6454(97)00493-X.

[24] Ramesh R, Bhattacharya R, Williams G. Effect of ageing on the mechanical behaviour of a novel automotive grade Al–Mg–Si alloy. Mater Sci Eng A 2012;541:128–34. doi:10.1016/j.msea.2012.02.013.

[25] Esmaeili S, Lloyd D. Modeling of precipitation hardening in pre-aged AlMgSi(Cu) alloys. Acta Mater 2005;53:5257–71. doi:10.1016/j.actamat.2005.08.006.

[26] Poole WJ, Wang X, Lloyd DJ, Embury JD. The shearable–non-shearable transition in Al–Mg–Si–Cu precipitation hardening alloys: implications on the distribution of slip, work hardening and fracture. Philos Mag 2005;85:3113–35. doi:10.1080/14786430500154935.

[27] Zaiken E, Ritchie RO. Effects of microstructure on fatigue crack propagation and crack closure behavior in aluminum alloy 7150. Mater Sci Eng 1985;70:151–60. doi:10.1016/0025-5416(85)90276-9.

[28] Edwards L, Busby AK, Martin JW. Effect of aging and dispersoid content on fatigue crack growth of in Al-Mg-Si alloys. Mater Sci Technol 1986;2:823–8.

[29] Lee DH, Park JH, Nam SW. Enhancement of mechanical properties of Al-Mg-Si alloys by means of manganese dispersoids. Mater Sci Technol 1999;15:450–5.

[30] Nam S, Lee D. The effect of Mn on the mechanical behavior of Al alloys. Met Mater 2000;6:13–6. doi:10.1007/bf03026339.

[31] Pereira AM, Ferreira JM, Loureiro A, Costa JDM, Bártolo PJ. Effect of process parameters on the strength of resistance spot welds in 6082-T6 aluminium alloy. Mater Des 2010;31:2454–63. doi:10.1016/j.matdes.2009.11.052.

[32] Wu SN, Ghaffari B, Hetrick E, Li M, Jia ZH, Liu Q. Microstructure characterization and quasi-static failure behavior of resistance spot welds of AA6111-T4 aluminum alloy. Trans Nonferrous Met Soc China (English Ed 2014;24:3879–85. doi:10.1016/S1003-6326(14)63546-9.

[33] Weman K. Pressure welding methods. Weld. Process. Handb. 2nd ed., 2012, p. 119–32. doi:10.1533/9780857095183.119.

[34] Chang B, Du D, Sui B, Zhou Y. Effect of forging force on fatigue behavior of spot welded joints of aluminum alloy 5182. J 2007.

[35] Zhang H, Senkara J. Resistance Welding: Fundamentals and Applications. vol. 65. 2nd ed. Boca Raton: 2006. doi:10.1017/CBO9781107415324.004.

[36] American Welding Society. Welding Handbook - Welding Science and Technology. vol. 1. Ninth. Miami: 2001.

[37] Ammar HR, Samuel AM, Samuel FH. Effect of casting imperfections on the fatigue life of 319-F and A356-T6 Al-Si casting alloys. Mater Sci Eng A 2008;473:65–75. doi:10.1016/j.msea.2007.03.112.

[38] Campbell J. Porosity. Complet. Cast. Handb., 2015, p. 341–415. doi:10.1016/B978-0-444-63509-9.00007-8.

[39] Lee P., Chirazi A, See D. Modeling microporosity in aluminum–silicon alloys: a review. J Light Met 2001;1:15–30. doi:10.1016/S1471-5317(00)00003-1.

[40] Suresh S. Fatigue of Materials. Cambridge University Press; 1998. doi:10.1017/CBO9780511806575.

[41] Paris PC, Gomez MP, Anderson WE. A rational analytic theory of fatiuge. Trend Eng 1961;13:9–14. doi:10.11648/j.ijmea.s.2015030201.11.

[42] Paris P, Erdogan F. A Critical Analysis of Crack Propagation Laws. J Basic Eng 1963;85:528–33. doi:10.1115/1.3656900.

[43] Pearson S. Initiation of fatigue cracks in commercial aluminium alloys and the subsequent propagation of very short cracks. Eng Fract Mech 1975;7:235–47. doi:10.1016/0013-7944(75)90004-1.

[44] Suresh S, Ritchie RO. Propagation of short fatigue cracks. Int Met Rev 1984;29:445–76. doi:10.1179/imtr.1984.29.1.445.

[45] Davidson DL. Small and large fatigue cracks in aluminum alloys. Acta Metall 1988;36:2275–82. doi:10.1016/0001-6160(88)90327-6.

[46] Ritchie RO, Lankford J. Small Fatigue Cracks: A Statement of the Problem and Potential Solutions. Mater Sci Eng 1986;84:11–6.

[47] Lankford J. The Influence of Microstructure on the Growth of Small Fatigue Cracks. Fatigue Fract Eng Mater Struct 1985;8:161–75.

[48] Taylor D. Fatigue thresholds: their applicability to engineering situations. Int J Fatigue 1988;10:67–79. doi:10.1016/0142-1123(88)90034-5.

[49] Zhai T, Jiang XP, Li JX, Garratt MD, Bray GH. The grain boundary geometry for optimum resistance to growth of short fatigue cracks in high strength Al-alloys. Int J Fatigue 2005;27:1202–9. doi:10.1016/j.ijfatigue.2005.06.021.

[50] Schäf W, Marx M, Knorr AF. Influence of microstructural barriers on small fatigue crack growth in mild steel. Int J Fatigue 2013;57:86–92. doi:10.1016/j.ijfatigue.2012.11.006.

[51] Caton MJ, Jones JW, Boileau JM, Allison JE. The effect of solidification rate on the growth of small fatigue cracks in a cast 319-type aluminum alloy. Metall Mater Trans A 1999;30:3055–68. doi:10.1007/s11661-999-0216-4.

[52] Chowdhury P, Sehitoglu H. Mechanisms of fatigue crack growth - a critical digest of theoretical developments. Fatigue Fract Eng Mater Struct 2016:n/a-n/a. doi:10.1111/ffe.12392.

[53] Suresh S. Crack deflection: Implications for the growth of long and short fatigue cracks. Metall Trans A 1983;14:2375–85. doi:10.1007/BF02663313.

[54] Suresh S. Fatigue crack deflection and fracture surface contact: Micromechanical models. Metall Trans A 1985;16:249–60. doi:10.1007/BF02815306.

[55] Hornbogen E, Gahr Z. Microstructure and Fatigue Crack Growth in a y-Fe-Ni-Al Alloy. Acta Metall 1975;24:581–92.

[56] Lankford J, Davidson DL, Chan KS. The influence of crack tip plasticity in the growth of small fatigue cracks. Metall Trans A 1984;15:1579–88. doi:10.1007/BF02657797.

[57] Wilkinson AJ, Roberts SG, Hirsch PB. Modelling the threshold conditions for propagation of stage I fatigue cracks. Acta Mater 1998;46:379–90. doi:10.1016/S1359-6454(97)00290-5.

[58] Rice JR, Thomson R. Ductile versus brittle behaviour of crystals. Philos Mag 1974;29:73–97. doi:10.1080/14786437408213555.

[59] Bilby BA, Cottrell AH, Swinden KH. The Spread of Plastic Yield from a Notch. Proc R Soc London 1963;272:304–14.

[60] Weertman J. Dislocation based fracture mechanics. 1996.

[61] Shyam A, Allison JE, Jones JW. A small fatigue crack growth relationship and its application to cast aluminum. Acta Mater 2005;53:1499–509. doi:10.1016/j.actamat.2004.12.004.

[62] Rice JR. Mechanics of Crack Tip Deformation and Extension by Fatigue. Fatigue Crack Propag 1967;ASTM STP 4:247–309. doi:10.1520/STP47234S.

[63] Vasudeven AK, Sadananda K, Louat N. A review of crack closure, fatigue crack threshold and related phenomena. Mater Sci Eng A 1994;188:1–22. doi:10.1016/0921-5093(94)90351-4.

[64] Ritchie RO, Boyce BL, Campbell JP, Roder O, Thompson a. W, Milligan WW. Thresholds for high-cycle fatigue in a turbine engine Ti-6Al-4V alloy. Int J Fatigue 1999;21:653–62. doi:10.1016/S0142-1123(99)00024-9.

[65] Shyam A, Allison JE, Szczepanski CJ, Pollock TM, Jones JW. Small fatigue crack growth in metallic materials: A model and its application to engineering alloys. Acta Mater 2007;55:6606–16. doi:10.1016/j.actamat.2007.08.022.

[66] Edwards L, Zhang YH. Investigation of small fatigue cracks—II. A plasticity based model of small fatigue crack growth. Acta Metall Mater 1994;42:1423–31. doi:10.1016/0956-7151(94)90161-9.

[67] Navarro A, de los Rios ER. A Model for Short Fatigue Crack Propagation With an Interpretation of the Short-Long Crack Transition. Fatigue Fract Eng Mater Struct 1987;10:169–86. doi:10.1111/j.1460-2695.1987.tb01158.x.

[68] Taylor D. Modelling of fatigue crack growth at the microstructural level. Comput Mater Sci 2002;25:228–36. doi:10.1016/S0927-0256(02)00267-7.

[69] Wang QG, Davidson CJ, Griffiths JR, Crepeau PN. Oxide Films, Pores and the Fatigue Lives of Cast Aluminum Alloys 2006;37.

[70] Zhu X. Ultrasonic Fatigue of E319 Cast Aluminium Alloy in the Long Lifetime Regime. University of Michigan, 2007. doi:10.1017/CBO9781107415324.004.

[71] Wang QG, Apelian D, Lados DA. Fatigue behavior of A356-T6 aluminum cast alloys. Part I. Effect of casting defects. J Light Met 2001;1:73–84. doi:10.1016/S1471-5317(00)00008-0.

[72] Nayhumwa C, Green NR, Campbell J. Influence of casting technique and hot isostatic pressing on the fatigue of an Al-7Si-Mg alloy. Metall Mater Trans A 2001;32:349–58. doi:10.1007/s11661-001-0266-8.

[73] Boileau JM, Allison JE. The effect of solidification time and heat treatment on the fatigue properties of a cast 319 aluminum alloy. Metall Mater Trans A 2003;34:1807–20. doi:10.1007/s11661-003-0147-4.

[74] Gerard DA, Koss DA. The influence of porosity on short fatigue crack growth at large strain amplitudes. Int J Fatigue 1991;13:345–52. doi:10.1016/0142-1123(91)90364-5.

[75] Moffat AJ. Micromechanistic analysis of fatigue in aluminium silicon casting alloys, Phd Thesis 2007:p274.

[76] Gall K, Biallas G, Maier HJ, Horstemeyer MF, McDowell DL. Environmentally

influenced microstructurally small fatigue crack growth in cast magnesium. Mater Sci Eng A 2005;396:143–54. doi:10.1016/j.msea.2005.01.014.

[77] Chao YJ. Failure mode of spot welds: interfacial versus pullout. Sci Technol Weld Join 2003.

[78] Radakovic DJ, Tumuluru M. Predicting Resistance Spot Weld Failure Modes in Shear Tension Tests of Advanced High-Strength Automotive Steels. Weld J 2008;87:96S–105S.

[79] Tovo R, Livieri P. A numerical approach to fatigue assessment of spot weld joints. Fatigue Fract Eng Mater Struct 2011;34:32–45. doi:10.1111/j.1460-2695.2010.01488.x.

[80] Radaj D, Vormwald M. Advanced Methods of Fatigue Assessment. Berlin: Springer-Verlag; 2013. doi:10.1007/978-3-642-30740-9.

[81] Sheppard DS, Strange M. Fatigue Life Estimation in Resistance Spot Welds: Initiation and Early Growth Phase. Fatigue Fract Eng Mater Struct 1992;15:531–49.

[82] Rupp A, Storzel K, Grubisic V. Computer Aided Dimensioning of Spot-Welded Automotive Structures. SAE Tech Pap 1995;950711. doi:10.4271/950711.

[83] Kang H, Lee Y. Fatigue Life Prediction Methods of Resistance Spot-Welded Joints. Elsevier Inc.; 2012. doi:10.1016/B978-0-12-385204-5.00011-2.

[84] Dong P. A structural stress definition and numerical implementation for fatigue analysis of welded joints. Int J Fatigue 2001;23:865–76. doi:10.1016/S0142-1123(01)00055-X.

[85] Dong P, Prager M, Osage D. The Design Master S-N Curve In ASME Div 2 Rewrite And its Validations. Weld World 2007;51:53–63. doi:10.1007/BF03266573.

[86] Sheppard SD. Further Refinement of a Methodology for Fatigue Life Estimation in Resistance Spot Weld Connections "Further Refinement of a Methodology for Fatigue Life Estimation in Resistance Spot. Weld Connect Am Soc Test Mater 1996:265–82.

[87] Kang H, Dong P, Hong J. Fatigue analysis of spot welds using a mesh-insensitive structural stress approach. Int J Fatigue 2007;29:1546–53. doi:10.1016/j.ijfatigue.2006.10.025.

[88] Dong P, Huther M. Guide for Application of the Mesh Insensitive Methodology: Structural Stress. vol. 33. 2012.

[89] Newman JA, Dowling NE. Crack Growth Approach to Life Prediction of Spot-Welded Lap Joints. Fatigue Fract Eng Mater Struct 1998;21:1123–32.

[90] Okamoto H. Al-Mg (Aluminum-Magnesium). J Phase Equilibria 1998;19:598. doi:10.1361/105497198770341815.

[91] Sarkar J, Kutty TRG, Conlon KT, Wilkinson DS, Embury JD, Lloyd DJ. Tensile and bending properties of AA5754 aluminum alloys. Mater Sci Eng A 2001;316:52–9. doi:10.1016/S0921-5093(01)01226-6.

[92] Heinz B, Skrotzki B. Characterization of a friction-stir-welded aluminum alloy 6013. Metall Mater Trans B 2002;33:489–98. doi:10.1007/s11663-002-0059-5.

[93] Gavras AG, Chenelle BF, Lados D a. Effects of microstructure on the fatigue crack growth behavior of light metals and design considerations. Matéria (Rio Janeiro) 2010;15:319–29. doi:10.1590/S1517-70762010000200033.

[94] Spear A, Ingraffea A. Microstructurally small fatigue crack growth in thin, aluminum-alloy, pressure vessel liner. Procedia Eng 2011;10:686–91. doi:10.1016/j.proeng.2011.04.114.

[95] Bertin L. Tensile Strength of Automotive Aluminum Joints Using Resistance Spot Welding , Self-Piercing Riveting and Adhesive Hybrid Joining By. University of Windsor, 2014.

[96] Florea RS, Hubbard CR, Solanki KN, Bammann DJ, Whittington WR, Marin EB. Quantifying residual stresses in resistance spot welding of 6061-T6 aluminum alloy sheets via neutron diffraction measurements. J Mater Process Technol 2012;212:2358–70. doi:10.1016/j.jmatprotec.2012.06.024.

[97] Pugno N, Ciavarella M, Cornetti P, Carpinteri A. A generalized Paris' law for fatigue crack growth. J Mech Phys Solids 2006;54:1333–49. doi:10.1016/j.jmps.2006.01.007.

[98] Newman JCJ, Phillips EP, Swain MH. Fatigue-life prediction methodology using small-crack theory. Int J Fatigue 1999;21:109–19.

[99] Kim S-M, Kim M-H. Incorporating mesh-insensitive structural stress into the fatigue assessment procedure of common structural rules for bulk carriers. Int J Nav Archit Ocean Eng 2015;7:10–24. doi:10.1515/ijnaoe-2015-0002.

[100] Bonnen JJF, Agrawal H, Amaya MA, Iyengar RM, Kang H, Khosrovaneh AK, et al. Fatigue of Advanced High Strength Steel Spot-Welds 2006;2006.

Images

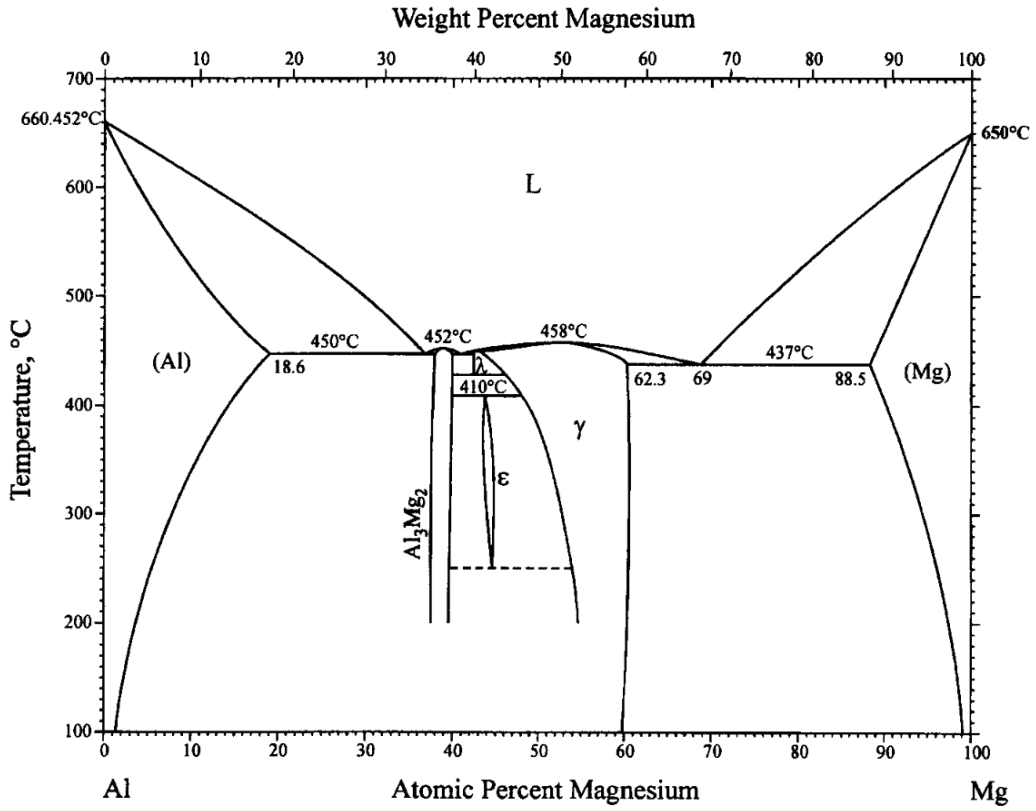

Figure 2.1 - Al-Mg phase diagram [90]

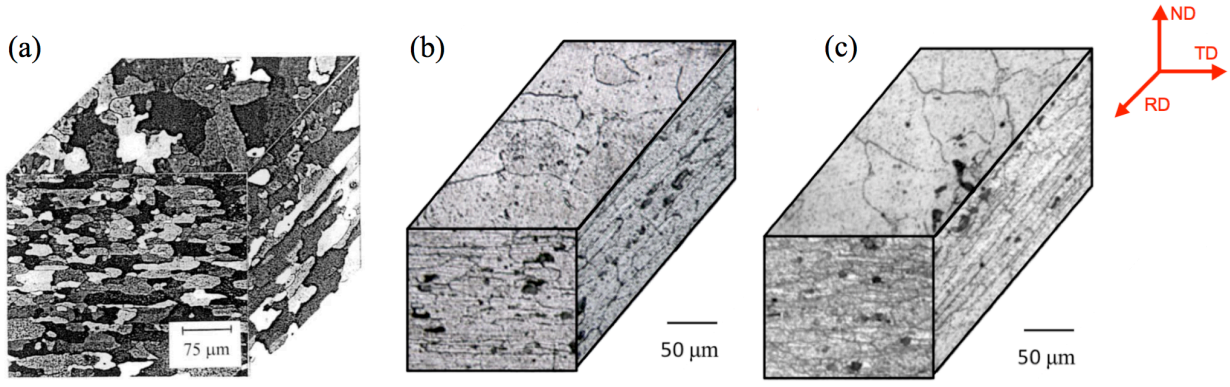

Figure 2.2 - Typical microstructure of rolled Al 5xxx alloy. (a) 5754 Al [91], (b) 5083-H116 (Al-4.5Mg) [8] and (c) 5456-H116 (Al-5Mg) [8].

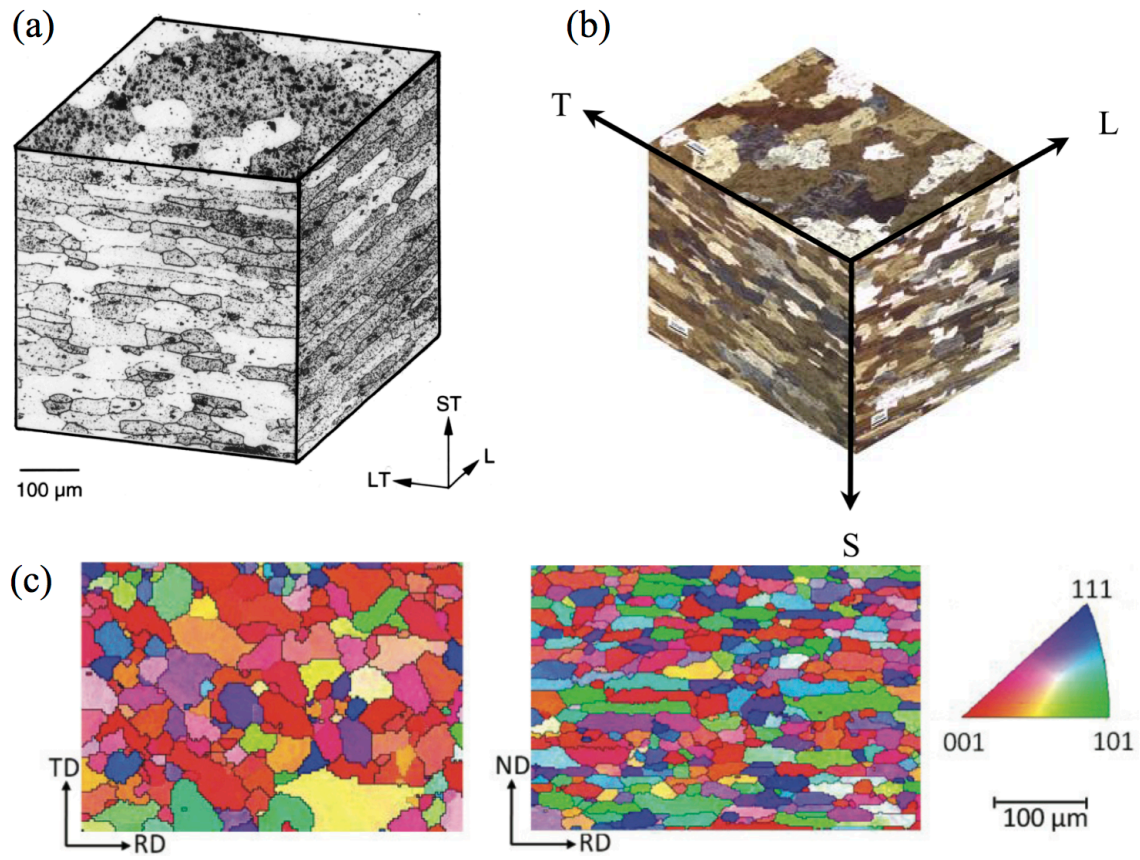

Figure 2.3 - Typical microstructure of rolled Al 6xxx alloy. (a) 6013 Al [92], (b) 6061-T651 [93] and (c) 6061-T6 [94].

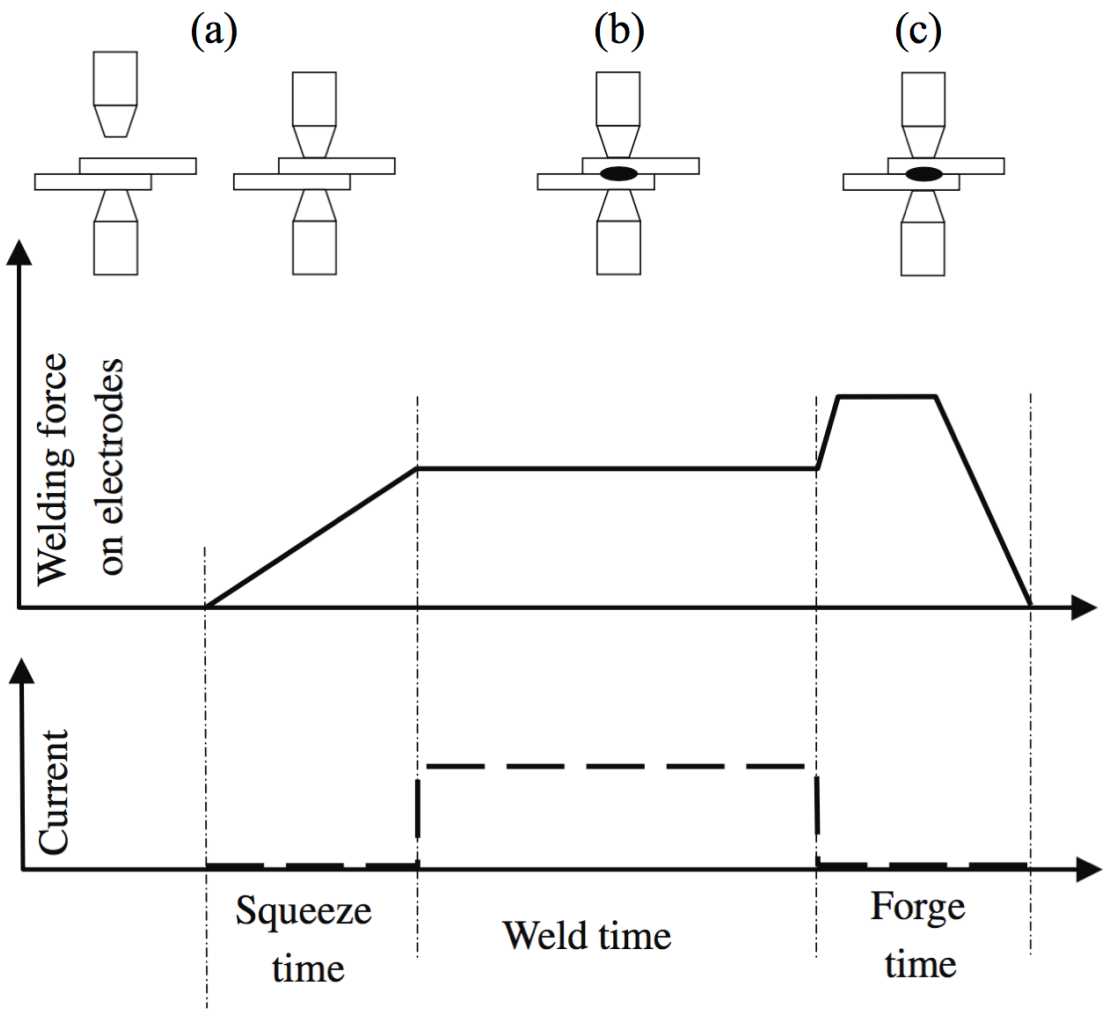

Figure 2.4 – Schematic of the resistance spot welding process; (a) clamping of the sheets between copper electrodes, (b) application of current, generating thermal energy and melting the material and (c) solidification of the melted material, forming a nugget which comprises the joint [31].

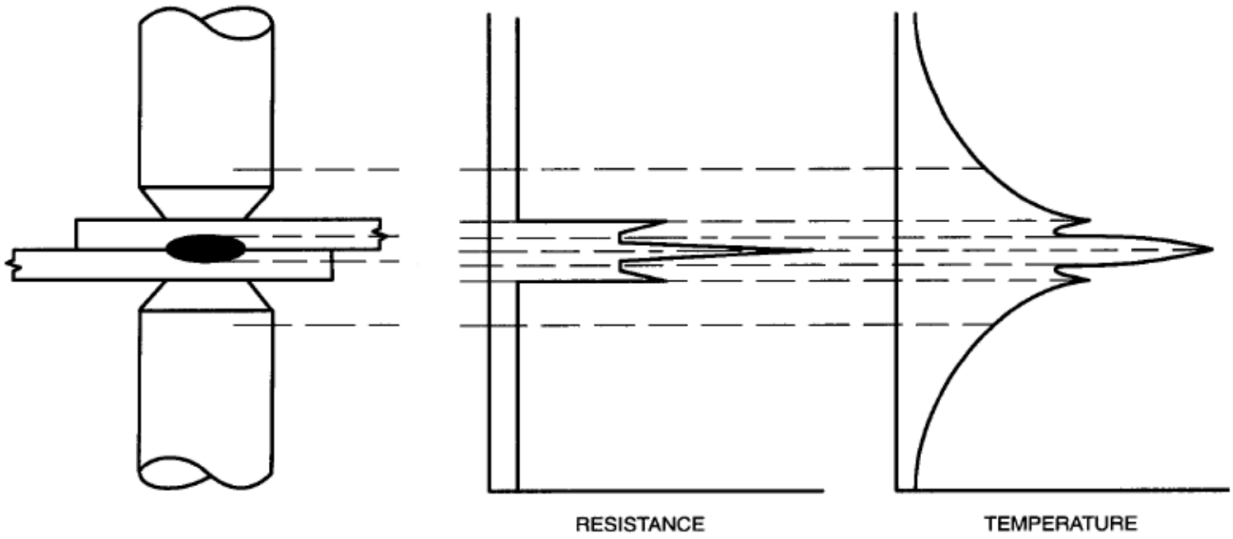

Figure 2.5 - Resistance and temperature distribution during the RSW process [95].

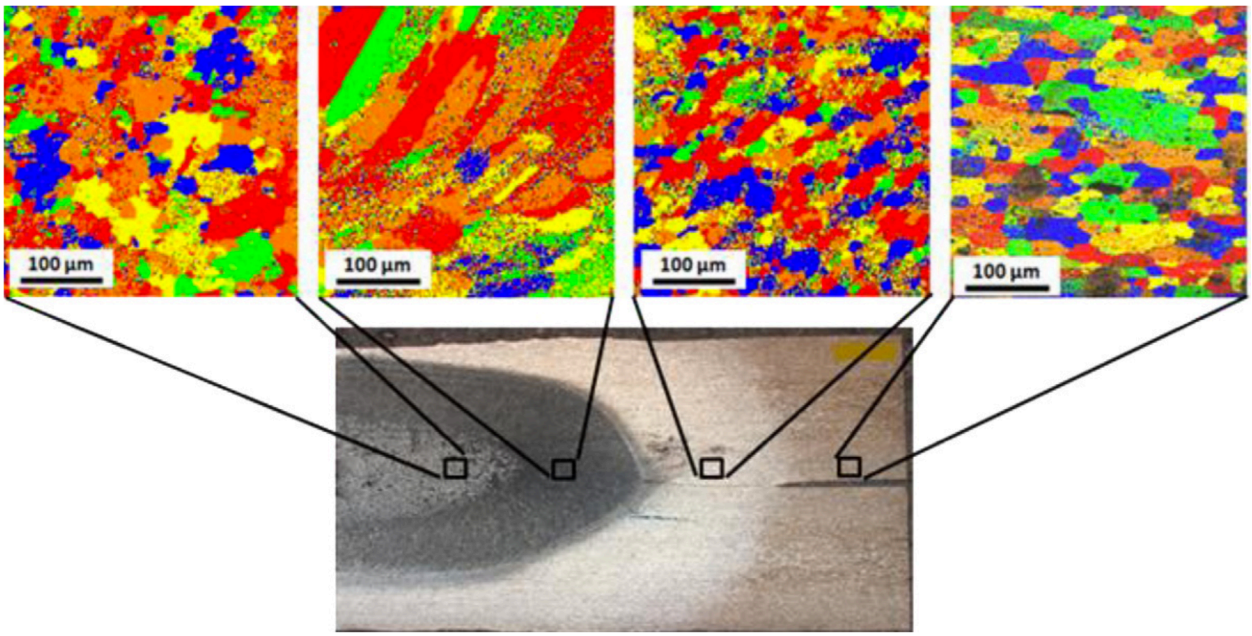

Figure 2.6 - EBSD maps of different regions in a resistance spot welded 6061-T6 joint [96]. The spot weld contains an equiaxed dendritic and columnar dendritic zone.

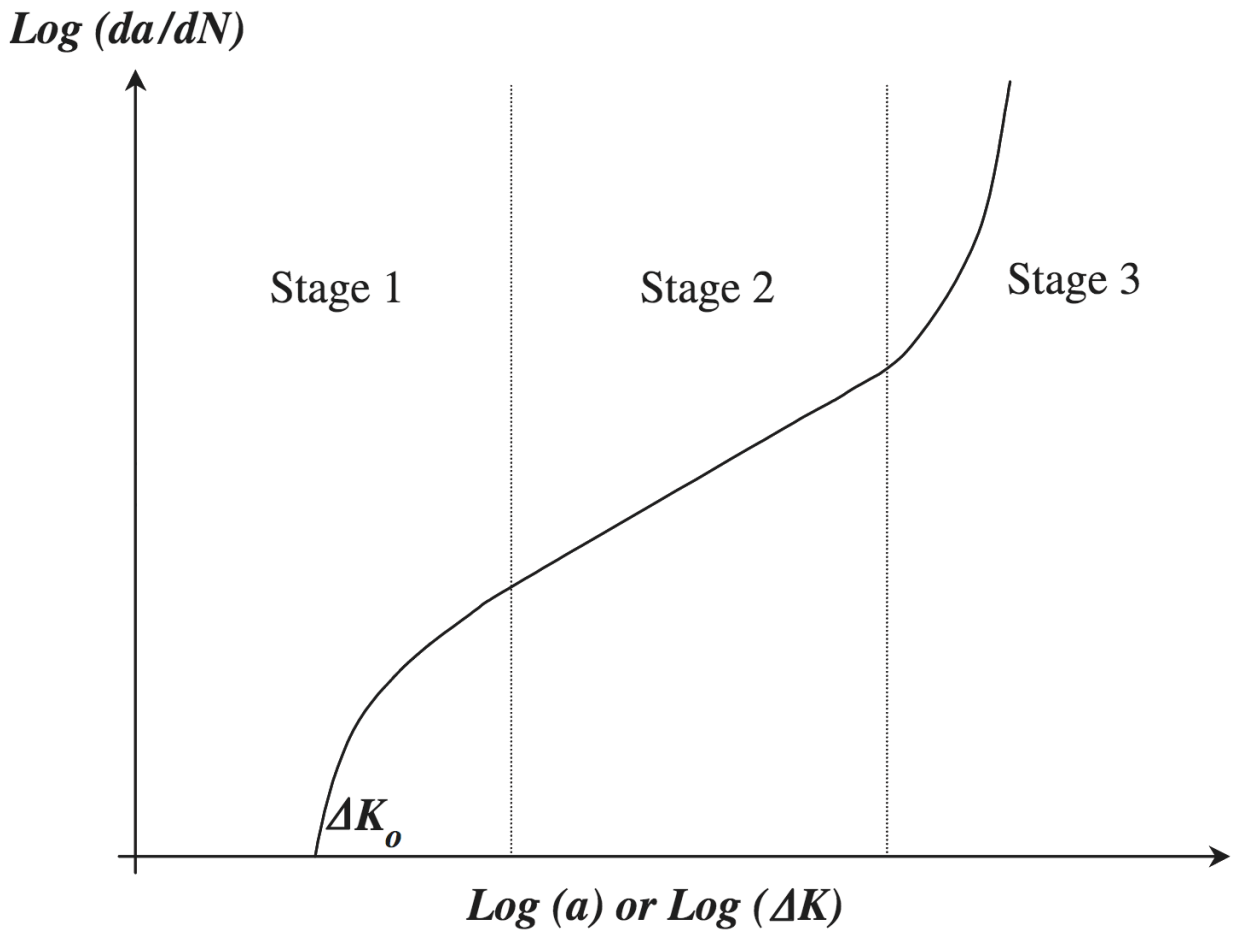

Figure 2.7 - Generic da/dN-ΔK curve [97].

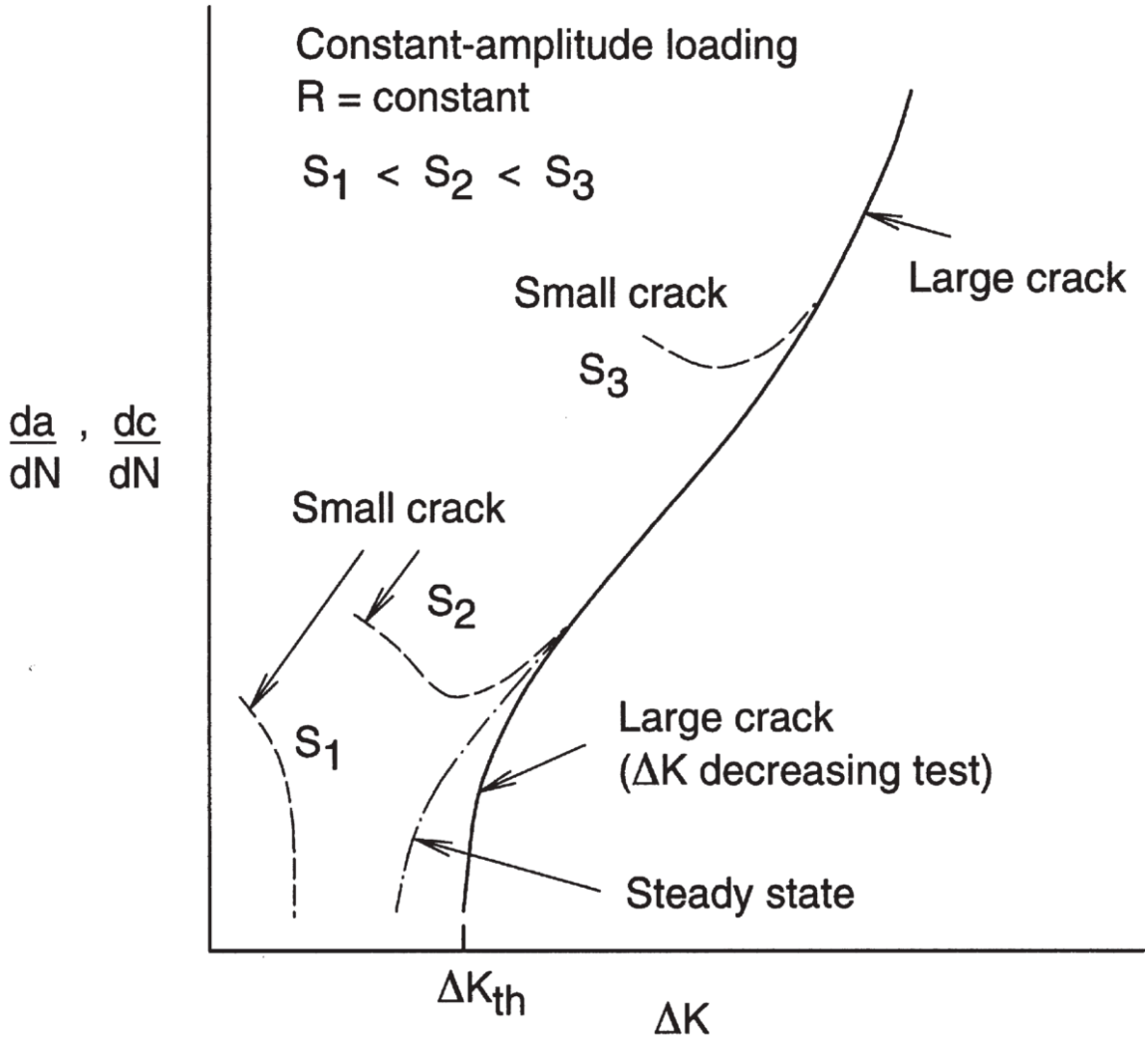

Figure 2.8 - Fatigue crack growth rate vs. stress intensity factor [98]. Short cracks exhibit anomalous behavior compared to traditional long crack growth behavior.

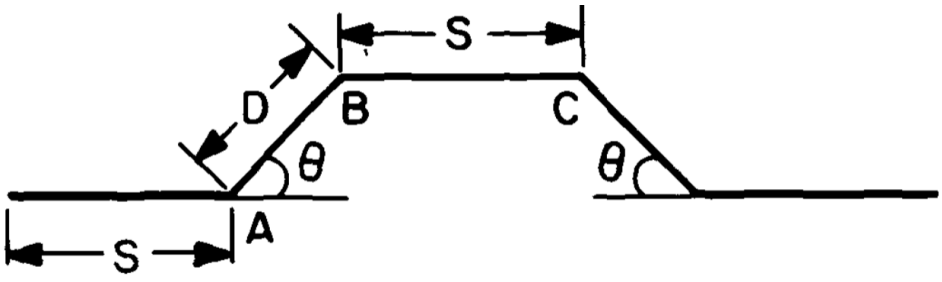

Figure 2.9 - Idealized crack with periodic deflections from Suresh [54].

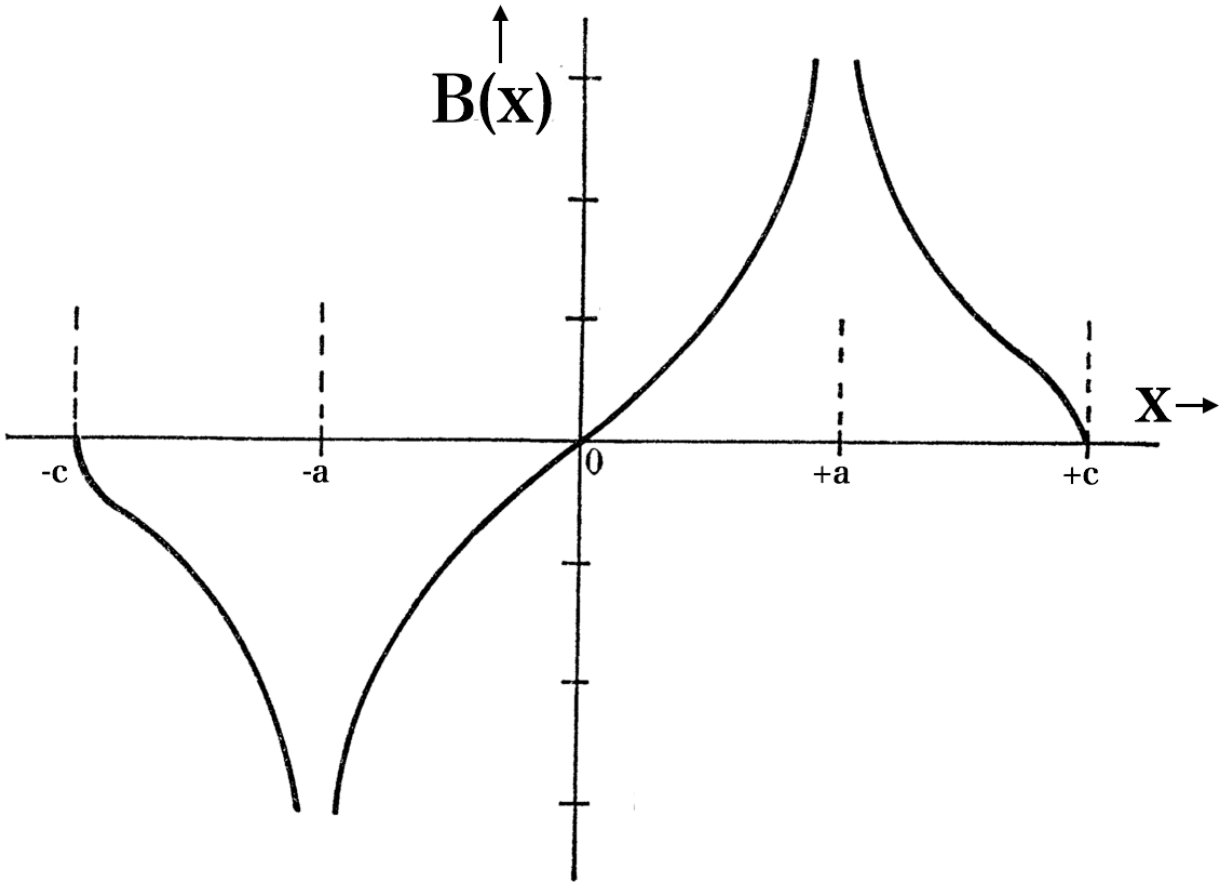

Figure 2.10 – Edge dislocation distribution along a crack subjected to uniaxial tension [59]. x = ± a corresponds to the edge of the crack tip and x = ± c corresponds to the edge of the monotonic plastic zone.

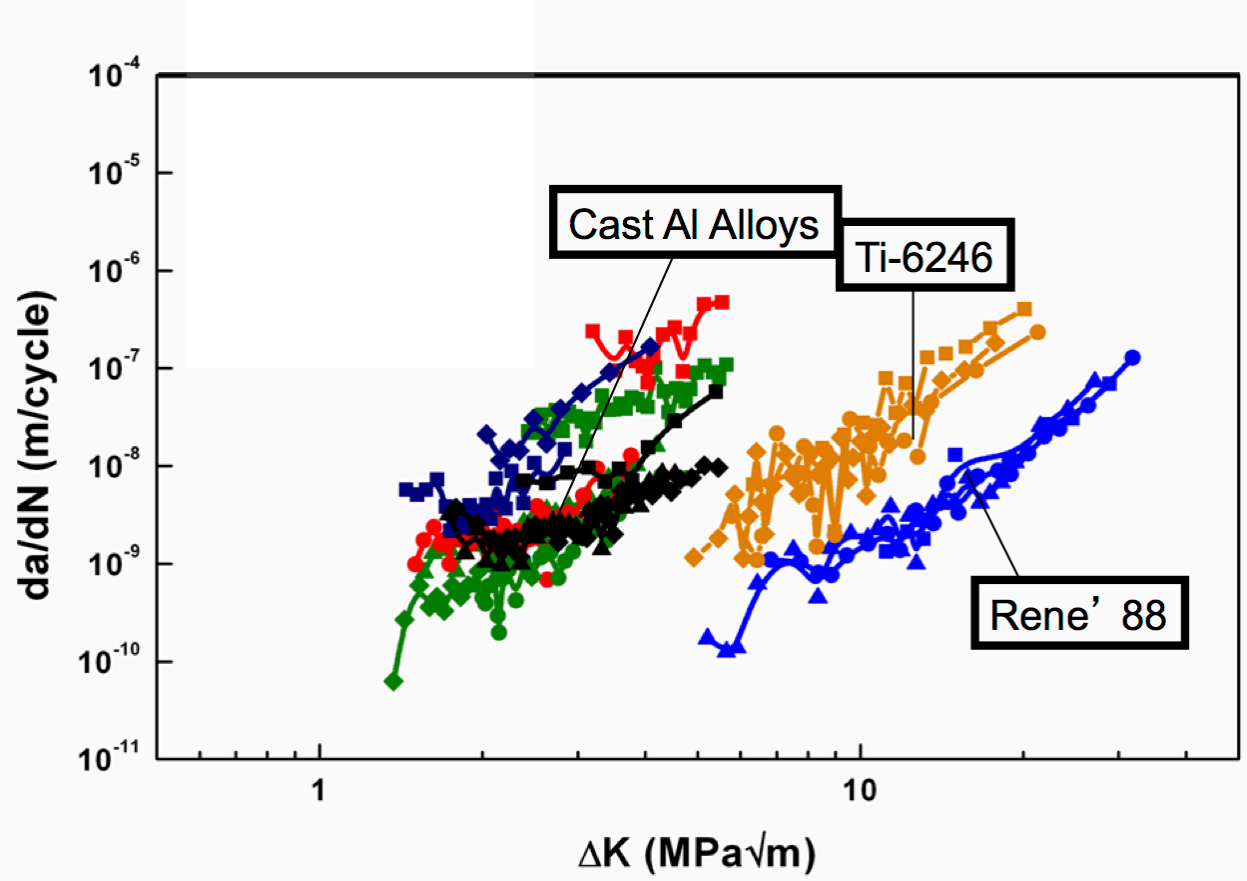

Figure 2.11 – Short fatigue crack growth rates vs. ΔK for a variety of systems [65].

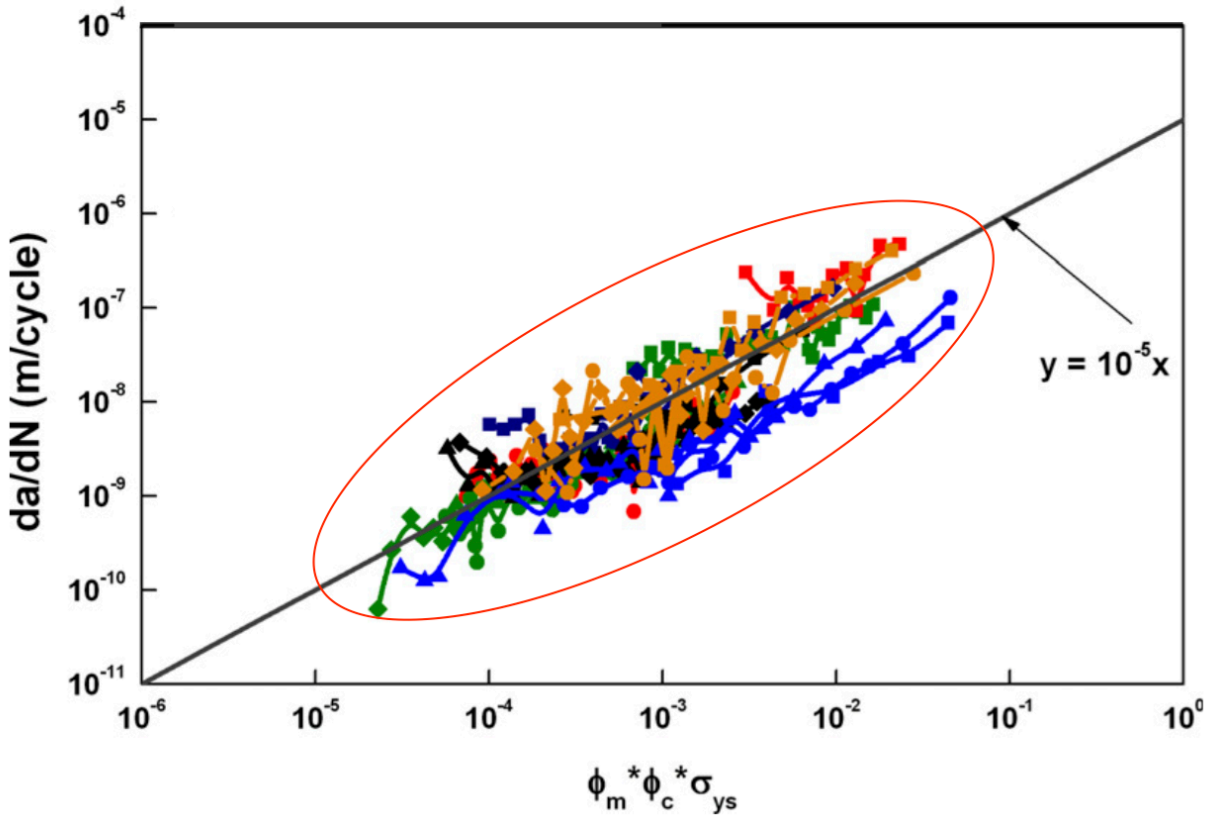

Figure 2.12 - Short crack growth rates vs. the unified parameter. The short crack growth rate for a given value of the unified parameter is similar across all alloy systems investigated.

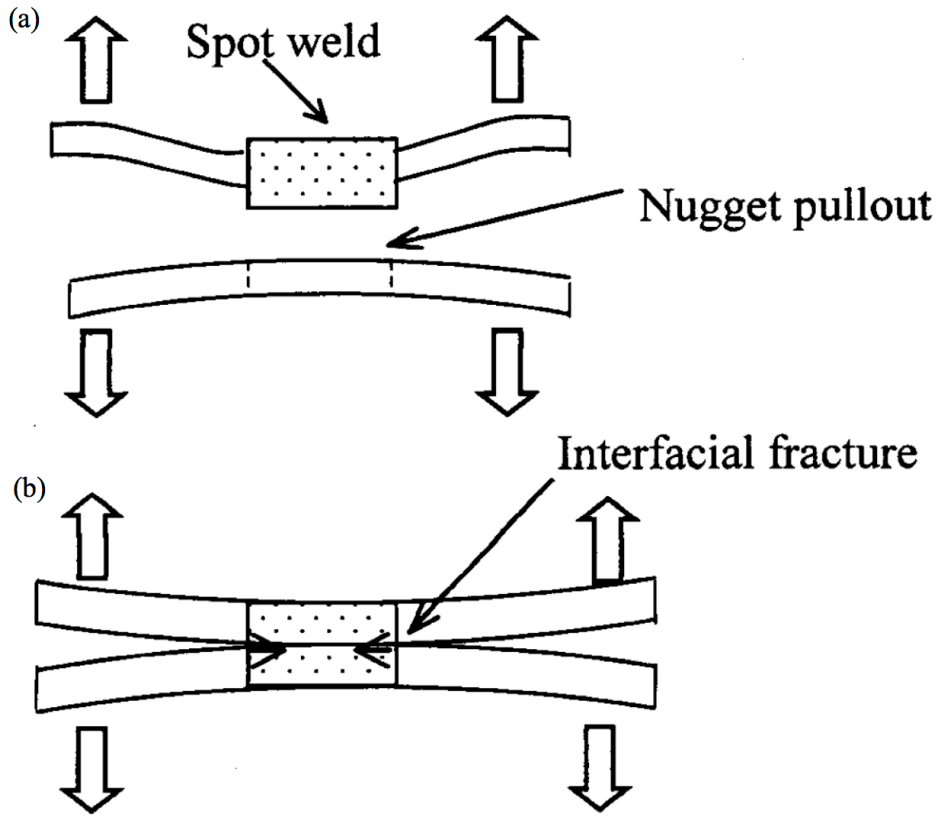

Figure 2.13 - Schematic of (a) nugget pullout and (b) interfacial failure in resistance spot welds [77].

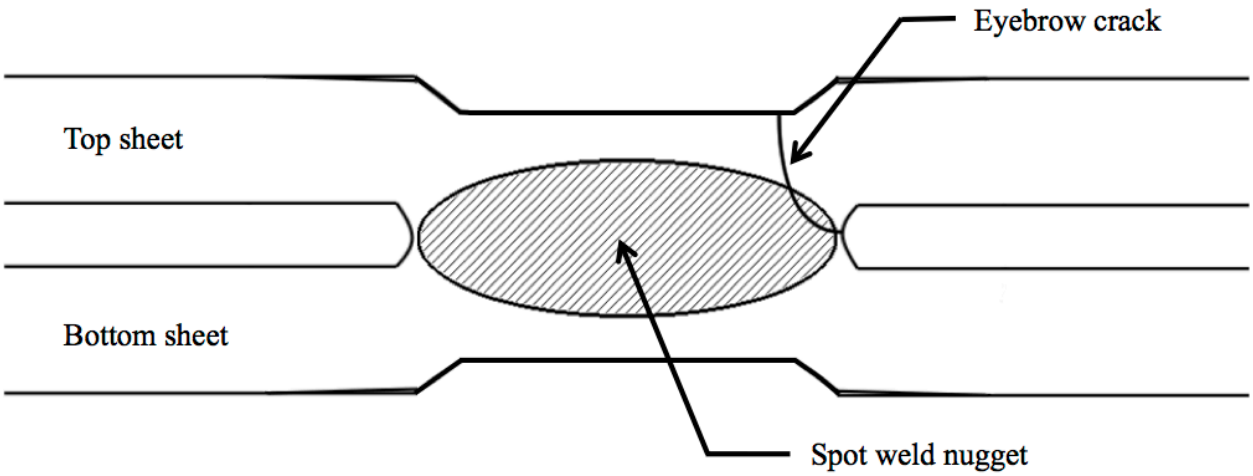

Figure 2.14 - Schematic of an "eyebrow" crack, defined as crack initiation at the edge of the spot weld and propagation through the sheet thickness.

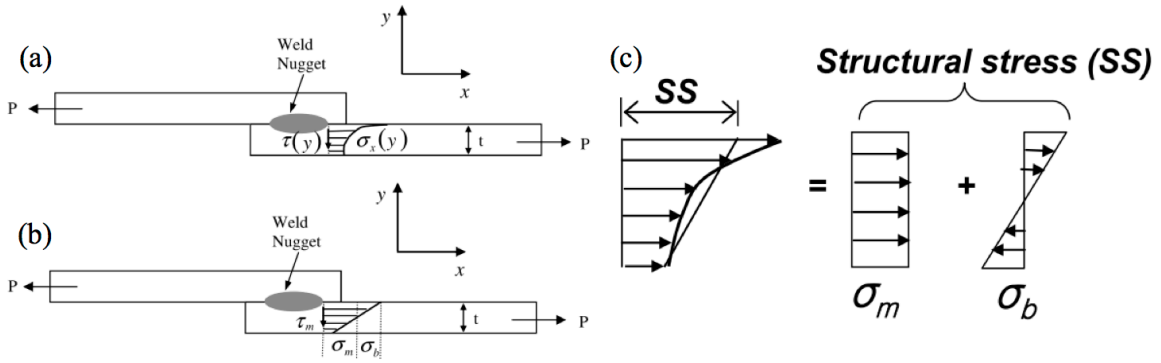

Figure 2.15 – Schematic of stress linearization. (a) Non-linear stress state at the spot weld edge, (b,c) linearized stress state [87].

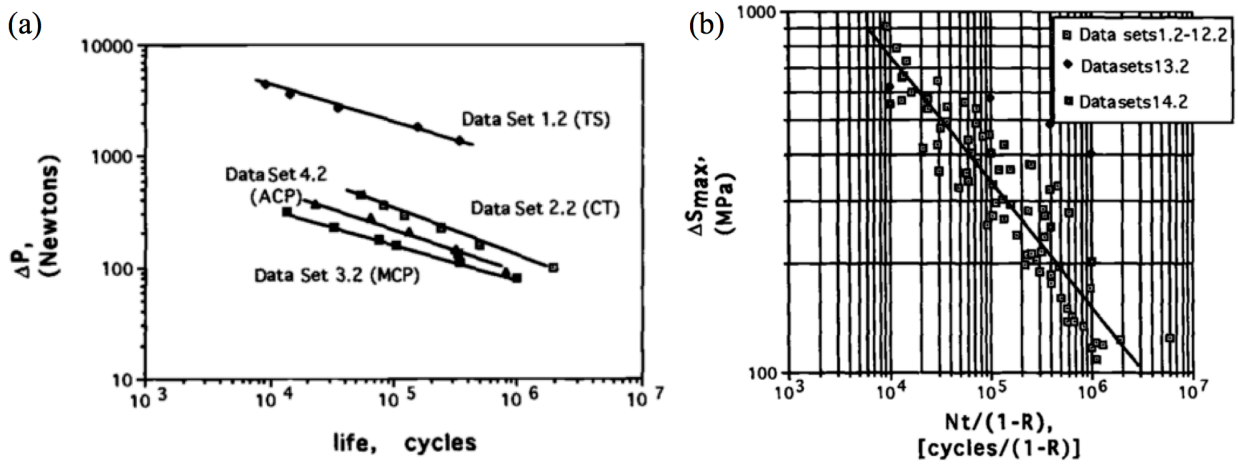

Figure 2.16 – Structural stress approach proposed by Sheppard [81,86]. (a) Nominal load vs. cycles to failure and (b) max structural stress vs. cycles to failure (normalized by the R ratio). The structural stress consolidates the data for different conditions.

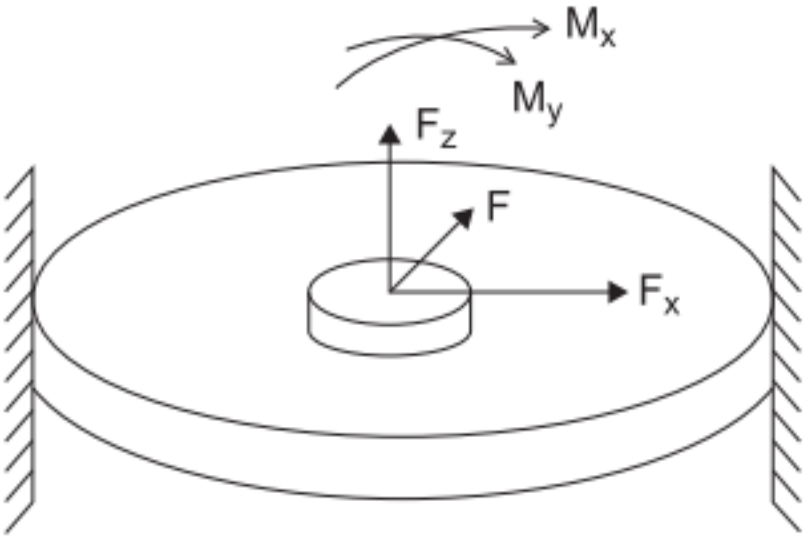

Figure 2.17 – Spot weld represented as a rigid inclusion as proposed by Rupp et al. [82].

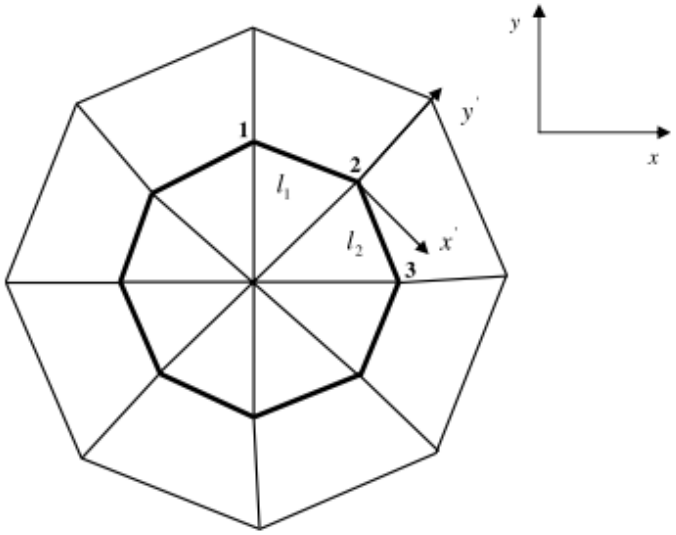

Figure 2.18 – FE mesh of the spot weld in the Battelle method [87]. Triangular shell elements and rigid beams form a spoke pattern.

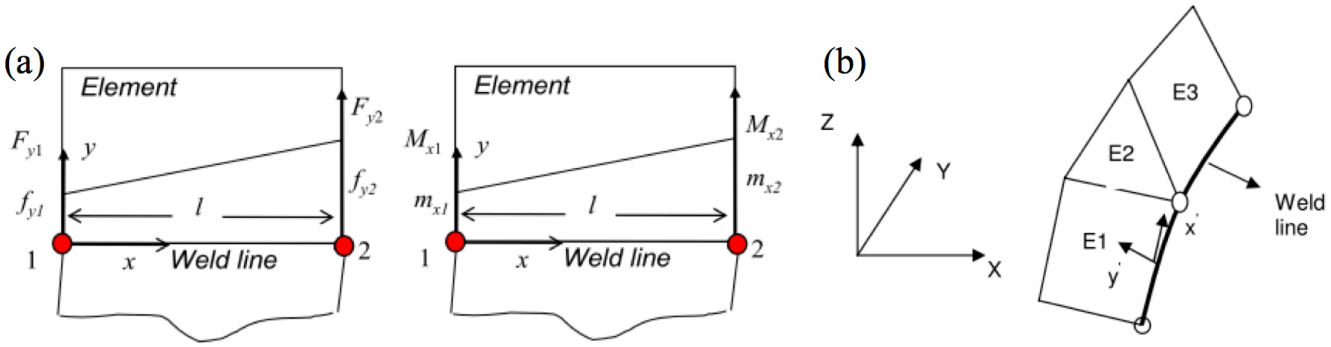

Figure 2.19 - Conversion from nodal forces and moments to line forces and moments (a) Definition of the line forces/moments at an FE element nodal point [99], (b) line forces distributed along the weld line between nodes in the local coordinate system [100].

Chapter 3

Experimental Approach

This chapter describes the materials investigated and the experimental technique employed in this research. Section 3.1 describes the two materials used for their research, as well as heat treatment and specimen fabrication. Section 3.2 describes the techniques used to determine the material microstructure, from optical and SEM/EBSD microscopy, to microhardness and radiographic testing. Finally, section 3.3 describes the short fatigue crack growth testing procedure, along with tensile and microtensile testing to determine the mechanical properties.

3.1 Material

3.1.1 Wrought Material

The materials tested in this investigation are the wrought aluminum 5754, an Al-3%Mg alloy, and aluminum 6111, an Al-1%Mg-1%Si-0.5%Cu alloy. The alloys were rolled to 3mm thickness and supplied by the Ford Motor Company's Research and Innovation center located in Dearborn, MI. The nominal compositions are presented in Table 3.1. The sheets were

approximately 300 mm by 100mm by 3mm. The as-received material was in the O-annealed (lowest strength, highest ductility) condition for alloy 5754 and the T4 temper (solution heat treated and naturally aged to a stable condition) for alloy 6111. As discussed in the literature review, alloy 5754 is non-heat treatable, and primarily hardened through solid solution, strain and grain size strengthening. Alloy 6111, on the other hand, is heat treatable and is primarily hardened through precipitation and dispersion strengthening.

3.1.2 Resistance Spot Welding

Resistance spot welding was performed by Dr. Elizabeth Hetrick at the Ford Motor Co. Research and Innovation Center. The process, as previously described in more detail, involves melting and solidifying sheet material that has been clamped together. The process is very quick and simulates the processes used in high volume production. Each individual spot weld takes less than 2s to complete. The welds display a cast microstructure as the wrought metal was melted and solidified to form the joint.

Traditional two sheet stackups of both alloys were spot welded together with thicknesses, t, of 1 and 3mm for fatigue life testing. The sheets stacked were 95mm by 25.4mm by the sheet thickness, while the overlap between sheets was 25.4mm, as shown in Figure 3.1. The parameters of the spot welding procedure (i.e. applied current, time) were optimized such that the nominal weld diameters were approximately 4 and 5 times the square root of the sheet thickness ($4t^{1/2}$ and $5t^{1/2}$).

In order to manufacture dogbone specimens for short fatigue crack growth testing, a 2-3-2mm sheet stackup was employed (that is, a 3mm sheet surrounded by two 2mm sheets). This is presented schematically in Figure 3.2. This process was used to ensure that the middle 3mm

sheet contained a RSW nugget throughout the entire thickness. The settings were optimized to produce a RSW nugget diameter of approximately 8mm. The dimensions of each of the plates used in the stackup were also 300x100mm. Each stackup contained two RSW nuggets to manufacture dogbone specimens. An image of the spot weld locations is provided in Figure 3.3.

3.1.3 Heat Treatment Procedure

Heat treatment was performed to determine the effects of aging on the mechanical and fatigue characteristics of both alloys. The primary heat treatment of interest is the paint-baked (PB) heat treatment, which is artificial aging of the alloys at 180°C for 30 minutes. The PB heat treatment is of interest in order to mimic the real world conditions of the alloys. During automotive production, after paint is applied, the vehicles are placed in an oven to expedite the dying and curing process of the paint [1]. The PB heat treatment essentially mimics this process. As alloy 5754 is a non-heat treatable alloy, any aging essentially acts as a low temperature anneal.

Heat treatment was performed a Thermo Scientific NESLAB EXACAL High Temperature bath with silicone oil. This ensured a rapid heat up and a stable and uniform aging temperature. In order to determine the effects of aging on the material hardness, sample blanks with dimensions 25.4 x 25.4 x 3 mm were placed in the oil bath for times ranging from 5 minutes to 50 hours at both 180°C and 210°C.

The heat treatment for aluminum 5754 consisted only of a PB heat treatment. For aluminum 6111, three heat treatments were investigated: T4 temper (solution heat-treated and naturally aged for at least 100 hours), a simulated PB heat treatment and an overaged condition (OA: artificially aged at 210°C for 12 hours).

The overaged condition was performed in order to understand the effects of overaging on the short fatigue crack growth characteristics. Overaging was conducted at 210°C, which was found to achieve similar hardness and yield strength to the PB condition. It was not possible to achieve the PB strength by aging at 180°C unless times greater than 100 hours were used.

3.1.4 Dogbone Specimen Design

Dogbone specimens were manufactured from the wrought and RSW samples such that the rolling direction was parallel to the gage length. Sample fabrication was performed by M. Cressey or K. Pruss at the University of Michigan Lay Mechanical Engineering machine shop. These specimen dimensions were consistent with ASTM E466 [2] and had a gage length of 36mm and a gage width of 18mm, as shown in Figure 3.4.

In order to manufacture the dogbone specimens on the RSW nuggets from the 2-3-2 stackup, the spot welds on the top and bottom 2mm sheets were mechanically milled off, leaving approximately $1/1000^{th}$ of an inch in order to ensure that the middle sheet material was not being removed. The middle sheet was then submitted for dogbone sample fabrication. An example of the cross-section of a 2-3-2 stackup and the RSW nugget location on the dogbone specimen are presented in Figure 3.5.

3.2 Microstructural Characterization

3.2.1 Sample Preparation

Metallographic specimens were mounted using Lapmaster fast cure epoxy resin in 1.25” diameter mounts. Dogbone specimens used for short fatigue crack growth tests were also prepared for EBSD patterning and optimal viewing for camera measurement of surface crack

growth. Specimens were prepared using a Buehler EcoMet 250 autopolisher and final polished with the Pace Technologies GIGA-1200 vibratory polisher. For the autopolishing, the following procedure was used: 150 RPM for the base, 60 RPM for the head with 20 N of force for dogbone specimens and 25 N of force for mounted metallographic specimens. Samples were ground from 320, 400, 600 and 800 grit SiC paper for 2-3 minutes with complementary rotation between the base and the head. The samples were then set to counter rotation and ground/polished for 5 minutes at 1200 grit, 9 μm, 6μm and 1μm polish. Samples were then placed in the vibratory polisher with MasterMet 2 colloidal silica (0.02 μm) for anytime between 4 and 12 hours (manual inspection for optimal polish was required). Etching of metallographic specimens to reveal grain structure was performed using Keller's reagent: 95% water, 2.5% nitric acid, 1.5% hydrochloric acid and 1% hydrofluoric acid. Etching was performed at room temperature for 30-60s.

3.2.2 Optical Microscopy

Optical microscopy was performed using a Nikon Epiphot 200 inverted microscope or a Zeiss Axio Vert.A1 inverted microscope equipped with a digital camera.

3.2.3 SEM and EBSD Analysis

Scanning electron microscopy (SEM) examination was completed with a TESCAN MIRA3 field emission gun (FEG) microscope, equipped with a backscatter electron (BSE) detector, an EDAX energy dispersive spectroscopy (EDS) detector, and an EDAX electron backscatter diffraction (EBSD) camera. SEM images were captured using an accelerating voltage between 15 and 30 kV to optimize image quality.

EBSD characterization was also performed in the SEM to determine the grain structure of the alloys. Operating conditions for EBSD were an accelerating voltage of 30 kV and a working distance of 20 mm. The beam intensity was set at 20.01 to give a spot size of approximately 18 nm. These conditions yielded reproducible high quality patterns at a rate of approximately 40 patterns per second with a step size of 0.75 μm. Image cleaning was performed in the EDAX TSL OIM data analysis software to smooth regions with a confidence index (CI) < 0.1 (areas of poor surface quality were typically indicative of grain boundaries).

3.2.4 Hardness and Microhardness Procedure

Rockwell hardness testing was performed on the 1" x 1" x 3mm blocks used to construct an artificial aging curve for aluminum alloy 6111. A Rockwell hardness tester was used to perform the hardness testing, and each block tested had 16 indents in a 4x4 pattern to optimize the number of measurements per sample while maintaining the minimum distance between points as prescribed by ASTM E8-11 [3]. For the wrought parent material, a Rockwell B (1/16" ball) indenter was used. For the RSW, the material was too soft for Rockwell B so a Rockwell E (1/8") was used instead.

Vickers microhardness mapping was completed at Ford Research and Innovation Center on a LECO AMH 43 automated microhardness system. Testing was performed on the wrought and RSW 5754 and 6111 aluminum alloys. A force of 200 gf for a dwell time of 13 s was applied for each microindentation, with spacing between points of approximately 200 μm. For the wrought alloys, an area of 3mm x 5mm was chosen, yielding approximately 400 indents. For the RSW alloys, an 8mm x 5mm region was chosen, yielding between 1200-1300 indents. The

microhardness data was then processed using a MATLAB script to interpolate the values between points.

3.2.5 Radiographic Testing

In order to quantify the porosity of the RSW specimens, radiographic testing was performed by the G. Campbell at the Ford Motor Co. Non-Destructive Evaluation Laboratory in Livonia, MI. 40 RSW Al 5754 samples and 25 RSW Al 6111 samples were submitted for assessment. The result was a two-dimensional image that was then processed in MATLAB to qualitatively identify the specimens with the lowest porosity on which short fatigue crack growth testing was performed.

3.3 Mechanical Testing

3.3.1 Short Fatigue Crack Growth (SFCG) Testing

SFCG samples were micronotched to provide a preferential small crack initiation site. A femtosecond laser was used to machine micronotches in the center of the dogbone specimen, irrespective of the local microstructure. Femtosecond laser machining produced small, reproducible notches with no-heat affected zone or microcracks, and minimal residual effects [4]. Notch fabrication was performed at the Center for Ultrafast Optical Science (CUOS) by M. Abere and R. Cahyadi. These notches were approximately 200 μm long, 50 μm wide and 100 μm deep. An SEM image of a typical femtosecond notch is provided in Figure 3.6.

Fatigue crack growth testing was conducted using an MTS servohydraulic test system, at a load ratio (R) of 0.1 and a cycling frequency of 30 Hz in lab air at 20°C. Samples were cycled with a constant maximum stress at stresses that were set fractions of the macroscopic yield

strength (approximately 60%, 70% and 80%). The crack length was measured optically using a QUESTAR QICAM digital camera with a 5μm resolution. The setup is displayed in Figure 3.7.

The half-crack length (a) versus the number of load cycles (N) was collected and converted into crack growth rate (da/dN) following ASTM E647 [5] using a seven-point sliding polynomial method to calculate da/dN. The stress intensity factor (ΔK) was determined using the Newman-Raju solution [6] for a semi-circular surface crack in a finite elastic plate, where the crack length to depth ratio was assumed to be one.

3.3.2 Tensile Testing

To determine the mechanical properties of interest (elastic modulus and yield strength) of the samples tested, tensile testing was performed on the dogbone specimens as prescribed in Section 3.1.4. Tensile testing was performed on 5 specimens for the alloys and heat treatments being tested, yielding 20 total tensile curves. Tensile testing was performed on an MTS servohydraulic test system, using an MTS 632.11B-20 extensometer with a 1" gage length. Samples were tested in displacement control with a strain rate of 0.015 mm/mm/min until specimen failure as prescribed by ASTM E8/E8M [7]. The data was analyzed using Microsoft Excel and the yield strength was calculated using the 0.2% offset method.

3.3.3 Microtensile Testing

The RSW nugget is contained within the overall gage section of the dogbone specimen and it was desired to determine the mechanical properties of just the weld nuggets in themselves. In order to do this, microtensile specimens of wrought and RSW 6111 were manufactured through electrical discharge machining (EDM) by Cut-Rite EDM Inc. such that the RSW nugget

was isolated in the gage section. The specimen geometry is shown in Figure 3.8. RSW 5754 samples were unable to be manufactured due to having too much porosity to EDM properly.

Microtensile testing was conducted in a Kammrath and Weiss tensile/compression module with a 5kN load cell as shown in Figure 3.9. An extensometer was not used and therefore the 0.015 mm/mm/min strain rate was approximated based on the specimen geometry. Wrought 6111 samples were fabricated to ensure that the mechanical properties achieved from the microtensile stage matched the larger dogbone specimens.

References

[1] Esmaeili S, Wang X, Lloyd DJ, Poole WJ. On the Precipitation-Hardening Behavior of the Al-Mg-Si-Cu Alloy AA6111. Metall Mater Trans A 2003;34A:751–63.

[2] Standard Practice for Conducting Force Controlled Constant Amplitude Axial Fatigue Tests of Metallic Materials. Annu B ASTM Stand 2012;i:1–5. doi:10.1520/E0466-07.2.

[3] Standard Test Methods for Rockwell Hardness of Metallic Materials. Annu B ASTM Stand 2012:1–37. doi:10.1520/E0018-11.2.

[4] Shyam A, Picard YN, Jones JW, Allison JE, Yalisove SM. Small fatigue crack propagation from micronotches in the cast aluminum alloy W319. Scr Mater 2004;50:1109–14. doi:10.1016/j.scriptamat.2004.01.031.

[5] Standard Test Method for Measurement of Fatigue Crack Growth Rates. Annu B ASTM Stand 2012;i. doi:10.1520/E0647-08E01.2.

[6] Newman JC, Raju IS. An empirical stress-intensity factor equation for the surface crack. Eng Fract Mech 1981;15:185–92. doi:10.1016/0013-7944(81)90116-8.

[7] Standard Test Methods for Tension Testing of Metallic Materials. Annu B ASTM Stand 2012:1–27. doi:10.1520/E0008.

[8] Series 647 Hydraulic Wedge Grips Reference Manual 2003:100–27.

[9] Kammarath and Weiss User Manual 2006;49:19.

[10] Deda EM. The effect of aluminum content and processing on the tensile behavior of high pressure die cast Mg alloys (Doctoral dissertation). 2016.

Tables

Table 3.1 - Compositions of the aluminum alloys investigated.

Alloy	Al (%)	Mg (%)	Si (%)	Cu (%)	Mn (%)	Fe (%)	Ti (%)
5754	Bal.	3	0.4	-	0.5	0.4	0.1
6111	Bal.	1	1	0.5	0.4	0.4	0.1

Figures

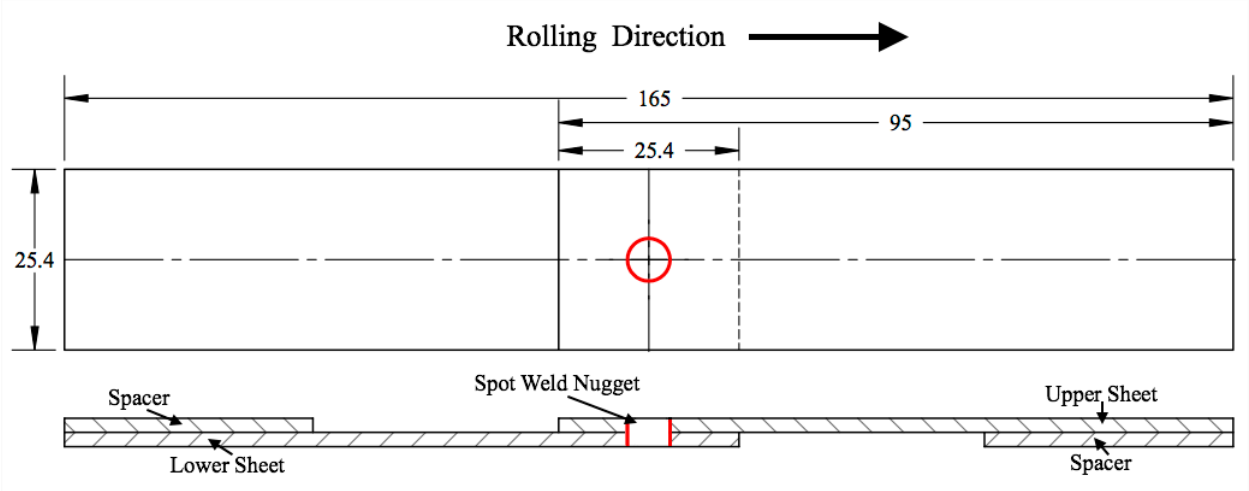

Figure 3.1 - Lap-shear spot welded specimen design.

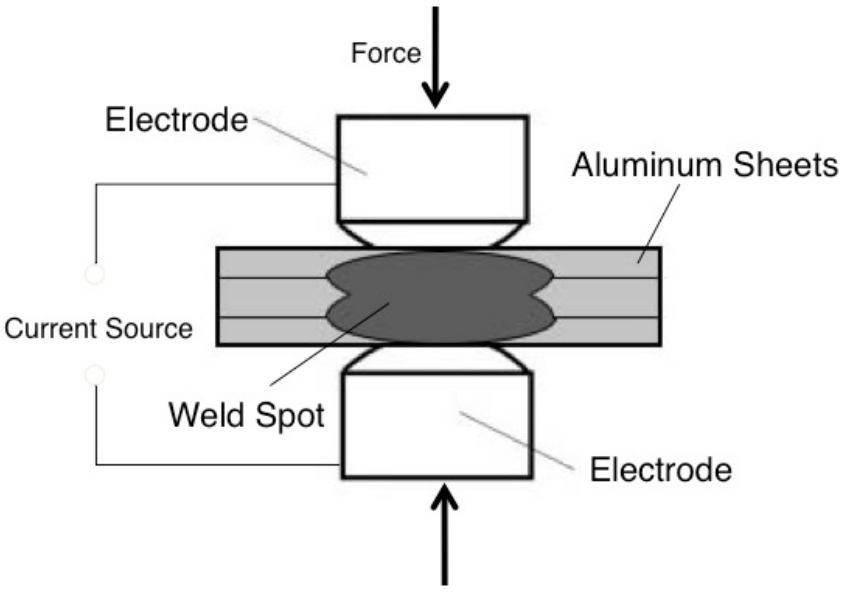

Figure 3.2 - RSW 2-3-2 stackup for manufacturing of short fatigue crack growth specimens.

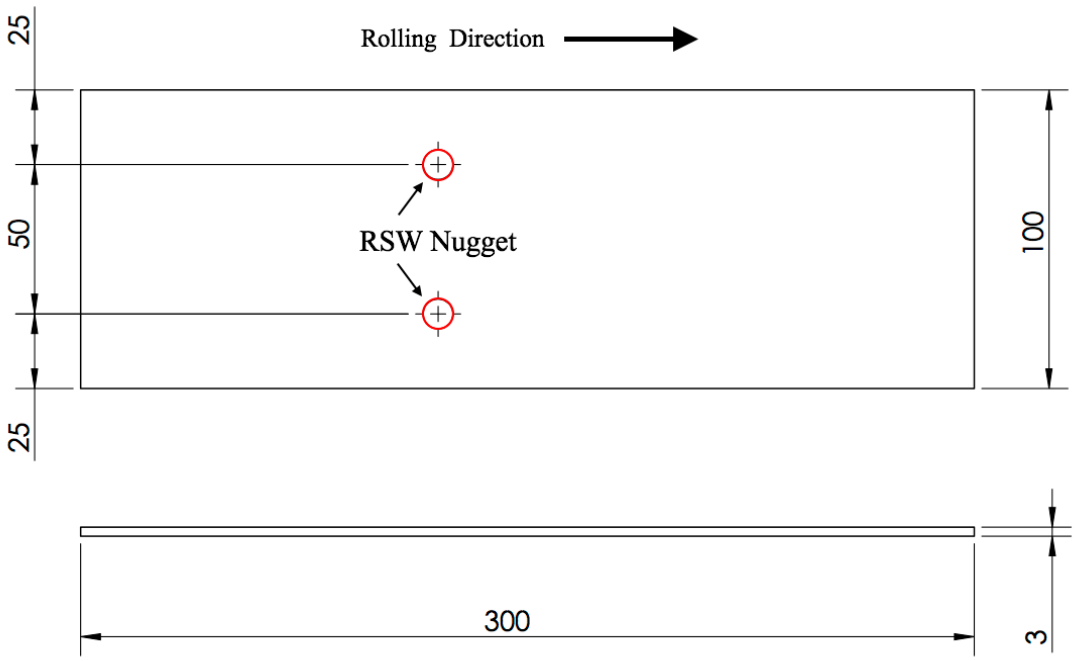

Figure 3.3 - RSW nugget locations in the middle sheet of the 2-3-2 sheet stackup. All units in mm.

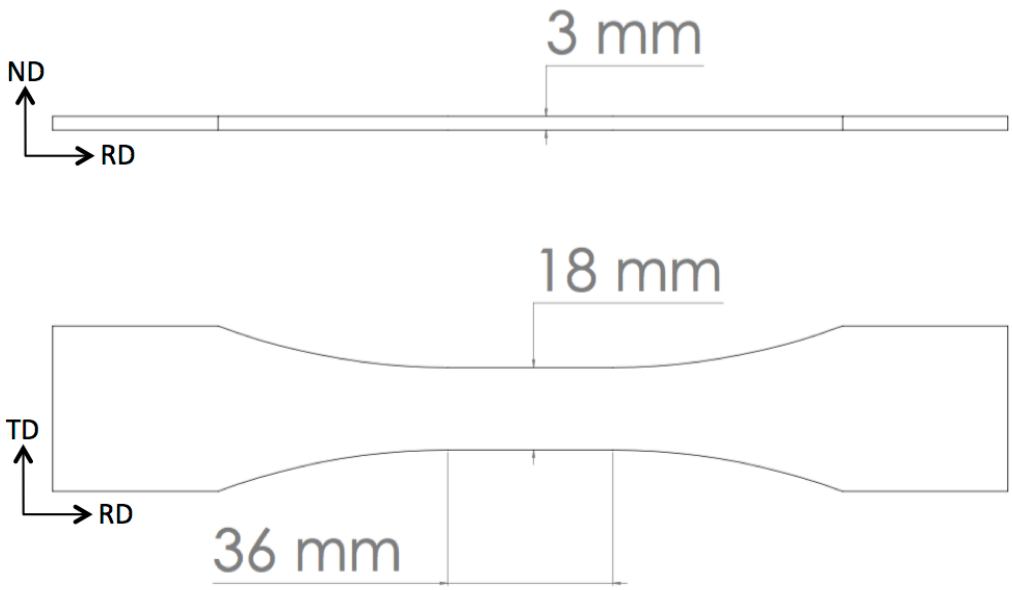

Figure 3.4 - Dogbone specimen sample design.

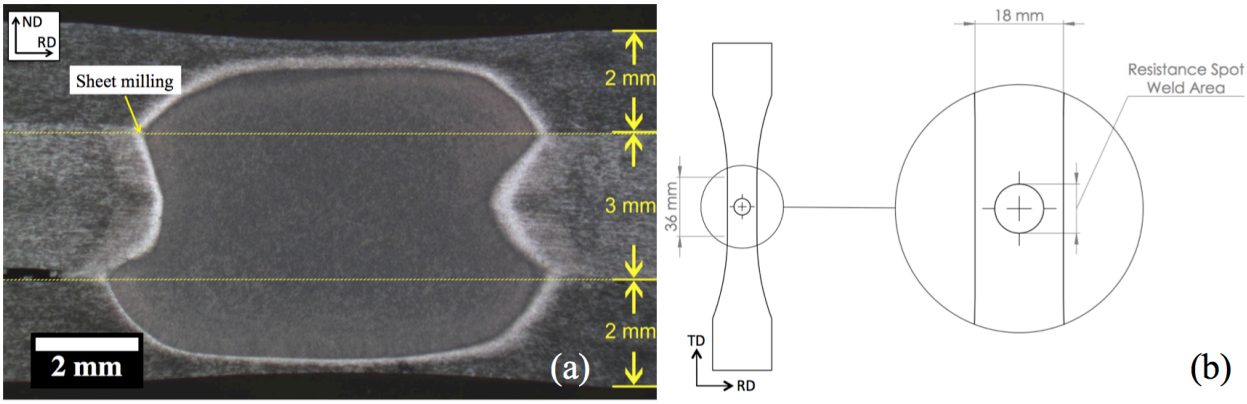

Figure 3.5 - RSW design for fatigue tests. (a) Removal of top and bottom sheets from 2-3-2 stackup. (b) RSW nugget location on the dogbone specimen. Note that the nugget size is exaggerated here.

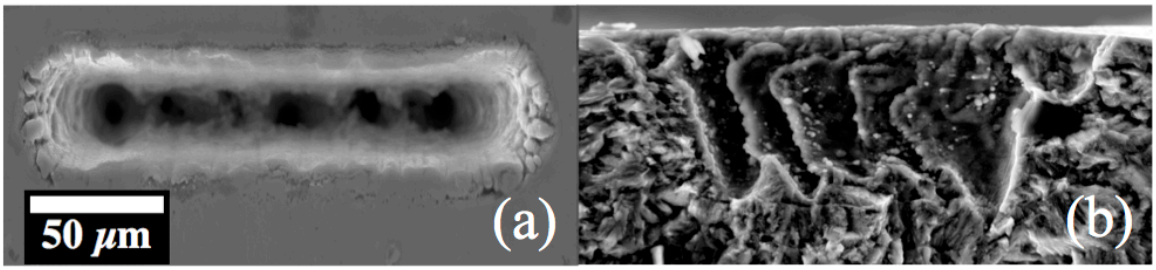

Figure 3.6 - SEM image of a femtosecond notch (a) Notch shape on the surface (TD-RD plane) (b) Notch shape from the fracture surface (ND-RD plane) with an irregular shape.

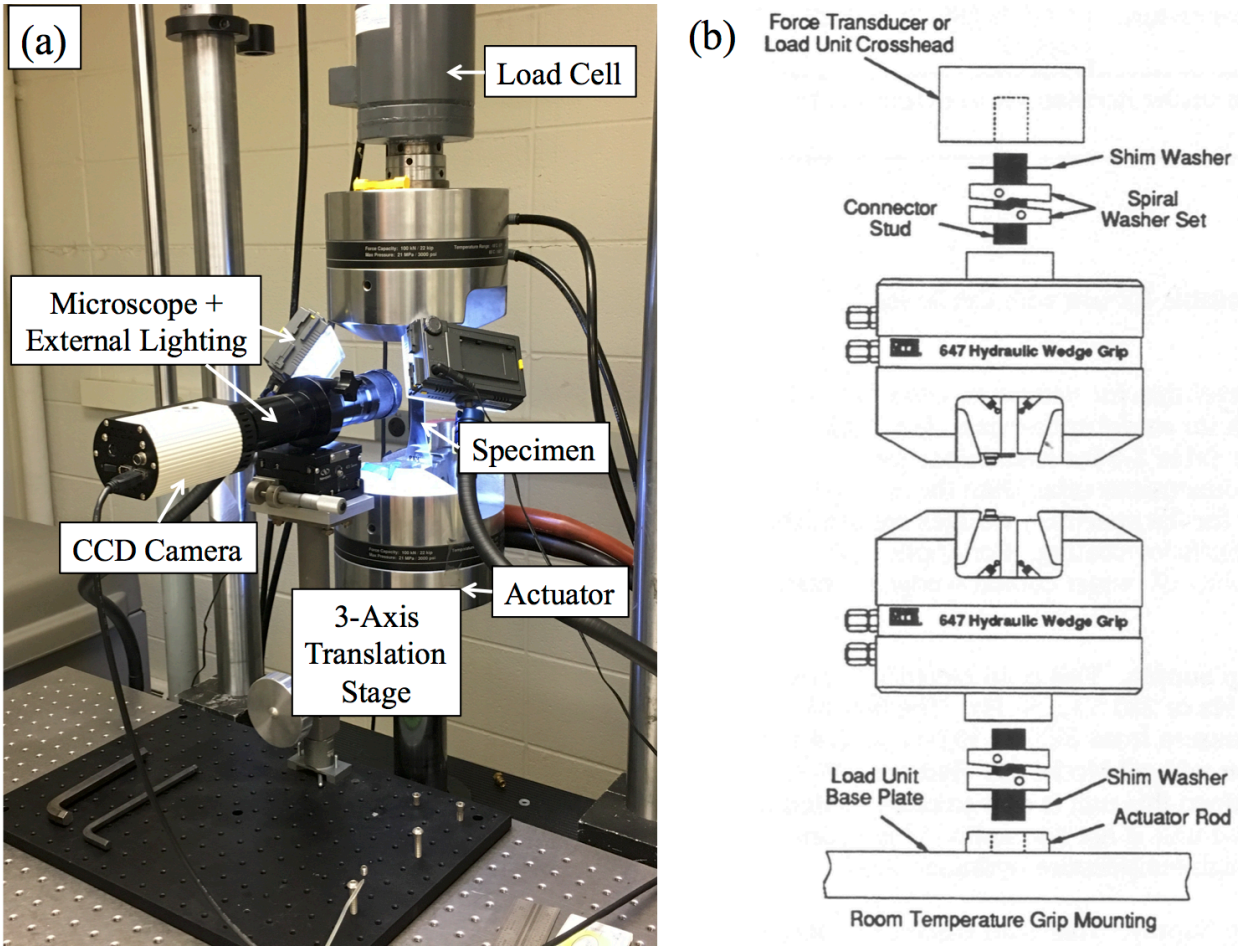

Figure 3.7 - MTS servohydraulic setup (a) Fatigue testing setup noting the camera and external lighting system and (b) schematic of the MTS wedge grips used for rectangular specimens [8].

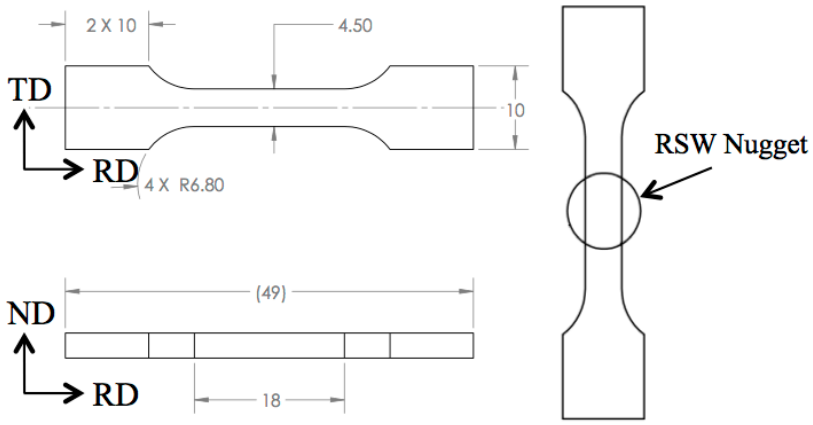

Figure 3.8 - Microtensile specimen geometry and RSW nugget location.

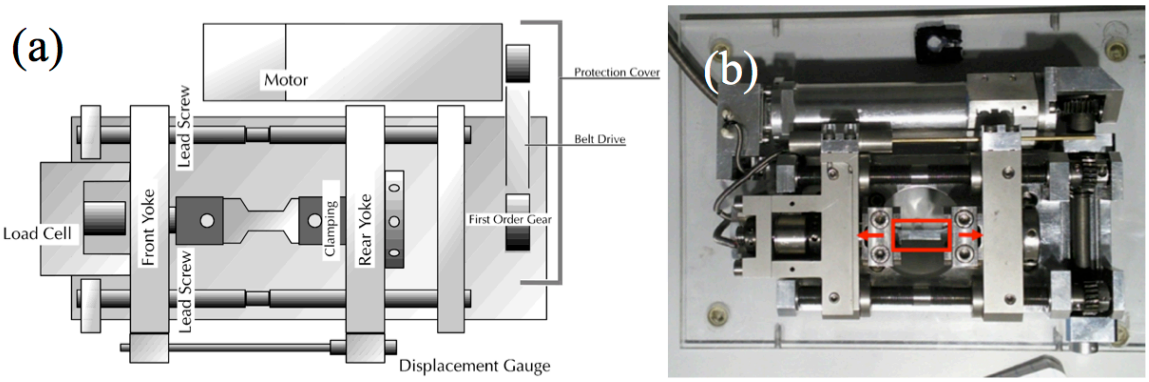

Figure 3.9 - Kammrath and Weiss tensile stage (a) Schematic of the setup [9] (b) Image of the actual setup [10].

Chapter 4

Short Fatigue Crack Growth In Wrought and Resistance Spot Welded Aluminum 5754 and 6111

This chapter describes the results of experimental short fatigue crack growth tests in wrought and resistance spot welded aluminum 6111 and 5754. The influence of alloying, heat treatment and weld-related microstructures are characterized. Applications and adjustments to a unified short crack model are also covered. Section 4.1 covers microstructural characterization and quantification of the parent and spot-welded materials using EBSD and microhardness analysis, along with the results of tensile testing. Section 4.2 presents the results of short fatigue crack growth testing, and observations from SEM and EBSD surface analysis and fractography. Section 4.3 uses the results from Section 4.2.2 and describes proposed changes to the unified short crack model to account for the pores found in the resistance spot welds. Finally, the results are discussed in Section 4.4 and conclusions are summarized in Section 4.5.

4.1 Microstructure Characterization

The wrought sheet alloys being studied in this study are aluminum alloys 5754 (Al-3Mg) and 6111 (Al-1Mg-1Si). The nominal composition of these alloys is listed in Table 4.1.

4.1.1 Parent Sheet Alloy Microstructures

Electron backscattered diffraction (EBSD) was used to characterize the grain shape, size and texture in 5754 and 6111 aluminum alloys. Representative micrographs of the microstructures of the TD-RD and ND-RD plane are shown in

Figure 4.1. The grain size for alloy 5754 has been quantified as 30 ± 8 μm in the TD and RD direction and 10 ± 3 μm in the ND direction. The grain size for alloy 6111 is 48 ± 12 μm in the TD and RD direction and 10 ± 4 μm in the ND direction. Both materials display grains that are elongated in the rolling direction due to plastic deformation from rolling. EDAX Orientation Imaging Microscopy (OIM) analysis has indicated that both materials exhibit weak rolled sheet crystallographic texture [1] with a maximum intensity of approximately 3.5 and 3 for alloys 5754 and 6111 respectively. These textures are relatively weak, and therefore it is assumed for this study that texture is not a factor in the short crack propagation behavior.

The primary heat treatment of interest in automotive aluminum alloy sheet is the paint-bake (PB) condition. During automotive production, after paint is applied, the vehicles are placed in an oven to expedite the drying and curing process [2]. The PB process has the additional benefit that is also produces an artificial age condition in age hardenable aluminum alloys such as 6111 Al. For the purposes of simulating this production process, an artificial aging treatment of 180°C for 30 minutes was used (see Figure 4.2). The Rockwell E hardness at this aging time was quantified as 89.02 ± 0.75 HRE. As alloy 5754 is a non-heat treatable alloy, any aging essentially acts as a low temperature anneal. The overaged (OA) aging condition of 6111 Al was also studied in order to understand the effects of an overaged microstructure (incoherent precipitates and homogenous slip distribution) on the short fatigue crack growth characteristics.

The overaging procedure (210°C for 12 hours) was used because it was found that achieving similar hardness and yield strength to the PB condition was not achievable at 180°C unless times longer than 100 hours were used. The Rockwell E hardness at this aging time was quantified as 89.35 ± 0.70 HRE, which was determined not to be significantly than the HRE for the PB 6111 condition. The Rockwell E hardness of the resistance spot welded 6111 (discussed more in the subsequent section) indicates that the weld is much softer than the parent material.

For this study, wrought 5754 aluminum was characterized in the PB heat treatment condition, while wrought 6111 specimens were tested in the T4, PB and OA conditions. Artificial aging was found to have no effect on the grain size, shape and texture.

4.1.2 Resistance Spot Welded Alloys

Resistance spot welding (RSW) is a joining process for metal sheets up to 3 mm thickness [3]. This process involves clamping two or more sheets between copper electrodes, represented schematically in Figure 4.3. Electrical current is then applied through the electrodes, generating heat due to the resistance to the flow of current offered by the aluminum sheets. The concentration of the heat melts the material in the center, forming a nugget that solidifies once the current is interrupted [4].

Optical micrographs with associated microhardness maps and EBSD of the highlighted regions (from the weld centerline to the parent material) are shown in Figure 4.4 (a) and (b) for spot welds in alloys 5754 and 6111 respectively. In spot welds, the material is melted and re-solidified, producing a cast dendritic microstructure: the weld fusion region from the center of the weld to approximately 500 μm from the weld-edge contains equiaxed grains. The region between the equiaxed zone of the weld and the parent material (approximately 500 μm long)

contains large, columnar grains that grow towards the center of the weld along the maximum temperature gradient, as exhibited in the EBSD maps for both alloys. The numbers underneath each region denote the average grain size for these regions.

For 5754 welds, hereafter 5754 RSW, the grain size in the center of the weld, where the cooling rate is at its highest and the smallest grain size is observed (36 μm equiaxed) is slightly larger than the parent material grain size of 30 μm x 10 μm x 10 μm. From the microhardness maps in 5754 RSW, there is no evidence that the weld matrix has different hardness than the parent material (65.5 ± 3.9 HV and 64.1 ± 3.2 HV respectively), but what is evident is the high amount of porosity. The spherical shape of the pores is indicative of gas porosity, likely due to the high Mg content of 5754, which increases the hydrogen solubility and leads to evolution of entrapped gas bubbles upon melting [5]. In addition, there is some evidence of shrinkage related porosity that is due to the volumetric contraction accompanying solidification (solid Al is ~7.1% denser liquid Al [6]). Qualitatively, it has been found that the area fraction of porosity in the 5754 RSW specimens is appreciably higher than the 6111 RSW specimens. These pores could not be indented for microhardness testing and display an HV of 0.

For 6111 RSW, the grain size in the center of the weld is smaller than the parent material (26 μm equiaxed vs. 48 μm x 10 μm x 10 μm). The microhardness maps indicate that the spot weld nugget is appreciably softer than the parent material, with a microhardness of 62.1 ± 3.1 HV compared to 90.7 ± 7.5 HV for the parent material. This is presumably due to the dissolution of strengthening precipitates during the material melting during the RSW process [7]. The artificial aging curve (Figure 4.2) displays an increase in strength during the PB treatment, indicating the growth of precipitates. The short temperatures and time, however, are not enough to strengthen this to the work hardened parent material.

A region is generally expected in between the weld and the parent material affected by the high temperature of the welding process known as the heat-affected zone (HAZ). Previous research on 6082-T6 aluminum MIG and GTA welding [8], 6061-T6 aluminum arc welding [9] and CO_2 laser beam welding [10,11] suggest residual heat causes a loss of strength in the HAZ due to coarsening and dissolution of strengthening precipitates in heat treatable alloys. However, in the case of resistance spot welds, a region of higher hardness is observed adjacent to the weld nugget, which is denoted as the thermomechanical affected zone (TMAZ). This term is normally associated with solid state welding processes such as friction stir welding [12–15] and linear friction welding [16–18] and this region is believed to exist due to the plasticity that results from the electrode indentation associated with the RSW process. This region, spanning an average 1mm from the weld nugget edge, exhibits a microhardness of approximately 72 HV compared to 65.5 ± 3.9 HV and 64.1 ± 3.2 HV for the weld nugget and parent material, respectively, in 5754 RSW. For 6111 RSW, this region exhibits a microhardness of 106.4 ± 5.4 HV, compared to 90.7 ± 7.5 HV and 62.1 ± 3.1 HV for the parent and spot welded region, respectively. From analysis of the EBSD maps, the TMAZ region exhibits the same microstructure as the parent alloys for both materials.

It is well known that residual stresses can appear in welded materials due to the interplay from the thermo-mechanical processes experienced during heating and cooling [4,19–21]. Quantification of the residual stresses in the fusion zone in spot welds was conducted on specimens used for crack growth testing. X-ray diffraction was performed at PROTO Manufacturing Inc. at Taylor, MI to measure the residual stress within the fusion zone. The results (Figure 4.5) indicate that the average residual stress is 21 MPa and is compressive. Florea et al. [19] performed residual stress measurements on 6061-T6 RSW joints and suggested that

residual stresses are insignificant if they are less than half of the parent material yield strength. For this study, the 21 MPa residual stress corresponds to approximately 8.5% of the parent 6111 Al yield strength and 18% of the 6111 RSW yield strength (discussed in the subsequent section). Therefore, for this study, we can consider the measured residual stress in the fusion zone insignificant and that residual stresses are not expected to bias the measured response of the short crack propagation behavior.

4.1.3 Mechanical Properties

Tensile testing was performed on the wrought aluminum alloys for each microstructural condition with the loading axis parallel to the rolling direction. The yield strength was determined using the 0.2% offset. Five specimens per material condition were tested to failure. Microtensile testing performed on nine 6111 RSW specimens were designed and manufactured via electro-discharge machining (EDM) such that the weld nugget occupied the gage section. Further details can found in Sections 3.3.2 and 3.3.3. The elastic modulus and yield strengths are tabulated in Table 4.2.

The mechanical properties of the TMAZ for the 6111 and the 5754 RSW could not be evaluated experimentally as microtensile specimens could not be fabricated to properly isolate these regions. The TMAZ region is thin and tensile specimens could not be manufactured in which the entire gage section was comprised of the TMAZ material. The appreciable porosity in the 5754 RSW center also created difficulties manufacturing proper microtensile specimens via EDM and thus these regions were also not tested in this study.

Càceres et al. [22] proposed that the relative change in yield strength can be estimated by a relative change of hardness. This method was utilized based on values obtained from the

microhardness maps. The microhardness of the TMAZ region adjacent to the weld nugget in alloy 6111 is 106.4 ± 5.4 HV compared to the 90.7 ± 7.5 HV for the parent PB material. The microhardness of the RSW 5754 weld nugget is 65.5 ± 3.9 HV, compared to the 64.1 ± 3.2 HV of the parent PB 5754. This leads to yield strength estimates of 289 and 102 MPa for the 6111 TMAZ and 5754 RSW regions, respectively. These estimations are included in Table 4.2.

The elastic modulus was found to be roughly constant, with an average value of 68 GPa; this is consistent with values from literature [23]. The yield strength varies with alloy and heat treatment. Wrought alloy 5754, primarily hardened through grain size, strain hardening and solid solution strengthening [24,25] , has the lowest yield strength. Wrought alloy 6111, primarily hardened through fine β'' precipitates [2,26–28] and Mn dispersoids [29–31] has a higher strength than PB 5754. For example, the yield strength of PB 6111 Al is 247 ± 2.6 MPa while the yield strength of PB 5754 Al is 105 ± 3.1 MPa.

4.2 Short Fatigue Crack Growth (SFCG)

Femtosecond laser notching was employed to place micronotches on the sheet specimen surface for crack initiation. Micronotches were placed in the center of the dogbone specimen irrespective of the local microstructure to understand the crack propagation behavior of physically short cracks. As depicted in Figure 4.6, micronotches were either placed in the center of the weld to characterize fatigue crack growth in the weld fusion zone (nugget) or within the TMAZ region adjacent to the weld fusion zone to characterize fatigue crack growth in the TMAZ. Crack growth measurements in the TMAZ were unable to be performed in 5754 RSW specimens as cracks initiated preferentially from porosity within the weld and not at micronotches. All SFCG specimens were fatigued at R = 0.1 at 30 Hz frequency.

4.2.1 SFCG in the Parent Sheet Material

For characterizing SFCG in the parent sheet materials, the maximum cyclic stress, σ_{max}, was chosen to be between 60% and 80% of yield strength. The crack growth rates of short cracks for the two alloys are displayed in Figure 4.7. The crack growth rates followed a power law relationship over the entire range of ΔK. This range of ΔK corresponds to a surface half-crack length of approximately 100 μm to 1 mm. One PB specimen of each alloy was tested at a maximum stress of 80 MPa (80% σ_{YS} for PB 5754 Al and 33% σ_{YS} for PB 6111 Al) up to a maximum half-crack length of approximately 1800 μm to observe the crack growth rates at ΔK values that were greater than 2.5 MPa $m^{1/2}$ for the 5754 Al and less than 2.5 MPa $m^{1/2}$ for the 6111 Al. This was done in order to quantify the nominal growth rates at ΔK values where the short crack growth testing for each material was performed. At these stress levels tested, the crack growth rates vary smoothly with increasing ΔK and crack arrests from crack front interactions with grain boundaries were not observed.

It has been observed that the growth rates for each alloy are similar for the differing specimens, heat treatments and stress levels tested. The short cracks display a linear trend in the log(da/dN) vs. log(ΔK) and a power law was fit to the data for each condition, presented in Table 4.3. There is a slight difference in the growth rates at the for 5754 Al and 6111 Al, as the 5754 Al has a power law exponent of 4.41 while the 6111 Al has an exponent of approximately 3.7.

In 6111 Al, the three heat treatments (T4, PB and OA) tested displayed similar short crack growth rates. The underaged, PB and OA heat treatment conditions, while having similar yield strengths, are expected to have different slip characteristics due the change in slip character from heterogeneous to homogenous deformation, altering the strain localization behavior.

Studies on long cracks for this type of change suggest OA alloys should display a flatter crack path [32] and higher growth rates [33–35]. However, these higher growth rates are generally not seen in short cracks [36] as the observed increase for long cracks is rationalized through crack closure effects. The power law coefficients indicate no statistically significant difference from one another, signifying no effect of heat treatment on the short crack propagation rate in 6111 Al. The 5754 Al specimen that was grown beyond the short crack threshold region shows slightly higher growth rates compared the 6111 parent materials. For the 6111 sample tested at lower growth rates, the initial propagation rates ($\Delta K < 1.75$ MPa $m^{1/2}$) are within the observed growth rates for 5754 Al, and the growth rates of the two alloys appear to diverge at $\Delta K > 1.75$ MPa $m^{1/2}$.

The crack path propagation behavior was investigated on specimen surfaces from a region within 500 μm of the micronotch using EBSD. Representative IPF micrographs are shown in Figure 4.8. The majority (>97%) of fatigue crack propagation occurred transgranularly in both alloys in all conditions, which has also been reported in other SFCG studies of aluminum alloys [37–39]. In the underaged, paint-baked conditions, cracks tended to deflect at grain boundaries to follow low index crystallographic planes, resulting in propagation away from the crack plane. The smaller grain size of PB 5754 resulted in smaller deviations, resulting in a much flatter crack path compared to the larger grained PB 6111. The OA 6111, in contrast to the PB 6111, displayed a much smaller degree of reorientation at grain boundaries, resulting in an overall flatter crack path. This result was expected due to the increase in the homogeneity of slip due to a loss of coherency of precipitates that occurs in overaged conditions [40].

Fractographic analysis was also performed for each alloy, with representative micrographs of regions adjacent to the micronotch (shown in Figure 4.9). In these regions there

is evidence of transgranular, crystallographic crack growth, with parallel features indicative of rough ductile tearing on the order of the grain size. The PB 5754 specimens exhibit a much more macroscopically smooth surface while the PB and OA 6111 display more tortuous surfaces due to the grain size differences.

4.2.2 SFCG in Resistance Spot Welded Regions

The short-crack growth rates for both the parent sheet, TMAZ and weld fusion regions of both alloys are presented in Figure 4.10. 6111 RSW specimens were tested at 80, 90 and 100 MPa, while TMAZ 6111 specimens were tested at 120 and 130 MPa because of the higher strength in the TMAZ region. The 5754 RSW specimens were tested at maximum stress levels between 40 and 50 MPa, and all of the specimens failed from a dominant fatigue crack that initiated from a large surface pore and not the micronotch. To characterize SFCG in these specimens, large view fields were utilized to monitor initiation from large pores. Once identified, crack growth rates from the dominant crack were calculated. Lower applied stress levels were used to assist in this process by ensuring that the naturally initiating crack was observed at the earliest possible interval.

Short crack propagation from the 6111 TMAZ region was observed to be slightly higher than the parent 6111 Al early in the short crack growth ($\Delta K \sim 2.6$ MPa $m^{1/2}$) but eventually converged with the parent short crack growth rate at $\Delta K = 4$ MPa $m^{1/2}$. This is attributed to propagation outside of the TMAZ region and into the base material. It was also observed that the short crack growth rates of 6111 TMAZ correspond well to the growth rate of the 5754 Al specimen grown beyond the short crack regime. EBSD analysis revealed no grain size difference between the TMAZ and parent materials, and there was no discernable difference in the fracture

surface compared to what was observed for the parent materials. SFCG data for the 5754 was not achievable because the dominant crack initiated from the pores in the weld region rather than the micronotch in the TMAZ region.

A high degree of variability in da/dN is often observed in the fatigue crack growth behavior of short cracks [41–44] due to the interaction of growing cracks with the underlying microstructure. However, in this case, the observed scatter in growth rates in the fusion zone are on the order of a 10x, much higher than was observed from the growth rates of the parent sheet and TMAZ regions. Furthermore, the short cracks are growing appreciably faster than the parent material. This is particularly pronounced for short cracks in the 5754 welds. The significant difference in growth rates between the parent and spot welded materials was an unexpected observation. The reason for this is believed to be due to interaction and coalescence with porosity present in the weld fusion zone. The effect of porosity on the fatigue crack initiation is well documented [45–47], but there is limited information on the effects of porosity on short crack growth.

Resistance Spot Welded 5754

For clarity, the SFCG rates of only the RSW and parent PB 5754 alloy are presented in Figure 4.11. As noted, the crack growth rates for short cracks in the RSW are appreciably higher than the parent material. The fatigue crack growth rate behavior is also much higher variability in the RSW condition compared with the parent condition. The high porosity present throughout the fusion zone provides sites that are favorable for crack initiation due to the increased stress concentration at the pore. Micronotches placed in the 5754 weld specimens, did not nucleate fatigue cracks for any of the specimens tested. Rather, cracks initiated from surface pores from which the short-crack propagation could be measured. Two examples of 5754 RSW specimens

that failed are presented in Figure 4.12 (S1 – σ_{max} = 45 MPa) and Figure 4.13 (S6 – σ_{max} = 50 MPa).

The initiating surface pore in these micrographs is marked with an arrow. As noted, cracks did not initiate from the micronotch, which is marked in the scanning electron micrographs. The micrograph was set at 200 μm, but the diameters of the initiating pores measured from on the surface for the examples presented are 87 μm and 101 μm for specimens S1 and S2, respectively. From the surface micrographs of the first sample (Figure 4.12 (a) and (b)), it is interesting to note that the crack did not propagate from the initiating pore towards the adjacent pore cluster less than 20 μm away. Observation of the surface crack path of the second sample (Figure 4.13 (a) and (b)) shows that the initiating pore is in a neighborhood with relatively few pores. Surface crack path analysis from EBSD maps found that the crack path is predominantly transgranular along crystallographic planes, with intergranular propagation sometimes present when propagating through porosity.

Scanning electron micrographs of the fracture surface are presented in Figure 4.12 (c)-(e) and Figure 4.13 (c)-(e). From the fracture surface overview, it can be seen that there exists a large amount of subsurface porosity. It is also qualitatively observed that the initiating pore is not the largest pore in the immediate vicinity. This suggests the observed porosity on the fracture surface is a significant factor affecting the propagation of short cracks.

Resistance Spot Welded 6111

In the 6111 RSW Al, short cracks initiated and propagated from the micronotches. The results for the RSW and parent 6111 conditions are presented in Figure 4.14. Compared to the 5754 RSW, the variability in crack growth rates in the 6111 RSW and the difference between

crack growth rates in the RSW versus the parent material is less appreciable. During and after the crack growth tests, the specimens were intermittently removed from the MTS frame and placed in the SEM to examine the interaction of the fatigue crack propagating from the micronotch and pores visible on the surface. Surface and fracture surface scanning electron micrographs of one such specimen of a 6111 spot weld (6111 RSW S15 – σ_{max} = 85 MPa) are presented in Figure 4.15 and Figure 4.16. In this sample, crack initiation occurred from a pore located approximately 700 μm from the notch (referred to as Pore 1) and coalesced with the short crack grown from the micronotch. The dominant crack from the micronotch also coalesced with a shrinkage pore (referred to as Pore 2), which was located approximately 205 μm from the end of the micronotch.

For Pore 1, crack initiation occurred from an area of visible porosity oriented at approximately 36° with respect to the loading direction. The earliest visible instance of propagation from the pore was at 2.15 million cycles after the start of testing, and propagated for an additional 1 million cycles before coalescing with the main crack. A marked drop in propagation rate was observed for the main crack prior to full coalescence with the crack initiated from the pore, leading to a drop in da/dN before a large increase in growth rate. While the length of the defect was measured to be ~ 47 μm on the surface, fracture surface examination of this region (Figure 4.16 (b) and (c)) showed a dendritic structure indicative of shrinkage porosity that spans approximately 209 μm in width and 56 μm deep.

For Pore 2, there was direct coalescence with the main crack propagating from the micronotch (Figure 4.15 (d)-(e)). This region was noted prior to fatigue testing due to its proximity and positioning on the macroscopic crack plane parallel to the micronotch. Limited propagation was observed solely from the pore, but there was eventual coalescence at 3.1 million

cycles, manifested by a local acceleration in da/dN. Fracture surface examination (Figure 4.16 (d) and (e)) of this pore shows dendritic features associated with shrinkage porosity, similar to Pore 1, which was approximately 59 μm in depth.

Measurements of fatigue crack growth for this research were only performed on the surface of the specimens. Fracture surface observations indicated that subsurface sites were crack initiators (such as the large pores present in the sheet center), likely coalescing with the overall dominant crack. Two additional regions from Figure 4.16 are identified, Pores 3 and 4, in Figure 4.17. Pore 3 displays a cluster of shrinkage pores approximately 370 μm from the specimen surface, the closest subsurface region where significant porosity was observed on the fracture surface. A region adjacent to the large pores present in the middle of the specimen is presented as Pore region 4 (Figure 4.17 (c)). River patterns were observed that "point" back to the defect cluster, indicative of crack initiation. Prior to and after fatigue crack growth testing, surface pores were cataloged in a 4mm x 4mm view field around the micronotch. The map from sample 6111 RSW S15 is presented in Figure 4.18 (a). More evidence of crack growth from pores was observed, primarily shown to be shrinkage porosity, with lengths ranging from 30μm to 240 μm. Some of the pores present in this figure appeared to be shrinkage porosity. The numbers of pores found in this view field for the 6111 RSW specimens tested are displayed in

Table 4.4. It was generally unclear if cracks propagated from these pores, but if it occurred it was limited to less than 100 μm. One such example is presented in Figure 4.18 (b) and (c). After initiation, the initiated crack propagated for approximately 20 μm before reorienting at a grain boundary and propagating for an additional 30 μm.

4.3 Adjustments To Unified Short Crack Model

As discussed in more detail in the literature review section, a unified short crack model proposed by Shyam et al. [48] is intended to account in a comprehensive way for microstructure, alloy, R-ratio and stress level effects on the short crack data for a wide range of engineering alloys. It is recognized that short crack growth is not completely captured by ΔK. For metals with large differences in strength, differences in the Paris intercept could be several orders of magnitude. The unified model, in contrast, utilizes crack tip displacement parameters as a means of more completely representing the plastic deformation phenomenon at the crack tip. Fatigue crack growth has been postulated [49] to be depend on two synergistic processes: damage accumulation and crack growth, both of which are accounted for in this model through the cyclic (ϕ_c) and monotonic (ϕ_m) crack-tip opening displacements, respectively:

[4.1] $$\phi_m = \frac{8\sigma_{YS}(1-\upsilon^2)a}{\pi E} ln\left(sec\left(\frac{\pi\sigma_{max}}{2\sigma_{YS}}\right)\right)$$

[4.2] $$\phi_c = \frac{16\sigma_{YS}(1-\upsilon^2)a}{\pi E} ln\left(sec\left(\frac{\pi\sigma_{max}(1-R)}{4\sigma_{YS}}\right)\right)$$

[4.3] $$\frac{da}{dN} = \mu\phi_m\phi_c\sigma_{YS}$$

Recall from Section 2.3 that the fitting parameter of the unified model, μ (damage susceptibility parameter), is proportional to the slip irreversibility (that is, the fraction of dislocations that contribute to extension of a fatigue crack [50]). The other variables associated with the μ, the geometric factor α and the critical displacement for crack extension Φ_{cr}, are assumed to be constant, and thus changes in μ are attributed to changes in slip irreversibility. It has been postulated [51,52] that solid solution strengthening (such as in 5754 Al) [53] and

overaging (OA 6111) produce microstructures that promote cross slip, thereby increasing the irreversibility of slip and reducing its resistance to crack growth. While this difference in crack growth was not observed for 6111 Al, it is feasible that a higher fraction of irreversibility is the cause of the faster observed growth rate for 5754 Al.

Using this parameter, the short crack data from the parent 5754 and 6111 aluminum tests are presented in Figure 4.19. The da/dN-ΔK data (Figure 4.7) displayed a slight difference in the short crack growth rates for 5754 Al and 6111 Al, which have different strengths (Table 4.2) and microstructures (Figure 4.1). Plotting the short crack growth rate vs. the short crack parameter (Figure 4.19) shows good agreement between the two alloys as the difference in yield strength and range of applied stress tested between the two alloys has been normalized. The values for the damage susceptibility parameter, μ (see Table 4.6), show an average μ for 5754 Al almost twice that of 6111 Al, but all four of the μ parameter for the parent materials are within one standard deviation. Nevertheless, the unified model has accounted for the differences observed using ΔK as a correlating parameter; for a given value of the short crack parameter, the differences in growth rates are indiscernible. Thus, for 5754 Al and 6111 Al, the short crack parameter provides a reasonable estimation for the short crack propagation response. Also included in Figure 4.19 is a line indicative of the predicted fit for the proposed linear relationship, with $\mu = 10^{-5}$ and a slope of 1 ($y = 10^{-5}x$). This relationship has been found to fit the short crack growth rate data for a wide variety of materials [48], from cast aluminum to the superalloy Rene' 88. At a given value of the unified parameter, the 6111 and 5754 Al crack growth data is slightly below but within the normal bounds (5x) for the description of this SFCG behavior.

The results from Section 4.2.2 signify a higher growth rate for the resistance spot welded regions for a given ΔK value, but the question remains whether the unified model could account

for this behavior. Using the unified short crack parameter, the short fatigue crack growth data from the resistance spot welded and parent conditions are presented in Figure 4.20. While there is good agreement between the parent materials, the distinction seen from the da/dN-ΔK plot still exists quite clearly for short crack growth behavior from the spot welded fusion zones.

The results in previous sections suggest that, within this region, crack interaction with welding porosity leads to the increased growth rate. Since porosity is a large scale feature it is not expected to affect slip irreversibility and thus is not accounted for by the unified parameter. Therefore, an adjustment to the unified model is proposed to account for this behavior, such that the crack growth rate and the unified parameter take into account the fraction of porosity. Identical adjustments can also be made to the normal SFCG rate vs. ΔK relationship; however, it is described here in the context of the unified parameter.

The unified model was adjusted by considering that the crack advances differently through the material matrix and porosity. When a crack tip encounters a pore, it is considered to instantaneously advance to the opposite side of the pore and thus "grow" the diameter of the pore. Furthermore, the presence of porosity increases the net section stress by reducing the average load bearing area. In the adjusted unified model, these effects are accounted for an on average basis using the pore volume fraction as the controlling parameter.

This adjustment in the unified model assumes that crack growth through the matrix dissipates energy while crack advance at a pore does not. This was accounted for by adjusting both the crack growth rate and the driving force using the area fraction of porosity (similar to a model proposed by Ghosh [54] to account for the effects of casting defects on tensile behavior), as described below. Experimentally, the crack growth was measured through optical

measurements of surface crack propagation, and thus an important aspect of this adjustment comes from splitting the measured crack length into these two components:

[4.4] $a_{measured} = a_{matrix} + a_{pore}$

The measured crack length ($a_{measured}$) is considered to be the sum of the growth through the fusion zone matrix (a_{matrix}), which is the intrinsic resistance to crack growth, and growth through the porosity (a_{pore}), which is considered to have no such resistance. To describe the steps taken to account for this porosity, the 5754 RSW S1 sample presented earlier is used as an example (in which the fraction of porosity measured was 50%). The delineation of growth through the matrix and porosity for this sample are shown in Figure 4.21.

The first step in the adjustment is to determine the fraction of porosity present in the short crack regime. For the spot welded specimens, fractographic scanning electron micrographs were used to measure the fraction of the projected fracture surface area comprised of porosity. From the fracture surface image, the following steps were performed (Figure 4.22):

- Each individual pore was isolated using Adobe® Photoshop (Figure 4.22 (a)) and the matrix portion of the fracture surface was removed (Figure 4.22 (b)).
- The region not associated with the short crack regime was removed from the micrograph (Figure 4.22 (c)). Masks were then created for each pore to give it a single color. This image was then analyzed in ImageJ, where the masked pores were quantified using the particle measurements module (Figure 4.22 (d)). This fits an ellipse to each individual masked pore.
- The area of each pore was quantified and the fraction of porosity, f, was then determined by summing the area of the pores ($A_{porosity}$) and normalizing by the area of the short-crack region (A_{SCArea}).

[4.5] $f = \frac{\sum A_{porosity}}{A_{SCArea}}$

Values of the quantified fraction of porosity, f, are tabulated in Table 4.5. The values show a range of porosity for the 5754 RSW specimens ranging from 43 to 52%, and a range for the 6111 RSW specimens ranging from 12 to 25%. This was confirmed qualitatively by visual examination that demonstrated that the fraction of porosity present in the 5754 spot welds is appreciably higher than in the 6111 spot welds.

The next step for adjusting the crack growth rate is to relate the fraction of porosity to the contribution of the measured crack length to growth through the matrix. This was accomplished based on several assumptions:

- An equivalent pore diameter can be calculated from the quantification of the total pore area for a given measured crack length:

[4.6] $\sum A_{pore} = \left(\frac{\pi}{2}\right) d_{pore,eff}^2$

- For every measured crack length, by assuming that cracks are perfectly semi-elliptical, a fracture surface area can be defined. On this fracture surface, the fraction of porosity is equivalent to the fraction measured previously and is given by:

[4.7] $f = \frac{\sum A_{pore}}{A_{total}} = \frac{\left(\frac{\pi}{2}\right) d_{pore,eff}^2}{\left(\frac{\pi}{2}\right) a_{measured}^2} = \left(\frac{d_{pore,eff}}{a_{measured}}\right)^2 = \left(\frac{a_{pore}}{a_{measured}}\right)^2$

- Using the relationship from Equation [4.7, the measured crack growth and crack advancement from pores can be defined by:

[4.8] $\frac{a_{pore}}{a_{measured}} = \sqrt{f} \therefore a_{pore} = a_{measured}\sqrt{f}$

- Equation [4.8 can be placed back into the original equation (Equation [4.4) to define a relationship for estimating crack growth through the matrix given the amount of measured crack growth on the specimen surface:

[4.9] $a_{matrix} = a_{measured}\left(1 - \sqrt{f}\right)$

From this relationship, for a given pore volume fraction, the crack growth in the matrix can be estimated for a given measured surface crack length, and a collection of measured crack length vs. cycles data can be converted into the crack growth in the matrix, da_{matrix}/dN, as shown in Figure 4.23.

The driving force parameter also requires a similar adjustment for crack growth through porous media. Recall from Equations [4.1 and [4.2 that the crack-tip opening displacements are functions of the crack length and applied stress. The crack length component does not change because it is purely a geometric term; that is, the crack length component was derived from the integration of the dislocation density over the plastic zone size and is given by the measured crack length. The applied stress term, however, does need to be modified to account for the reduction in net section area due to porosity.

To account for this, the assumption is made that the fraction of porosity measured in the short crack region is equivalent to the area fraction of porosity on the total weld fracture surface plane. The adjustment is then made to reduce the net area to account for the fraction of porosity. In the current investigation, dogbone specimens contained welds that spanned approximately 8 mm in diameter while the actual gage width was 18 mm as shown in Figure 4.24. The increase in stress due to the reduction in net section area from the weld section is given by:

[4.10] $\sigma'_{max} = \sigma_{max} \cdot \left(\frac{A_{total}}{A_{total} - f \cdot A_{weld}}\right)$

Plotting the fatigue crack growth rate through the matrix against the adjusted unified parameter (Figure 4.25) gives appreciably better agreement to the predicted trend. Crack propagation through the parent sheet does not experience porosity and thus no adjustment is necessary for those regions.

The adjusted modified model, adjusted for fatigue crack growth solely through the matrix, is as follows:

[4.11] $\frac{da_{matrix}}{dN} = \mu\left(1 - \sqrt{f}\right)\sigma_{ys}\phi'_m\phi'_c$

Where the adjusted crack-tip opening displacements are:

[4.12] $\phi'_m = \frac{8\sigma_{ys}(1-\nu^2)a_{measured}}{\pi E} \ln\left(\sec\left(\frac{\pi\sigma'_{max}}{2\sigma_{ys}}\right)\right)$

[4.13] $\phi'_c = \frac{16\sigma_{ys}(1-\nu^2)a_{measured}}{\pi E} \ln\left(\sec\left(\frac{\pi\sigma'_{max}(1-R)}{4\sigma_{ys}}\right)\right)$

Similar adjustments can be made to the da/dN-ΔK plot to quantify propagation rates through the matrix (see Figure 4.26). There exists better agreement between the parent material and the spot welded short crack growth rates, but the corrected spot weld growth rates are still observed to be slightly faster than the parent material growth rates.

4.4 Discussion

4.4.1 Short Crack Growth Behavior of Parent Sheet Metal

The short crack growth behavior of the 5754 and 6111 Al sheet materials were characterized to serve as a baseline for the RSW conditions. The short crack growth rates for both alloys (Figure 4.7) are similar for a given ΔK. For the 6111 Al specimens, no significant difference was observed for the three different heat treatments. There is no change in the grain size with each of these heat treatments, as the only changes are with the growth of fine β'' precipitates [2,26,27]. This is consistent with the work of Zaiken and Ritchie [32], who examined the effect of heat treatment on Al 7150 (Al-Zn) and observed that there were no discernible differences in crack growth rates in the Paris regime for underaged, peak-aged and overaged specimens. Interestingly, overaging increased the long crack propagation rates in 7055 Al [35] compared to the underaged condition. However, these observed differences were attributed to the difference in slip character and, ultimately, crack closure. Therefore, the difference in slip character is not expected to have an effect on the short crack growth behavior of 6111 Al, which is observed in this study.

The parent 5754 and 6111 Al alloys were also tested at different stress levels, and there were no observed changes in growth rate for differing applied stresses. Indeed, the growth rate for a given alloy is approximately the same in all parent conditions for a given ΔK value at R = 0.1. Short crack growth tests performed on Al 6082 [55], 304 stainless steel [56] and Ti-6Al-4V [57] at a R = 0.1 did not exhibit effects due to stress levels, which is consistent with this study. Other studies of short crack growth at R = -1 on 319 cast Al [58] and Ti-6Al-4V [59] have demonstrated a stress level dependence on the crack growth rate. Additionally, Newman and

Edwards [60] investigated short cracks in Al 2024-T3 and observed a stress level effect that increased with decreasing R ratio. Caton et al. [57] has suggested that this effect is due to the breakdown of ΔK as an appropriate correlating parameter. Thus, future studies on these alloys at different load ratios may indeed exhibit a stress level effect.

4.4.2 Short Crack Growth Behavior of Resistance Spot Welded Alloys

It is postulated that the increase in the observed short crack growth behavior in the fusion zone of the 5754 and 6111 welded materials is due to "direct" interaction of the crack front, with the crack front intersecting with porosity that is evident in the weld fusion zone. There are many studies on the effect of pores and oxide films on the analysis of fatigue life of engineering alloys, but little in the analysis of short crack propagation behavior. It has been shown that the fatigue life of smooth, un-notched specimens can be 1-2 orders of magnitude lower for cast or sintered alloys compared with the same alloys without casting pores [61–65]. This is analogous to the observed difference in growth rate of the spot welded materials compared with the wrought parent material, but porosity also affects the initiation lifetime and thus this analogy has limitations. It is found that in un-notched specimens, crack initiation lifetime decreases with increasing stress level [66,67]. While the applied stresses are nominally elastic, the amount and size of porosity visible on the 5754 weld and 6111 weld fracture surface produces a high enough of a stress concentration to result in a short initiation lifetime and thus crack propagation constitutes a majority of the total fatigue lifetime [68]. Therefore, for RSW conditions, it is likely that observed crack propagation rates are representative of the total fatigue behavior.

The porosity observed for both RSW conditions is believed to have influenced the propagation rates through direct and indirect interaction. For 5754 and 6111 weld specimens, the

high fraction of porosity observed on the fracture surface shows that pores directly intersect with the crack front. Moffat [69], in a study of fatigue mechanisms for Al-Si cast alloys, observed propagation between pores. This led to the conclusion that pores provide a "weak" path for crack propagation, and that propagation towards pores is beneficial in terms of the crack driving force. This was described in more detail by Piotrowski et al. [70] who suggested that the localization of strain and plasticity at the crack tip are enhanced with higher porosity, leading to lower thresholds for crack propagation to occur. Interconnected or clustered porosity, as observed in the 5754 welds, also creates a significant overlap of the plastic zones [71,72], which produces a favorable propagation path and acceleration in the crack growth rate. Therefore it can be inferred that the porosity observed in 5754 and 6111 welds provides an easier propagation path, as porous areas do not appear to offer intrinsic resistance to crack growth, resulting in the higher observed crack growth rates. Examination of the fracture surfaces for the 5754 welds (Figure 4.12 (c)-(e) and Figure 4.13 (c)-(e)) and the 6111 weld (Figure 4.16 (a)) revealed the higher fraction of porosity in the 5754 welds compared to the 6111 weld. This has been quantified in Table 4.5. It can be inferred then that since the porosity is not as high in the 6111 welds compared to 5754 welds the influence of porosity on crack growth rates is proportionally affected and thus the measured growth rates are higher in the 5754 welds compared to the 6111 welds due to differences in the pore area fraction.

In addition to significantly higher growth rates, SFCG in the fusion zone also exhibited high variability in the crack growth rates, up to one and a half orders of magnitude (Figure 4.10). This is believed to be due to propagation of the crack front through the matrix between the porous regions. Another explanation may be due to the coalescence of the fatal crack with the porosity. Tan et al. [73] used quantitative fractography to study the interaction of short surface cracks from

FIB notches located on the same macroscopic crack plane. The result showed a decrease in da/dN from surface measurements in order to facilitate a larger semi-elliptical crack shape and maintain its aspect ratio before growth before growth rates on the surface returned to normal. Thus, as crack growth rates are calculated from surface measurements, it is plausible that subsurface changes to the crack shape may be responsible for the cessations seen in the propagation rate. Further work utilizing X-ray computed tomography might be used to quantify the subsurface initiation and coalescence and more fully characterize the crack propagation characteristics of the resistance spot welded materials.

4.4.3 Unified Short Crack Model

As mentioned in the literature review, the advantage of utilizing the unified short crack parameter proposed by Shyam et al. [48] parameter is to have an initial reference condition for the response of short crack growths in existing and new structural alloys. Plotting the short crack growth rates of the wrought 5754 and 6111 Al vs. the unified parameter (see Figure 4.19) shows good agreement and accounts for the effect of yield strength and applied stress on. The values for the damage susceptibility parameter, μ, are considered to be solely proportional to the slip irreversibility (the fraction of dislocations that contribute to extension of a fatigue crack) for a given alloy system. It has been demonstrated that solid solution strengthening (such as in 5754 Al) [51,53], solute atoms preferentially segregate into the stress field around the dislocations, restricting dislocation motion and enhancing the propensity for cross-slip. For overaged alloys such as OA 6111 Al, the precipitates have lost their coherency and are no longer shearable by dislocations [23,52]. These microstructures pin dislocations and restrict dislocation motion, also increasing the propensity for cross slip. In both cases, strain localization is expected to be reduced and irreversibility increased. Thus, the increased propensity for cross slip will increase

the irreversibility of deformation and result in reduced crack growth resistance of a system [33]. This difference in growth rates is not observed for OA 6111, likely because the studies mentioned refer to long crack behavior where lower growth rates due to tortuosity displayed by underaged alloys is not present in the short crack regime. It is feasible that this is a mechanism for faster growth rates in 5754 Al, as μ (Table 4.6) shows an average μ for 5754 Al almost twice that of 6111 Al. The values for the four parent alloys, however, have been determined that the difference is not statistically significant, and thus it is unclear if there is an effect. Furthermore, the values of the slip irreversibility for each alloy and heat treatment have not been quantified for thus study. This would need to be done via measurement of slip offset via atomic force microscopy [74]. Thus, further research on materials where the irreversibility is quantified or controlled would ensure that the unified parameter properly accounts for this phenomenon. Nevertheless, the unified model has accounted for the divergence observed using ΔK as a correlating parameter and provides a reasonable estimation for the short crack propagation response.

As mentioned in the previous section, this alloy does not exhibit a stress level effect. Other research on short fatigue crack growth [58–60] investigated in 319 cast Al, Ti-6Al-4V and 2024-T3 has shown a stress level dependence that shows increasing growth rates with increasing stress amplitudes, primarily with $R \leq 0$. It has been suggested [57] that this is due to a breakdown in ΔK as a correlating parameters, and other solutions [75,76] have been proposed. The unified parameter is believed to accurately account for the stress level effect by normalizing the applied stress by the material yield strength. The original model proposal was able to reasonably correlate the growth rates for alloys of differing strength at load ratios of -1, 0.05 0.01 and 0.03.

Thus it is reasonable to believe that this model accounts for the stress level and R-ratio effects seen in short fatigue crack growth.

The results of short crack propagation tests suggests that the direct interaction between the crack front and porous areas enhance the propagation rates and are not adequately accounted for by the unified model. Other researchers have found that porosity can lead to a decrease in threshold values in a powder metallurgy steel [70] and enhance the monotonic (crack advance) portion of the fatigue crack growth process since porosity does not offer resistance to crack growth.

The adjustment to the unified parameter to account for these porosity effects (Equations [4.11 – [4.13) proposed in the current investigation appears to do well and, as presented in Figure 4.25, the majority of the adjusted weld fusion zone short crack data converges well within the scatter bands (indicating as half an order of magnitude from the predicted trendline). For the 6111 weld short crack growth rates, the data shifts considerably closer to the parent material, while for the 5754 weld growth rates, there is still large enough portion of the data that is appreciably higher than would be expected for crack growth purely through the matrix.

The deviation seen in 5754 welds is likely due to the limitations of the adjustment to porosity. Specifically, the assumption that fraction of porosity that exists on the fracture surface is constant throughout the short crack lifetime needs to be adjusted. This assumption does not consider the size, shape and spacing of the porosity, each of which has been found to alter the total fatigue life on porous metals [62,65,77]. Furthermore, Gall et al. [78] observed that microstructurally small cracks propagated nearly 2 orders of magnitude faster in AM60B magnesium for specimens that contained a “high” fraction of porosity. It was postulated that the

porosity has an “indirect” effect on growth rates, attributed to local amplification of the stress field from porosity adjacent to the crack front rather than “direct” propagation through a pore. It is feasible that the local amplification in growth rates is leading to higher growth rates than is being accounted for in the model adjustment. For the 6111 welds, this is found to be a reasonable approximation, but as noted earlier the overall fraction of porosity is lower in 6111 welds compared to 5754 welds and thus has a higher sensitivity to the porosity as the short crack progresses.

4.5 Conclusions

To understand the crack propagation behavior of spot welds in aluminum alloys, physically short fatigue crack growth testing was performed on wrought and resistance spot welded 5754 and 6111 aluminum. The wrought parent alloys exhibited similar crack propagation rates for a given driving force, despite variability in alloying, heat treatment, stress level, and crack path. Short cracks propagating in the RSW regime, however, display appreciably higher growth rates for a given driving force. This is due to the direct interaction between the crack front and the porosity present in the weld. Fracture surface analysis revealed that the 5754 spot welds have between 43 and 52% porosity fraction, while the 6111 spot welds display between 12 and 25% porosity fraction. This differences in observed porosity yielded higher growth rates for 5754 welds relative to the parent material for the 6111 weld and compared to their respective parent materials. Short cracks in spot welded 5754 specimens exhibited growth rates up to two orders of magnitude higher than the parent material.

A unified short crack model was applied which has captured the observed fatigue crack growth behavior in a wide variety of engineering alloys. Adjustments to the model are proposed

to account for the effect of porosity. The measured crack growth rate is modified to display growth solely through the material matrix and the driving force is adjusted to account for the reduction in net section area due to the porosity. These modifications showed good agreement with the predicted trend, and thus the unified model can be used for both sheet Al alloys and resistance spot welds in these sheet Al alloys.

References

[1] Hirsch J, Lücke K. Mechanism of deformation and development of rolling textures in polycrystalline FCC metals I. description of rolling tecture development in homogeneous CuZn alloys. Acta Metall 1988;36:2863–82. doi:10.1016/0001-6160(88)90172-1.

[2] Esmaeili S, Wang X, Lloyd DJ, Poole WJ. On the Precipitation-Hardening Behavior of the Al-Mg-Si-Cu Alloy AA6111. Metall Mater Trans A 2003;34A:751–63.

[3] Weman K. Pressure welding methods. Weld. Process. Handb. 2nd ed., 2012, p. 119–32. doi:10.1533/9780857095183.119.

[4] Zhang H, Senkara J. Resistance Welding: Fundamentals and Applications. vol. 65. 2nd ed. Boca Raton: 2006. doi:10.1017/CBO9781107415324.004.

[5] Senkara J, Zhang H. Cracking in Spot Welding Aluminum Alloy AA5754. Weld Reseach 2000.

[6] Campbell J. Porosity. Complet. Cast. Handb., 2015, p. 341–415. doi:10.1016/B978-0-444-63509-9.00007-8.

[7] Wu SN, Ghaffari B, Hetrick E, Li M, Jia ZH, Liu Q. Microstructure characterization and quasi-static failure behavior of resistance spot welds of AA6111-T4 aluminum alloy. Trans Nonferrous Met Soc China (English Ed 2014;24:3879–85. doi:10.1016/S1003-6326(14)63546-9.

[8] Myhr OR, Grong Ø. Process modelling applied to 6082-T6 aluminium weldments—II. Applications of model. Acta Metall Mater 1991;39:2703–8. doi:10.1016/0956-7151(91)90086-G.

[9] Enjo T, Kuroda T. Microstructure in Weld Heat Affected Zone of Al-Mg-Si Alloy. Trans JWRI 1982;11:61–6.

[10] Hirose A, Kobayashi KF, Todaka H. CO2 laser beam welding of 6061-T6 aluminum alloy thin plate. Metall Mater Trans A 1997;28:2657–62. doi:10.1007/s11661-997-0022-9.

[11] Hirose A, Kurosawa N, Kobayashi KF, Todaka H, Yamaoka H. Quantitative evaluation of softened regions in weld heat-affected zones of 6061-T6 aluminum alloy—Characterizing of the laser beam welding process. Metall Mater Trans A 1999;30:2115–20. doi:10.1007/s11661-999-0022-z.

[12] Fonda RW, Bingert JF, Colligan KJ. Development of grain structure during friction stir welding. Scr Mater 2004;51:243–8. doi:10.1016/j.scriptamat.2004.04.017.

[13] Dai Q, Liang Z, Chen G, Meng L, Shi Q. Explore the mechanism of high fatigue crack propagation rate in fine microstructure of friction stir welded aluminum alloy. Mater Sci Eng A 2013;580:184–90. doi:10.1016/j.msea.2013.05.057.

[14] Prangnell PB, Heason CP. Grain structure formation during friction stir welding observed by the "stop action technique." Acta Mater 2005;53:3179–92.

doi:10.1016/j.actamat.2005.03.044.

[15] Geuser F De, Bley F, Denquin A, Deschamps A. Mapping the microstructure of a friction-stir welded (FSW) Al-Li-Cu alloy. J Phys Conf Ser 2010;247:1–7. doi:10.1088/1742-6596/247/1/012034.

[16] Wanjara P, Jahazi M. Linear friction welding of Ti-6Al-4V: Processing, microstructure, and mechanical-property inter-relationships. Metall Mater Trans A 2005;36:2149–64. doi:10.1007/s11661-005-0335-5.

[17] Ma TJ, Li W-Y, Yang SY. Impact toughness and fracture analysis of linear friction welded Ti–6Al–4V alloy joints. Mater Des 2009;30:2128–32. doi:10.1016/j.matdes.2008.08.029.

[18] Vishwakarma KR, Ojo OA, Wanjara P, Chaturvedi MC. Microstructural Analysis of Linear Friction-Welded 718 Plus Superalloy. JOM 2014;66:2525–34. doi:10.1007/s11837-014-0938-7.

[19] Florea RS, Hubbard CR, Solanki KN, Bammann DJ, Whittington WR, Marin EB. Quantifying residual stresses in resistance spot welding of 6061-T6 aluminum alloy sheets via neutron diffraction measurements. J Mater Process Technol 2012;212:2358–70. doi:10.1016/j.jmatprotec.2012.06.024.

[20] Zerbst U, Ainsworth R a., Beier HT, Pisarski H, Zhang ZL, Nikbin K, et al. Review on fracture and crack propagation in weldments – A fracture mechanics perspective. Eng Fract Mech 2014;132:200–76. doi:10.1016/j.engfracmech.2014.05.012.

[21] Ertas AH, Sonmez FO. Design optimization of spot-welded plates for maximum fatigue life. Finite Elem Anal Des 2011;47:413–23. doi:10.1016/j.finel.2010.11.003.

[22] Cáceres CH, Griffiths JR, Pakdel AR, Davidson CJ. Microhardness mapping and the hardness-yield strength relationship in high-pressure diecast magnesium alloy AZ91. Mater Sci Eng A 2005;402:258–68. doi:10.1016/j.msea.2005.04.042.

[23] Ashby MF, Jones DRHDRH. Engineering Materials 1. Eng Mater 1 1996:322. doi:10.1016/B978-0-08-096665-6.00030-1.

[24] Holtz RL, Pao PS, Bayles RA, Longazel TM, Goswami R. Corrosion-fatigue behavior of aluminum alloy 5083-H131 sensitized at 448 K (175 C). Metall Mater Trans A Phys Metall Mater Sci 2012;43:2839–49. doi:10.1007/s11661-011-0866-x.

[25] Shi Y, Guo H. Fatigue performance and fatigue damage parameter estimation of spot welded joints of aluminium alloys 6111-T4 and 5754. Fatigue Fract Eng Mater Struct 2013;36:1081–90. doi:10.1111/ffe.12089.

[26] Wang X, Poole WJ, Esmaeili S, Lloyd DJ, Embury JD. Precipitation Strengthening of the Aluminum Alloy AA6111. Metall Mater Trans A 2003;34A:2913–24.

[27] Quainoo GK, Yannacopoulos S. Natural Aging Behavior of AA6111 Aluminum. Ghana J Sci 2007;47:91–100.

[28] Bryant JD. The Effects of Preaging Treatments on Aging Kinetics and Mechanical Properties in AA6111 Aluminum Autobody Sheet. Metall Mater Trans A 1999;30A.

[29] Lee DH, Park JH, Nam SW. Enhancement of mechanical properties of Al-Mg-Si alloys by means of manganese dispersoids. Mater Sci Technol 1999;15:450–5.

[30] Nam S, Lee D. The effect of Mn on the mechanical behavior of Al alloys. Met Mater 2000;6:13–6. doi:10.1007/bf03026339.

[31] Edwards L, Busby AK, Martin JW. Effect of aging and dispersoid content on fatigue crack growth of in Al-Mg-Si alloys. Mater Sci Technol 1986;2:823–8.

[32] Zaiken E, Ritchie RO. Effects of microstructure on fatigue crack propagation and crack closure behavior in aluminum alloy 7150. Mater Sci Eng 1985;70:151–60. doi:10.1016/0025-5416(85)90276-9.

[33] Hornbogen E, Gahr Z. Microstructure and Fatigue Crack Growth in a y-Fe-Ni-Al Alloy. Acta Metall 1975;24:581–92.

[34] C.W. B, J.E. K, M.A. H. Effects of microstructure on long and short cracks at a sharp notch. Met Sci 1984;18:374–80.

[35] Chen JZ, Zhen L, Yang SJ, Dai SL. Effects of precipitates on fatigue crack growth rate of AA 7055 aluminum alloy. Trans Nonferrous Met Soc China (English Ed 2010;20:2209–14. doi:10.1016/S1003-6326(10)60630-9.

[36] Larsen JM, Williams JC, Thompson AW. Crack-Closure Effects on the Growth of Small Surface Cracks in Titanium-Aluminum Alloys. Mech. Fatigue Crack Closure, ASTM STP 982, 1988, p. 149–67.

[37] Zhai T, Jiang XP, Li JX, Garratt MD, Bray GH. The grain boundary geometry for optimum resistance to growth of short fatigue cracks in high strength Al-alloys. Int J Fatigue 2005;27:1202–9. doi:10.1016/j.ijfatigue.2005.06.021.

[38] Haigen J, Zhimin Y, Feng J, Xue L. EBSD Analysis of Fatigue Crack Growth of 2124 Aluminum Alloy for Aviation. Rare Met Mater Eng 2014;43:1332–6. doi:10.1016/S1875-5372(14)60118-1.

[39] Jian H, Jiang F, Wei L, Zheng X, Wen K. Crystallographic mechanism for crack propagation in the T7451 Al-Zn-Mg-Cu alloy. Mater Sci Eng A 2010;527:5879–82. doi:10.1016/j.msea.2010.05.063.

[40] Bolingbroke RK, King JE. A comparison of long and short fatigue crack growth in a high strength aluminum alloy. In: Miller K., De Los Rios ER, editors. Behav. Short Fatigue Cracks, London: Mechanical Engineering Publications; 1986, p. 101.

[41] Miller KJ. the Short Crack Problem. Fatigue Fract Eng Mater Struct 1982;5:223–32. doi:10.1111/j.1460-2695.1982.tb01250.x.

[42] Lankford J. The Influence of Microstructure on the Growth of Small Fatigue Cracks. Fatigue Fract Eng Mater Struct 1985;8:161–75.

[43] Suresh S, Ritchie RO. Propagation of short fatigue cracks. Int Met Rev 1984;29:445–76. doi:10.1179/imtr.1984.29.1.445.

[44] Suresh S. Fatigue of Materials. Cambridge University Press; 1998. doi:10.1017/CBO9780511806575.

[45] Yi JZ, Gao YX, Lee PD, Flower HM, Lindley TC. Scatter in fatigue life due to effects of porosity in cast A356-T6 aluminum-silicon alloys. Metall Mater Trans A 2003;34:1879–90. doi:10.1007/s11661-003-0153-6.

[46] Caton MJ, Jones JW, Mayer H, Stanzl-Tschegg S, Allison JE. Demonstration of an endurance limit in cast 319 aluminum. Metall Mater Trans A 2003;34:33–41. doi:10.1007/s11661-003-0206-x.

[47] Boileau JM, Allison JE. The effect of solidification time and heat treatment on the fatigue properties of a cast 319 aluminum alloy. Metall Mater Trans A 2003;34:1807–20. doi:10.1007/s11661-003-0147-4.

[48] Shyam A, Allison JE, Szczepanski CJ, Pollock TM, Jones JW. Small fatigue crack growth in metallic materials: A model and its application to engineering alloys. Acta Mater 2007;55:6606–16. doi:10.1016/j.actamat.2007.08.022.

[49] Vasudeven AK, Sadananda K, Louat N. A review of crack closure, fatigue crack threshold and related phenomena. Mater Sci Eng A 1994;188:1–22. doi:10.1016/0921-5093(94)90351-4.

[50] Shyam A, Allison JE, Jones JW. A small fatigue crack growth relationship and its application to cast aluminum. Acta Mater 2005;53:1499–509. doi:10.1016/j.actamat.2004.12.004.

[51] Brosi JK. Mechanical property evolution of Al-Mg alloys following immediate temperature thermal exposure. Case Western Reserve University, 2010.

[52] Poole WJ, Wang X, Lloyd DJ, Embury JD. The shearable–non-shearable transition in Al–Mg–Si–Cu precipitation hardening alloys: implications on the distribution of slip, work hardening and fracture. Philos Mag 2005;85:3113–35. doi:10.1080/14786430500154935.

[53] Wei RP, Gangloff RP. Fracture Mechanics: Perspectives and Directions (twentieth Symposium). 100 Barr Harbor Drive, PO Box C700, West Conshohocken, PA 19428-2959: ASTM International; 1989. doi:10.1520/STP1020-EB.

[54] Ghosh A. Tensile instability and necking in materials with strain hardening and strain-rate hardening. Acta Metall 1977;25:1413–24. doi:10.1016/0001-6160(77)90072-4.

[55] Güngör S, Edwards L. Effect of Surface Texture on Fatigue Life in a Squeeze-Cast 6082 Aluminium Alloy. Fatigue Fract Eng Mater Struct 1993;16:391–403. doi:10.1111/j.1460-2695.1993.tb00095.x.

[56] Deng GJ, Tu ST, Wang QQ, Zhang XC, Xuan FZ. Small fatigue crack growth mechanisms of 304 stainless steel under different stress levels. Int J Fatigue 2014;64:14–21. doi:10.1016/j.ijfatigue.2014.01.027.

[57] Caton MJ, John R, Porter WJ, Burba ME. Stress ratio effects on small fatigue crack growth in Ti-6Al-4V. Int J Fatigue 2012;38:36–45. doi:10.1016/j.ijfatigue.2011.11.004.

[58] Caton MJ, Jones JW, Boileau JM, Allison JE. The effect of solidification rate on the growth of small fatigue cracks in a cast 319-type aluminum alloy. Metall Mater Trans A 1999;30:3055–68. doi:10.1007/s11661-999-0216-4.

[59] Hines JA, Lütjering G. Propagation of microcracks at stress amplitudes below the conventional fatigue limit in Ti-6Al-4V. Fatigue Fract Eng Mater Struct 1999;22:657–65. doi:10.1046/j.1460-2695.1999.00217.x.

[60] Newman JCJ, Edwards PR. Short-crack growth behaviour in an aluminum alloy - an Agard cooperative test programme. 1988.

[61] Ammar HR, Samuel AM, Samuel FH. Effect of casting imperfections on the fatigue life of 319-F and A356-T6 Al-Si casting alloys. Mater Sci Eng A 2008;473:65–75. doi:10.1016/j.msea.2007.03.112.

[62] Wang QG, Apelian D, Lados DA. Fatigue behavior of A356-T6 aluminum cast alloys. Part I. Effect of casting defects. J Light Met 2001;1:73–84. doi:10.1016/S1471-5317(00)00008-0.

[63] Wang QG, Davidson CJ, Griffiths JR, Crepeau PN. Oxide Films, Pores and the Fatigue Lives of Cast Aluminum Alloys 2006;37.

[64] Nayhumwa C, Green NR, Campbell J. Influence of casting technique and hot isostatic pressing on the fatigue of an Al-7Si-Mg alloy. Metall Mater Trans A 2001;32:349–58. doi:10.1007/s11661-001-0266-8.

[65] Chawla N, Williams JJ. Fatigue and fracture of powder metallurgy steels. In: Chang I, Zhao Y, editors. Adv. Powder Metall. Prop. Process. Appl. 2nd ed., Woodhead Publishing ; 2013, p. 455–90.

[66] Chawla N, Andes C, Davis LC, Allison JE, Jones JW. The interactive role of inclusions and SiC reinforcement on the high-cycle fatigue resistance of particle reinforced metal matrix composites. Metall Mater Trans A 2000;31:951–7. doi:10.1007/s11661-000-0037-y.

[67] Polasik SJ, Williams JJ, Chawla N. Fatigue crack initiation and propagation of binder-treated powder metallurgy steels. Metall Mater Trans A 2002;33:73–81. doi:10.1007/s11661-002-0006-8.

[68] Couper MJ, Neeson AE, Griffiths JR. Casting defects and the fatigue behavior of an aluminum casting alloy. Fatigue Fract Eng Mater Struct 1990;13:213–27. doi:10.1111/j.1460-2695.1990.tb00594.x.

[69] Moffat AJ. Micromechanistic analysis of fatigue in aluminium silicon casting alloys, Phd Thesis 2007:p274.

[70] Piotrowski G, Deng X, Chawla N, Narasimhan KS, Marucci M. Fatigue-Crack Growth Of Fe-0. 85 Mo-2 Ni-01. 6 C Steels With A Heterogeneous Microstructure. Int J Powder

Metall 2005;41:31–41.

[71] Gerard DA, Koss DA. The influence of porosity on short fatigue crack growth at large strain amplitudes. Int J Fatigue 1991;13:345–52. doi:10.1016/0142-1123(91)90364-5.

[72] Gerosa R, Rivolta B, Tavasci A, Silva G, Bergmark A. Crack initiation and propagation in Chromium pre-alloyed PM-steel under cyclic loading. Eng Fract Mech 2008;75:750–9. doi:10.1016/j.engfracmech.2007.01.009.

[73] Tan JT, Chen BK. Coalescence and growth of two coplanar short cracks in AA7050-T7451 aluminium alloys. Eng Fract Mech 2013;102:324–33. doi:10.1016/j.engfracmech.2013.03.002.

[74] Shyam A, Milligan WW. A model for slip irreversibility, and its effect on the fatigue crack propagation threshold in a nickel-base superalloy. Acta Mater 2005;53:835–44. doi:10.1016/j.actamat.2004.10.036.

[75] Hironobu N, Masahiro G, Norio K. A small-crack growth law and its related phenomena. Eng Fract Mech 1992;41:499–513. doi:10.1016/0013-7944(92)90297-R.

[76] Shyam A, Picard YN, Jones JW, Allison JE, Yalisove SM. Small fatigue crack propagation from micronotches in the cast aluminum alloy W319. Scr Mater 2004;50:1109–14. doi:10.1016/j.scriptamat.2004.01.031.

[77] Nicoletto G, Anzelotti G, Konečná R. X-ray computed tomography vs. metallography for pore sizing and fatigue of cast Al-alloys. Procedia Eng 2010;2:547–54. doi:10.1016/j.proeng.2010.03.059.

[78] Gall K, Biallas G, Maier HJ, Horstemeyer MF, McDowell DL. Environmentally influenced microstructurally small fatigue crack growth in cast magnesium. Mater Sci Eng A 2005;396:143–54. doi:10.1016/j.msea.2005.01.014.

Tables

Table 4.1 - Composition of Aluminum Alloys 5754 and 6111

Alloy	Mg (%)	Si (%)	Cu (%)	Mn (%)	Fe (%)	Ti (%)	Al (%)
5754	3	0.4	-	0.5	0.4	0.1	Bal.
6111	1	1	0.5	0.4	0.4	0.1	Bal.

Table 4.2 - Elastic modulus and yield strength for materials tested. (* calculated from microhardness comparison [22])

Material	Elastic Modulus (GPa)	Yield Strength (MPa)
PB 5754	65.7 ± 2.1	105 ± 3.1
T4 6111	69.3 ± 2.5	179 ± 1.4
PB 6111	68.4 ± 1.9	247 ± 2.6
OA 6111	70.1 ± 2.4	250 ± 2.4
PB 6111 RSW	65.7 ± 3.5	117 ± 8.2
6111 TMAZ *	-	289
PB 5754 RSW*	-	107

Table 4.3 - da/dN vs. ΔK power law fit components short cracks growing in wrought aluminum 5754 and 6111 ($da/dN = C(\Delta K)^n$)

Material	C	n
PB 5754	$2.22 \times 10^{-11} \pm 1.89 \times 10^{-12}$	$4.41 \pm 1.39 \times 10^{-1}$
T4 6111	$3.51 \times 10^{-11} \pm 1.25 \times 10^{-11}$	$3.57 \pm 1.92 \times 10^{-1}$
PB 6111	$2.54 \times 10^{-11} \pm 1.50 \times 10^{-11}$	$3.82 \pm 3.10 \times 10^{-1}$
OA 6111	$3.01 \times 10^{-11} \pm 1.74 \times 10^{-12}$	$3.60 \pm 6.07 \times 10^{-2}$
6111 TMAZ	$6.69 \times 10^{-10} \pm 2.67 \times 10^{-11}$	$1.78 \pm 3.51 \times 10^{-2}$
5754 RSW (pre-adjustment)	$2.80 \times 10^{-9} \pm 1.13 \times 10^{-9}$	$3.96 \pm 5.38 \times 10^{-1}$
6111 RSW (pre-adjustment)	$1.75 \times 10^{-10} \pm 6.40 \times 10^{-11}$	$3.63 \pm 4.12 \times 10^{-1}$
5754 RSW (post-adjustment)	$7.05 \times 10^{-10} \pm 2.91 \times 10^{-10}$	$3.96 \pm 5.38 \times 10^{-1}$
6111 RSW (post-adjustment)	$8.33 \times 10^{-11} \pm 3.33 \times 10^{-12}$	$3.63 \pm 4.12 \times 10^{-1}$

Table 4.4 - Number of surface welding defects observed in 4x4mm view field around micronotch for RSW 6111 specimens (defect size > 30 μm)

Sample	Surface Defects Observed
6111 RSW S14	23
6111 RSW S15	32
6111 RSW S21	12
6111 RSW S28	18

Table 4.5 - Measured fraction of porosity in the short crack regime for resistance spot welded alloys tested.

Sample	Fraction Porosity
5754 RSW S1	0.5
5754 RSW S6	0.43
5754 RSW S10	0.52
5754 RSW S12	0.49
6111 RSW S14	0.25
6111 RSW S15	0.15
6111 RSW S21	0.22
6111 RSW S28	0.12

Table 4.6 - Fitting parameters for the unified short crack model ($da/dN = \mu(\Phi_m\Phi_c\sigma_{YS})^m$)

Material	μ	m
PB 5754	$2.51 \times 10^{-5} \pm 8.21 \times 10^{-6}$	$1.35 \pm 5.09 \times 10^{-2}$
T4 6111	$1.57 \times 10^{-5} \pm 1.26 \times 10^{-6}$	$0.93 \pm 5.42 \times 10^{-2}$
PB 6111	$1.41 \times 10^{-5} \pm 3.89 \times 10^{-6}$	$1.08 \pm 8.99 \times 10^{-2}$
OA 6111	$1.29 \times 10^{-5} \pm 6.73 \times 10^{-7}$	$0.92 \pm 1.62 \times 10^{-2}$
6111 TMAZ	$2.88 \times 10^{-7} \pm 2.30 \times 10^{-8}$	$0.47 \pm 8.40 \times 10^{-3}$
5754 RSW (pre-adjustment)	$4.26 \times 10^{-4} \pm 3.92 \times 10^{-4}$	$1.03 \pm 1.47 \times 10^{-1}$
6111 RSW (pre-adjustment)	$1.10 \times 10^{-4} \pm 1.04 \times 10^{-4}$	$0.93 \pm 1.40 \times 10^{-1}$
5754 RSW (post-adjustment)	$3.14 \times 10^{-5} \pm 2.72 \times 10^{-5}$	$1.03 \pm 1.47 \times 10^{-1}$
6111 RSW (post-adjustment)	$4.82 \times 10^{-5} \pm 4.03 \times 10^{-5}$	$0.93 \pm 1.40 \times 10^{-1}$

Images

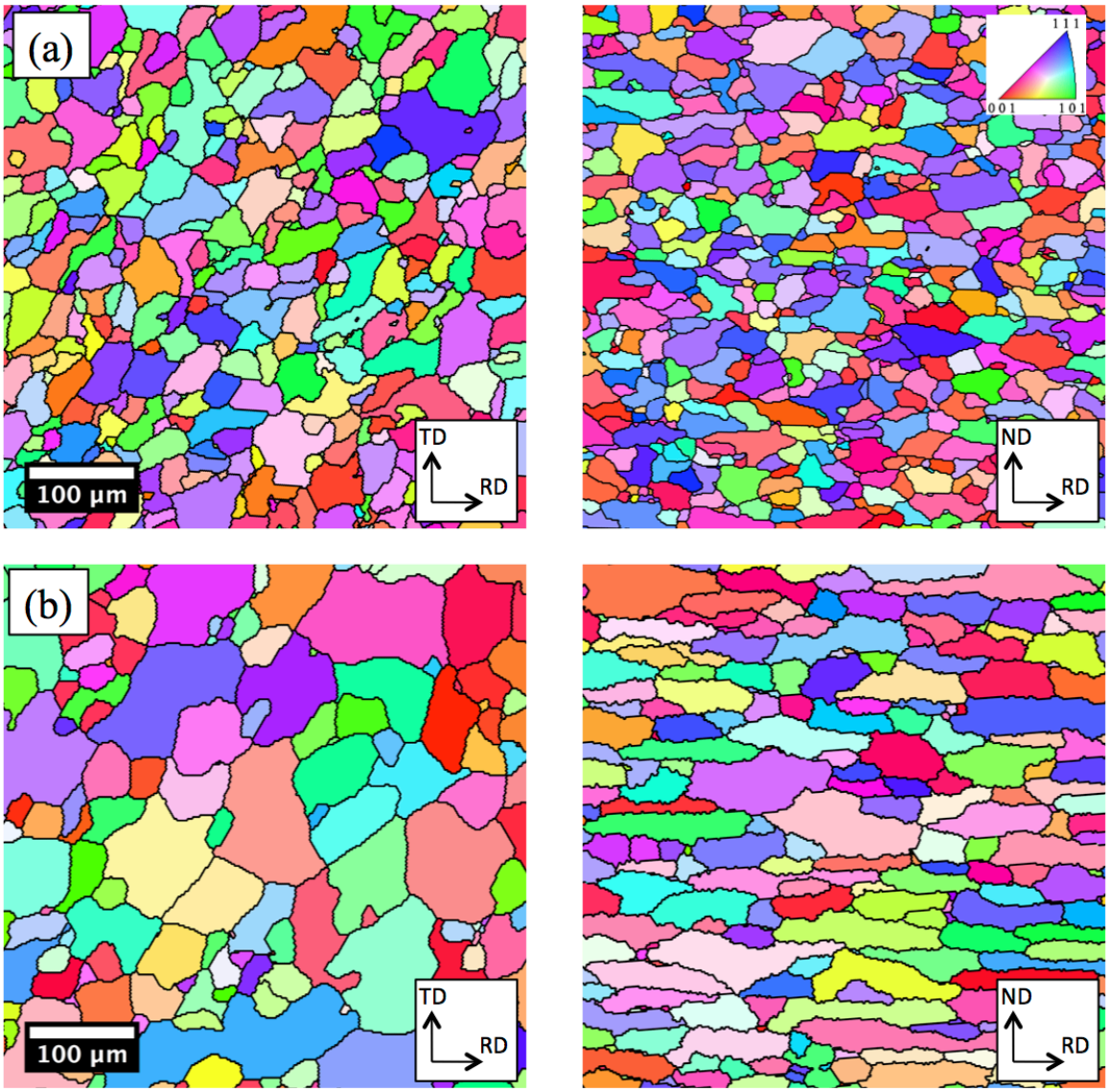

Figure 4.1 - Representative EBSD micrographs of the aluminum alloys being studied (500 x 500 µm view field) (a) Aluminum alloy 5754 (b) Aluminum alloy 6111.

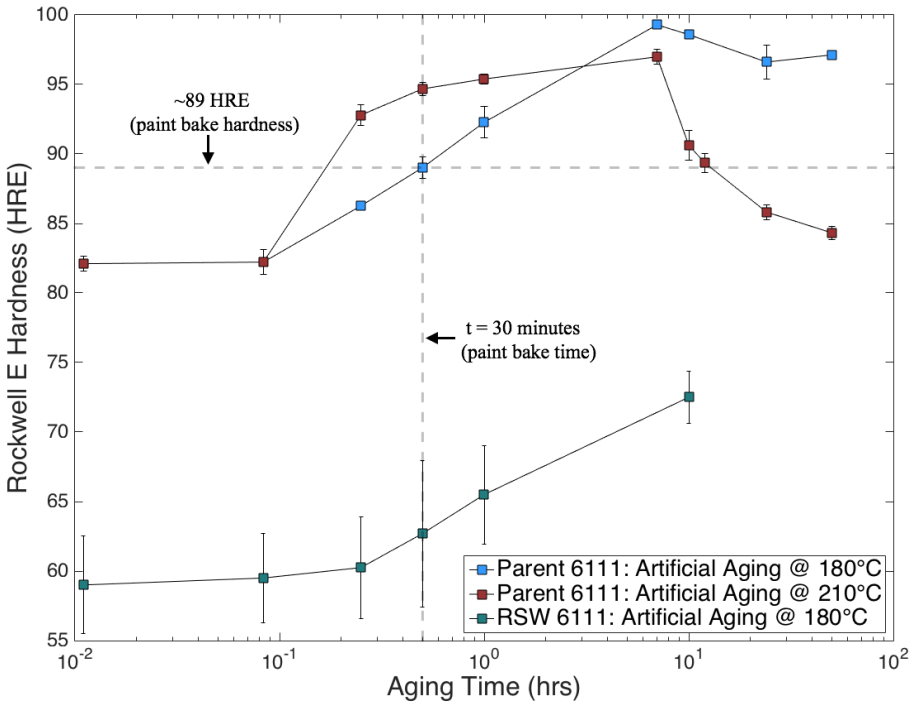

Figure 4.2 – Rockwell hardness vs. artificial aging times for T4 and 6111 Al spot welds. The PB heat treatment is marked, and the OA heat treatment was selected to match the hardness and yield strength of the PB condition.

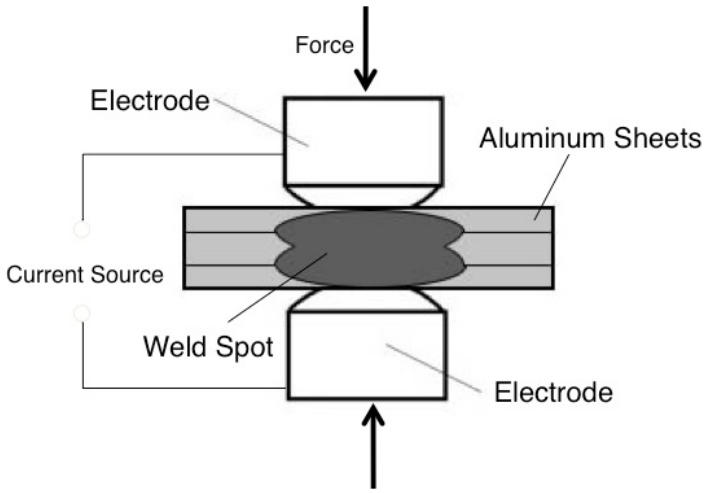

Figure 4.3 - Schematic of the resistance spot welding process for sheet metal. The image displays a 2-3-2 stackup used in this study.

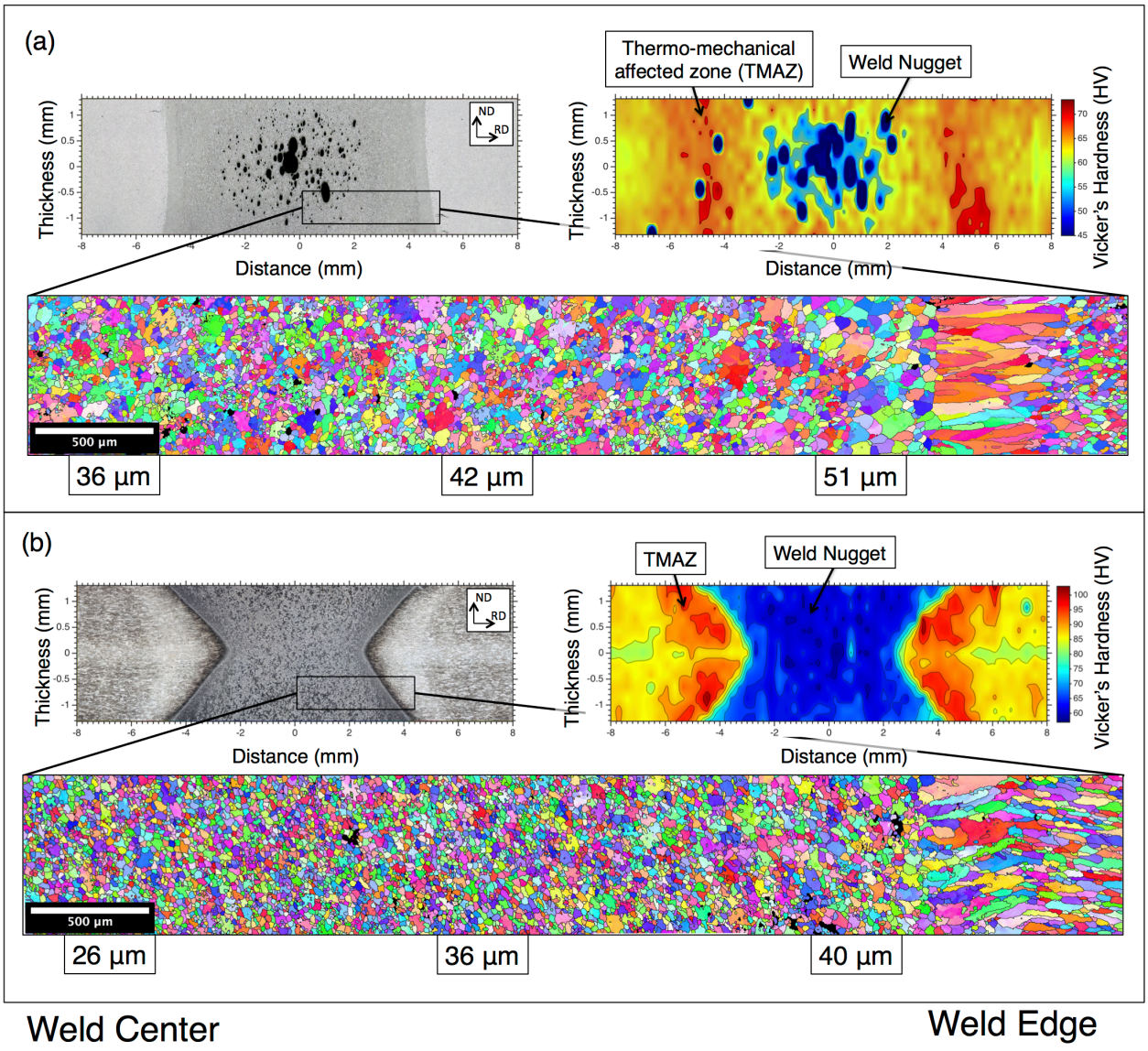

Figure 4.4 - Optical images, associated microhardness maps and EBSD of the weld microstructure from the weld centerline to the parent material in the ND-RD plane. (A) RSW Al 5754 (b) RSW Al 6111. The numbers underneath the EBSD map correspond to the average grain sizes at these regions.

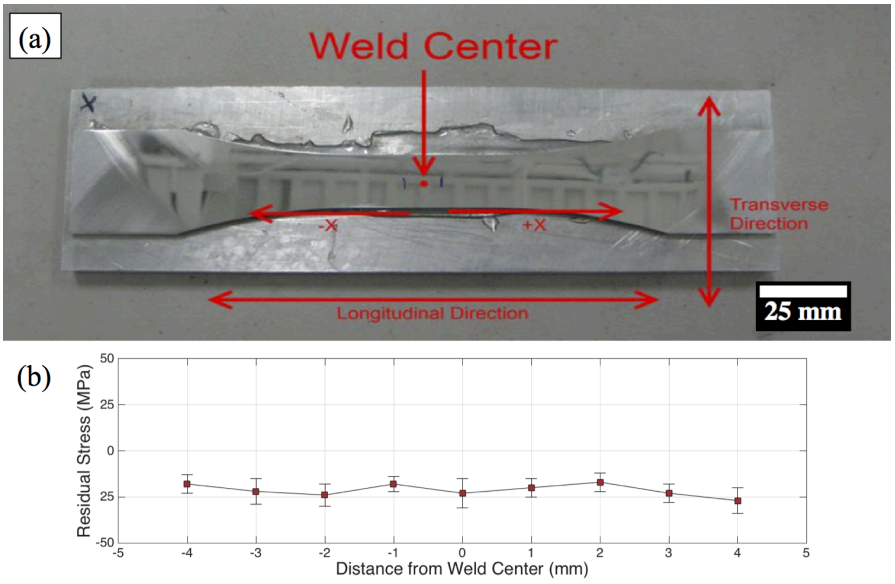

Figure 4.5 - Residual stress measurement of RSW specimen (a) Dogbone specimen used for XRD analysis with the regions marked (b) values obtained from the weld centerline ± 4mm.

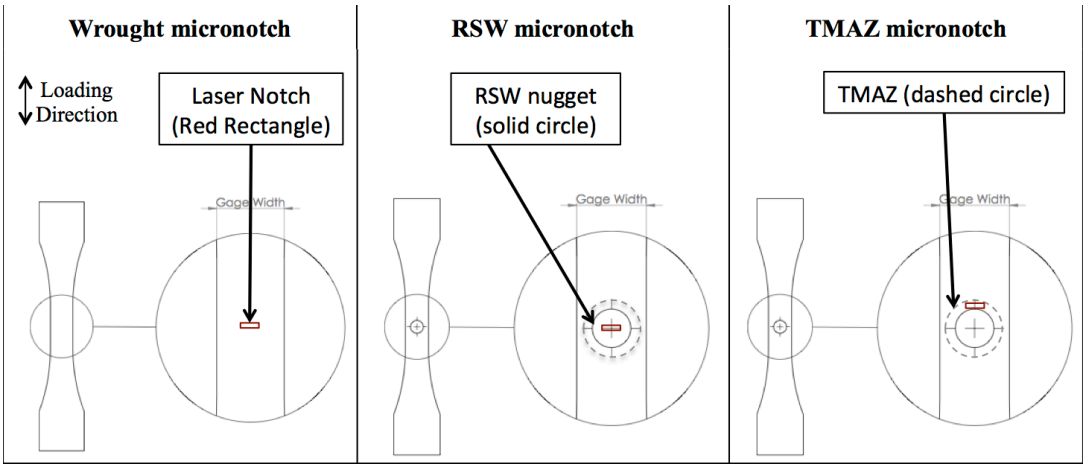

Figure 4.6 - Schematic detailing the location of the femtosecond micronotch on the dogbone specimen.

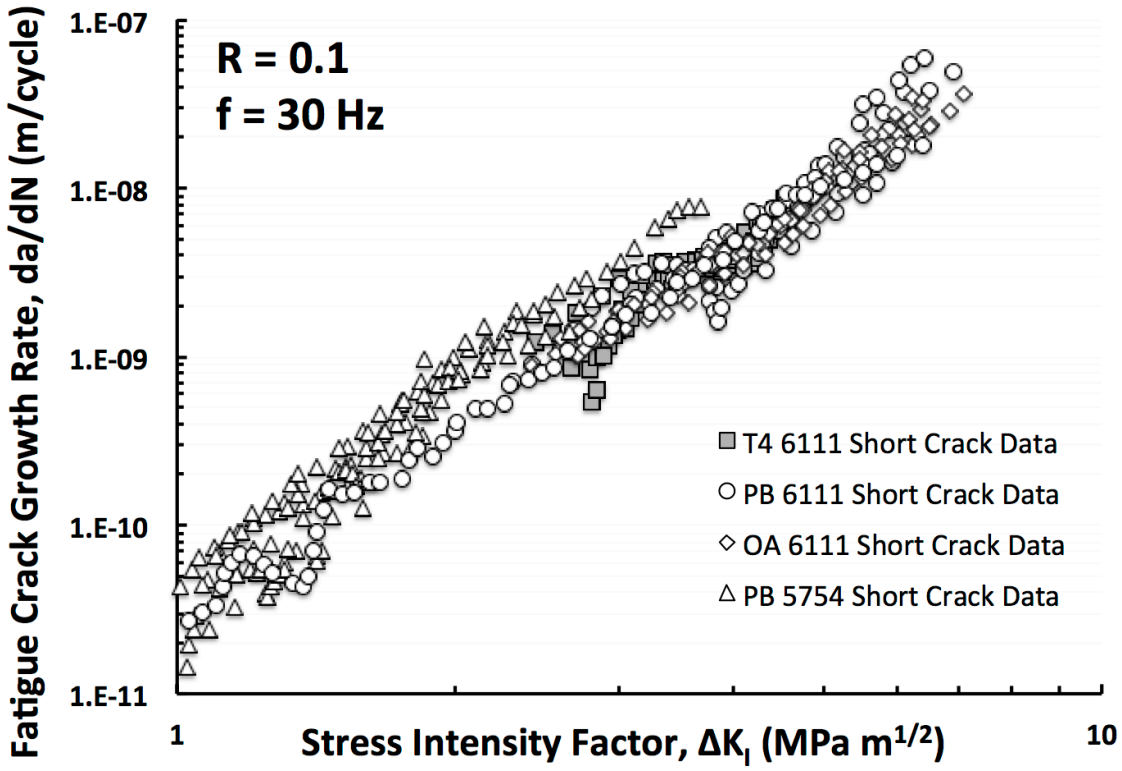

Figure 4.7 – Measured fatigue crack growth rates, da/dN vs. ΔK for wrought aluminum 5754 and 6111.

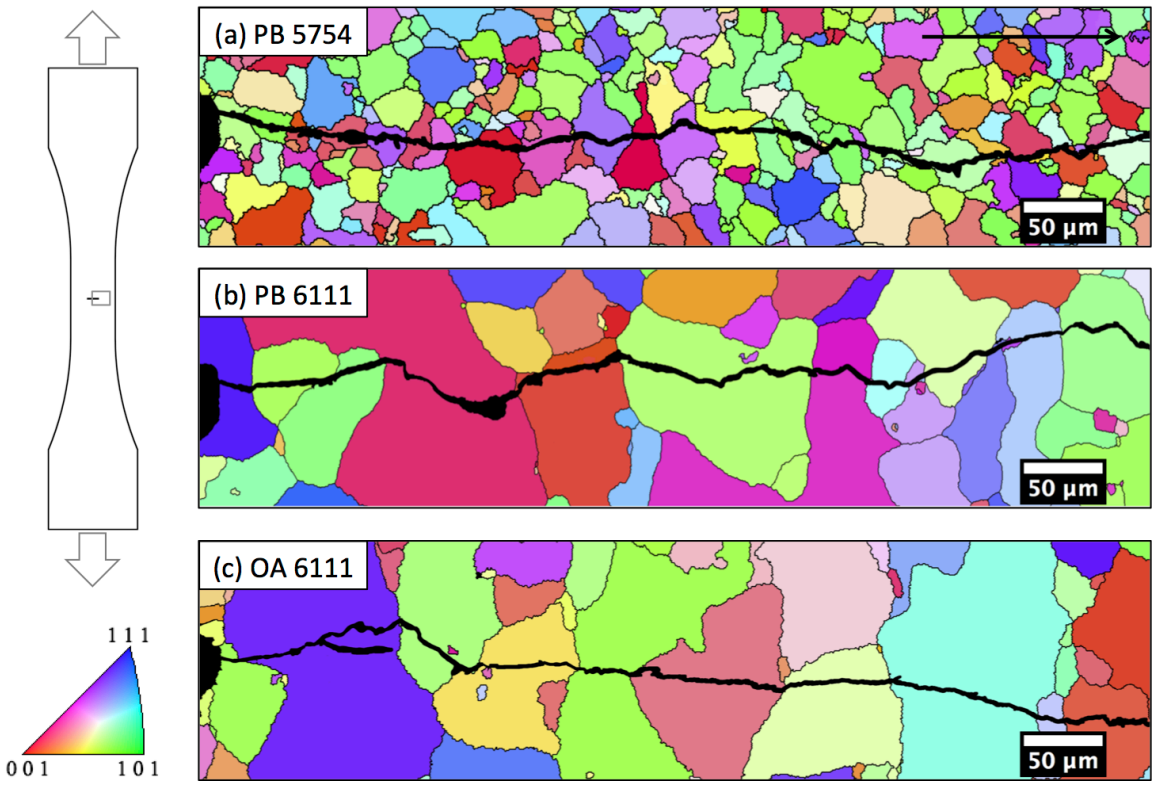

Figure 4.8 – EBSD surface crack profiles showing crystallographic propagation and deflection of short cracks at grain boundaries in (a) PB 5754 (b) PB 6111 and (c) OA 6111 conditions. The crack propagation direction is from left to right.

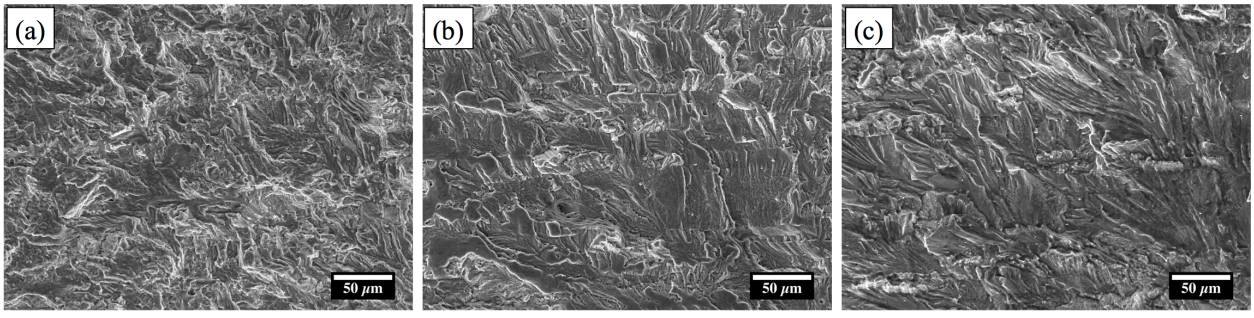

Figure 4.9 - Fatigue fracture surfaces adjacent to the micronotch for (a) PB 5754 (b) PB 6111 and (c) OA 6111 conditions. The crack propagation direction is from bottom to top.

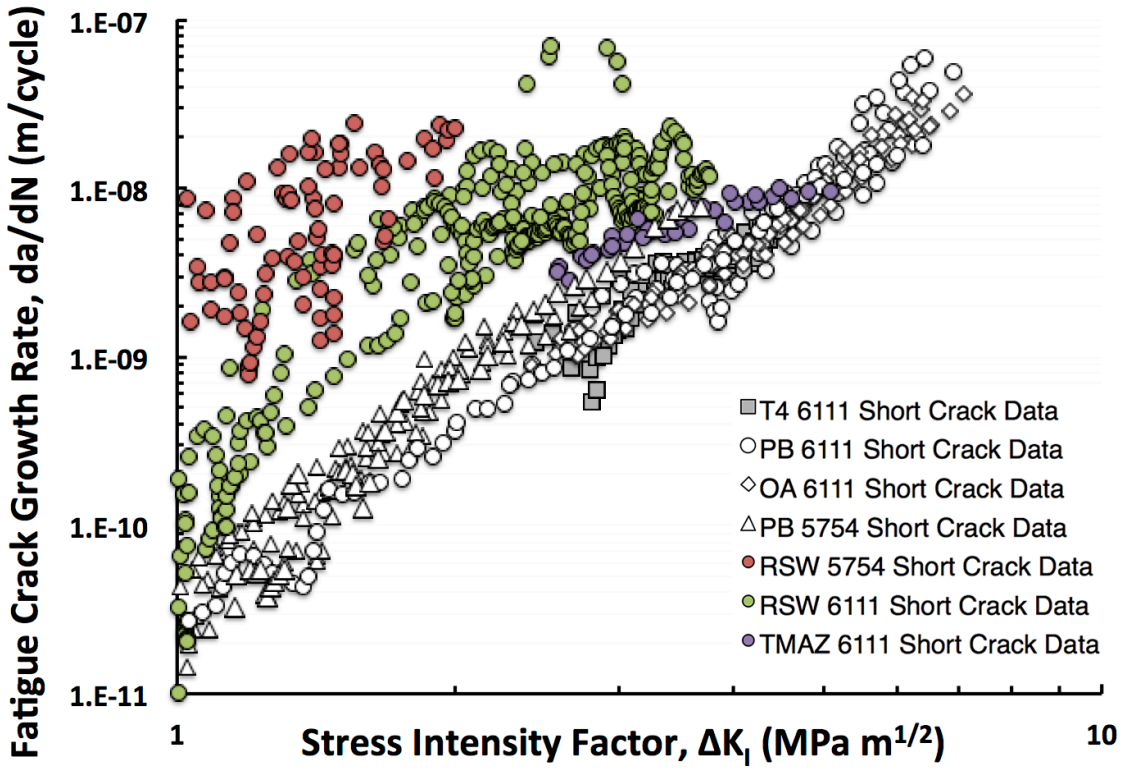

Figure 4.10 - Short-crack growth rates vs. ΔK for resistance spot welded regions compared to growth in the parent material (in white and gray).

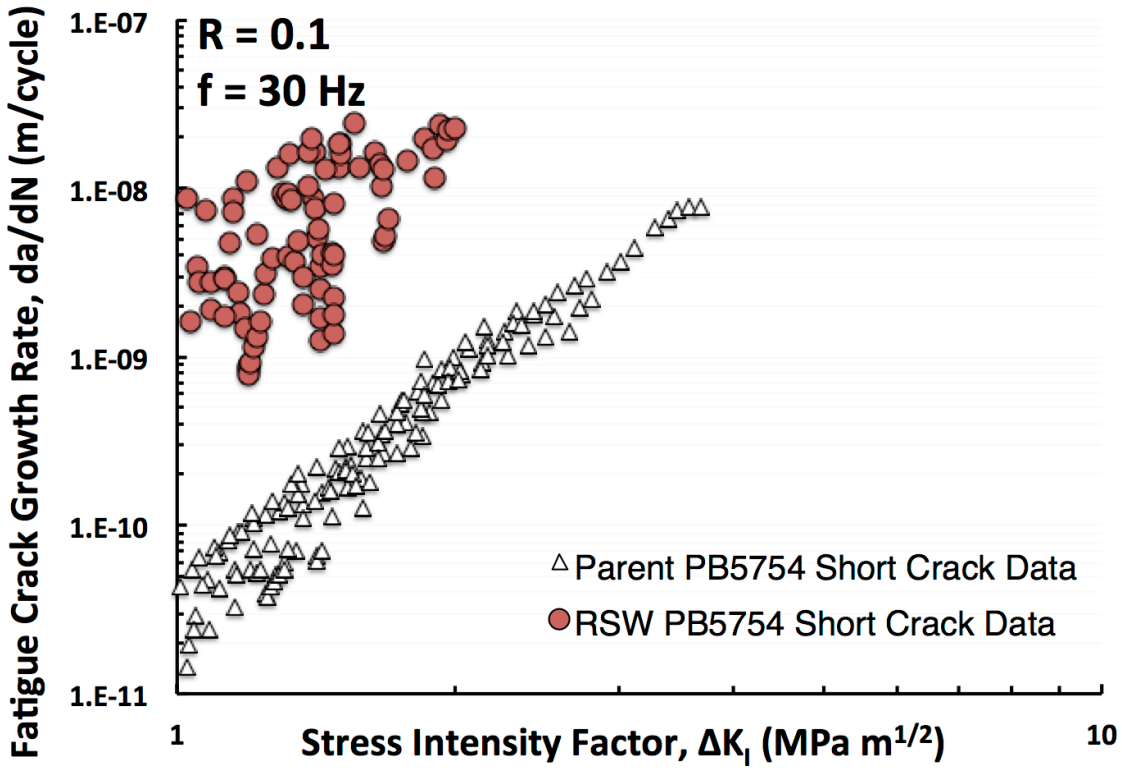

Figure 4.11 - SFCG rates for the RSW and parent PB5754 alloy. For a given ΔK, short cracks propagating in the spot weld can grow up to two orders of magnitude faster than the parent sheet.

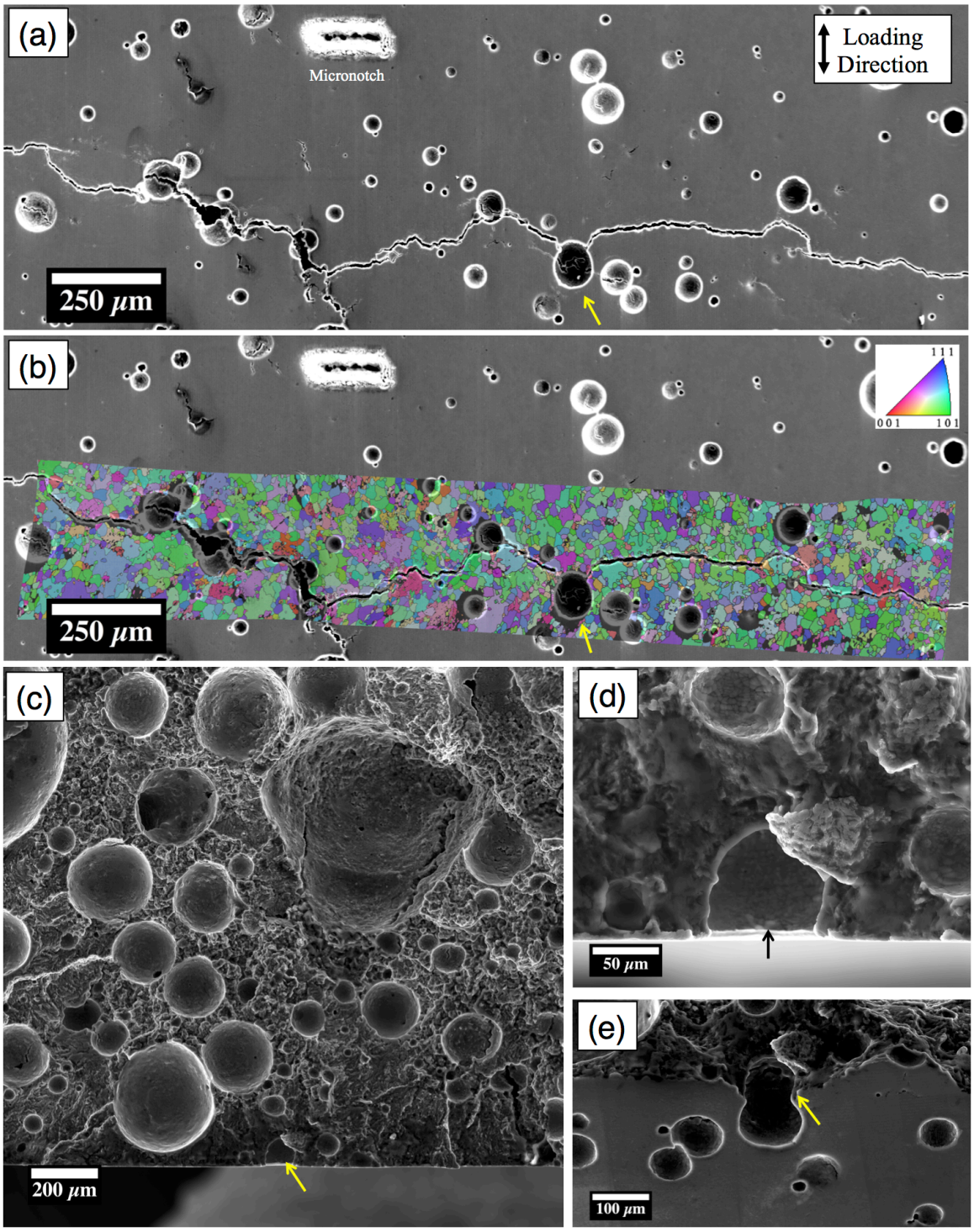

Figure 4.12 – 5754 RSW S1 (σ_{max} = 45 MPa). The arrow designates the initiating pore. (a) SEM surface image and (b) the EBSD map of the crack propagation path overlaid. The fracture surface showing (c) macroscopic fracture surface, (d) zooming in on the surface initiating pore; (e) displays the same feature at a 45° tilt.

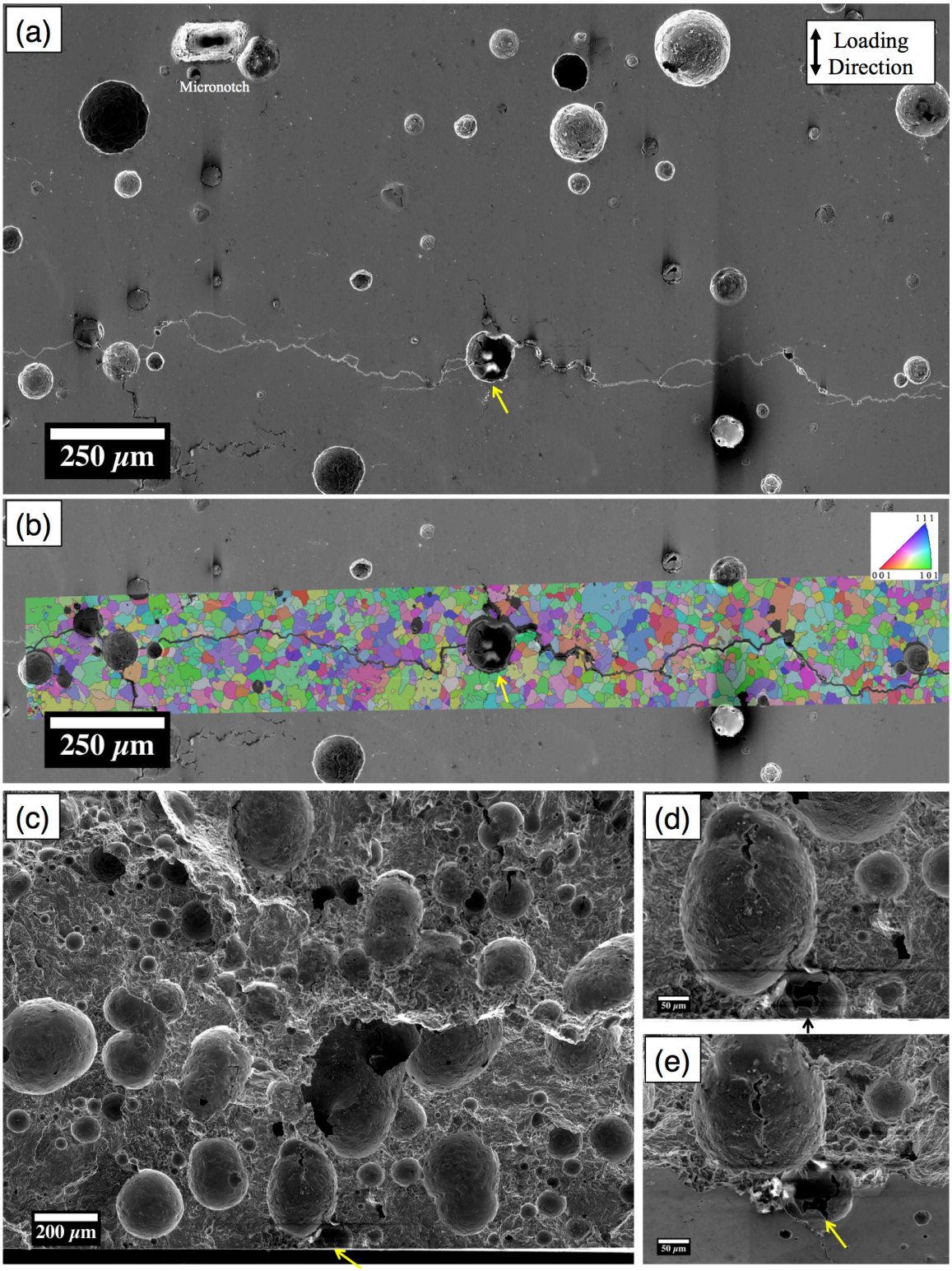

Figure 4.13 – 5754 RSW S6 (σ_{max} = 50 MPa). The arrow designates the initiating pore. (a) SEM surface image and (b) the EBSD map of the crack propagation path overlaid. The fracture surface

showing (c) macroscopic fracture surface, (d) zooming in on the surface initiating pore; (e) displays the same feature at a 45° tilt.

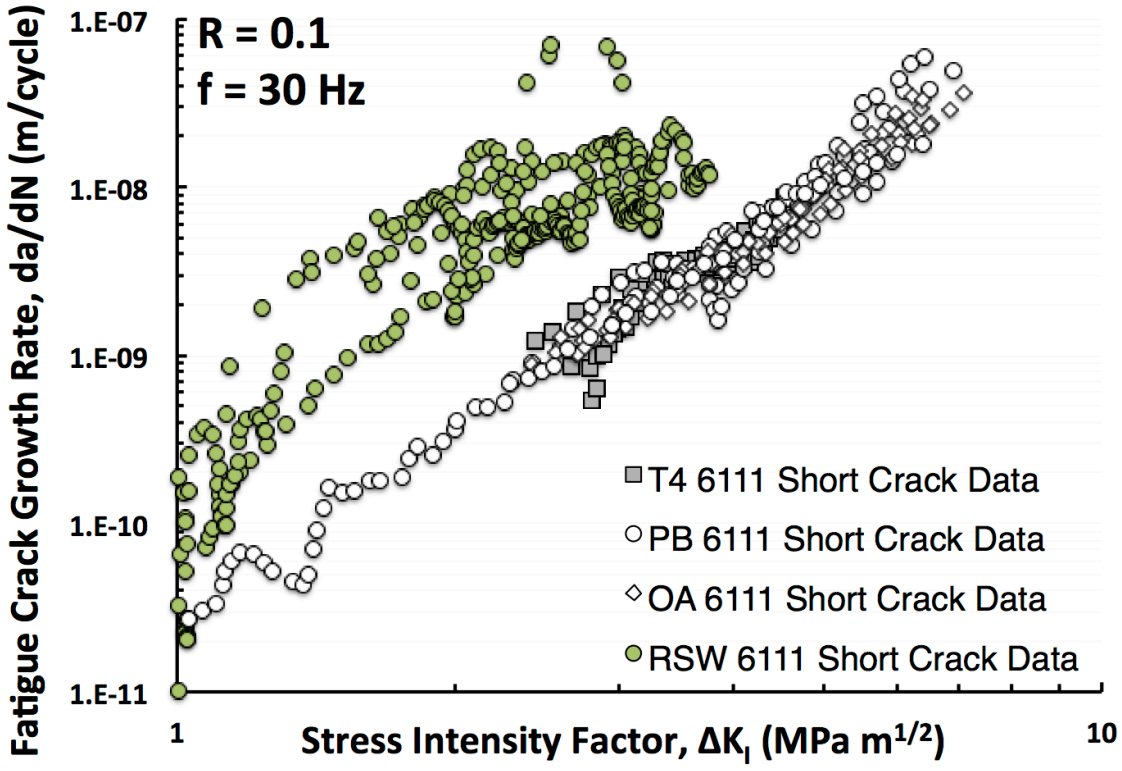

Figure 4.14 - SFCG rates for the RSW and parent 6111 alloy. For the region of ΔK where the parent material was tested, cracks are propagating approximately one order of magnitude faster in the resistance spot welds.

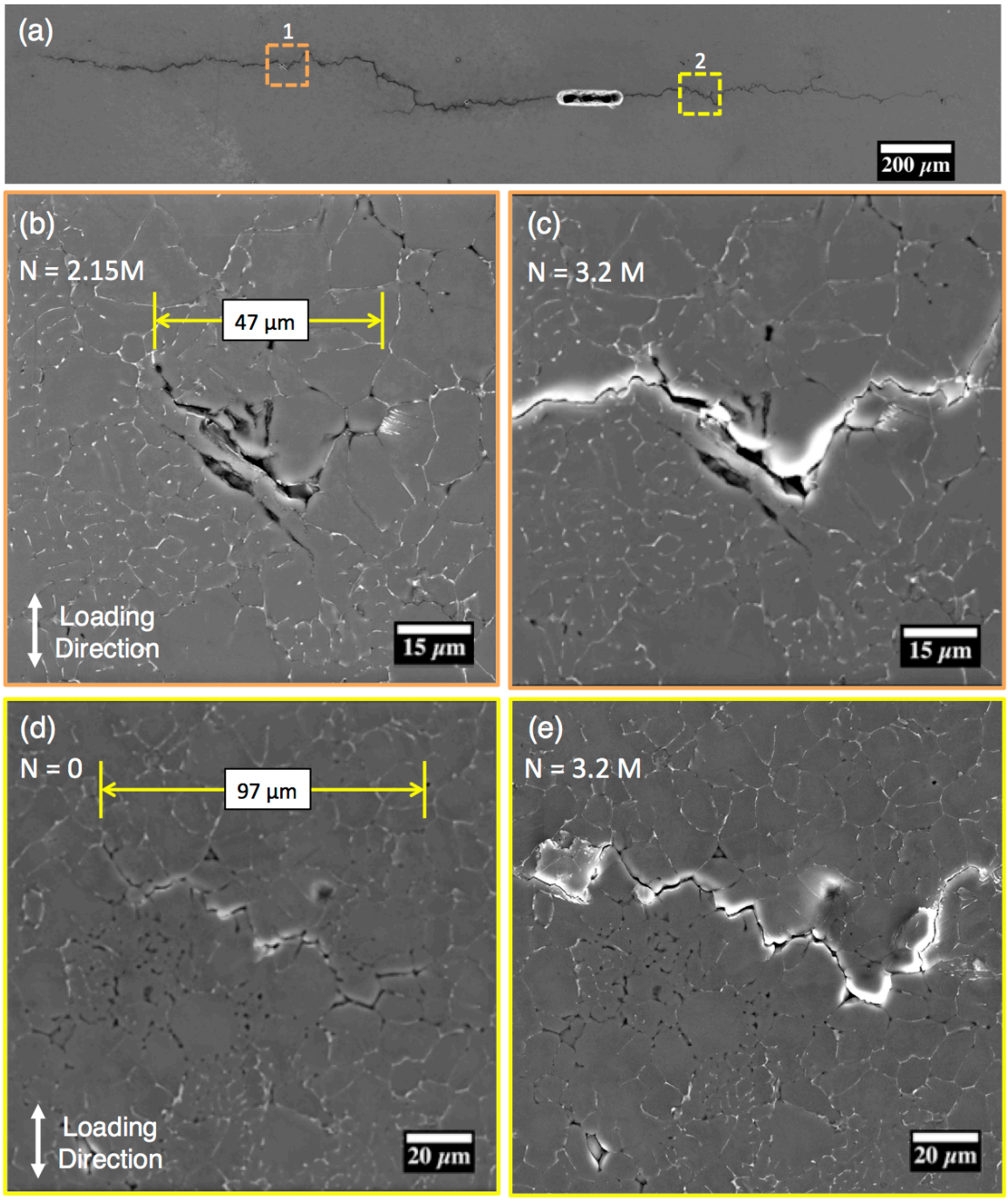

Figure 4.15 – SEM image of crack growth from a micronotch in 6111 RSW S15. (a) Displays an overview of the surface crack and the two pores of interest, Pore 1 and Pore 2. The earliest (2.15M cycles) and final (3.2M cycles) instances of Pore 1 are shown in (b) and (c); the earliest (0 cycles) and final (3.2M cycles) instances of Pore 2 are shown in (d) and (e).

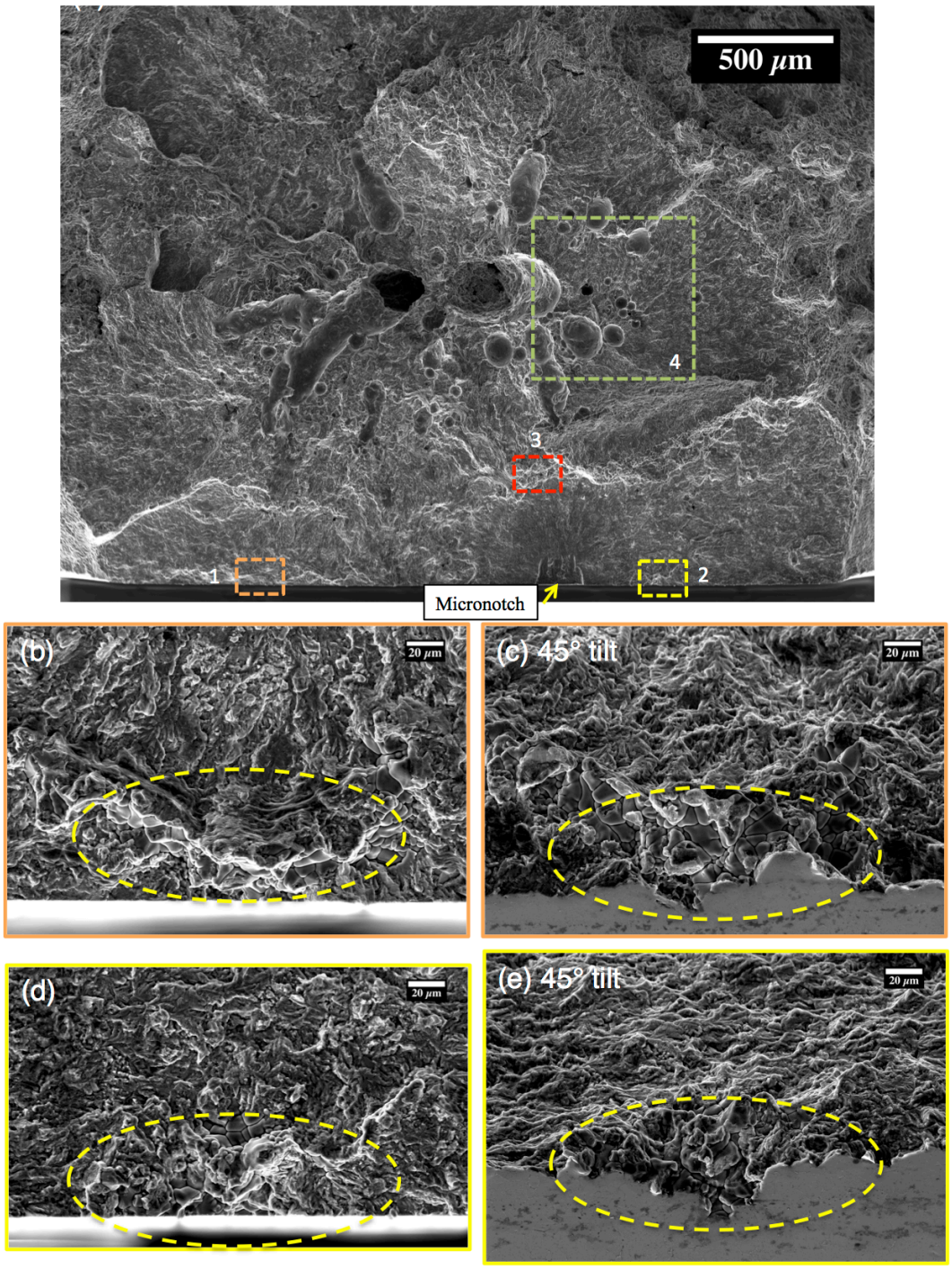

Figure 4.16 – Fracture surface of 6111 RSW S15. The same pores, Pore 1 and Pore 2 are marked as shown in Figure 4.15. Fatigue crack growth testing finished at 3.2M cycles. Figure (a) shows the macroscopic fracture surface, noting the micronotch and the pores investigated. Pore 1 (b,c) and Pore 2 (d,e) are presented in these micrographs. The images on the left area shown perpendicular to the loading direction, while the right images are the same images rotated 45°. Pore regions 3 and 4 are focused in the subsequent image.

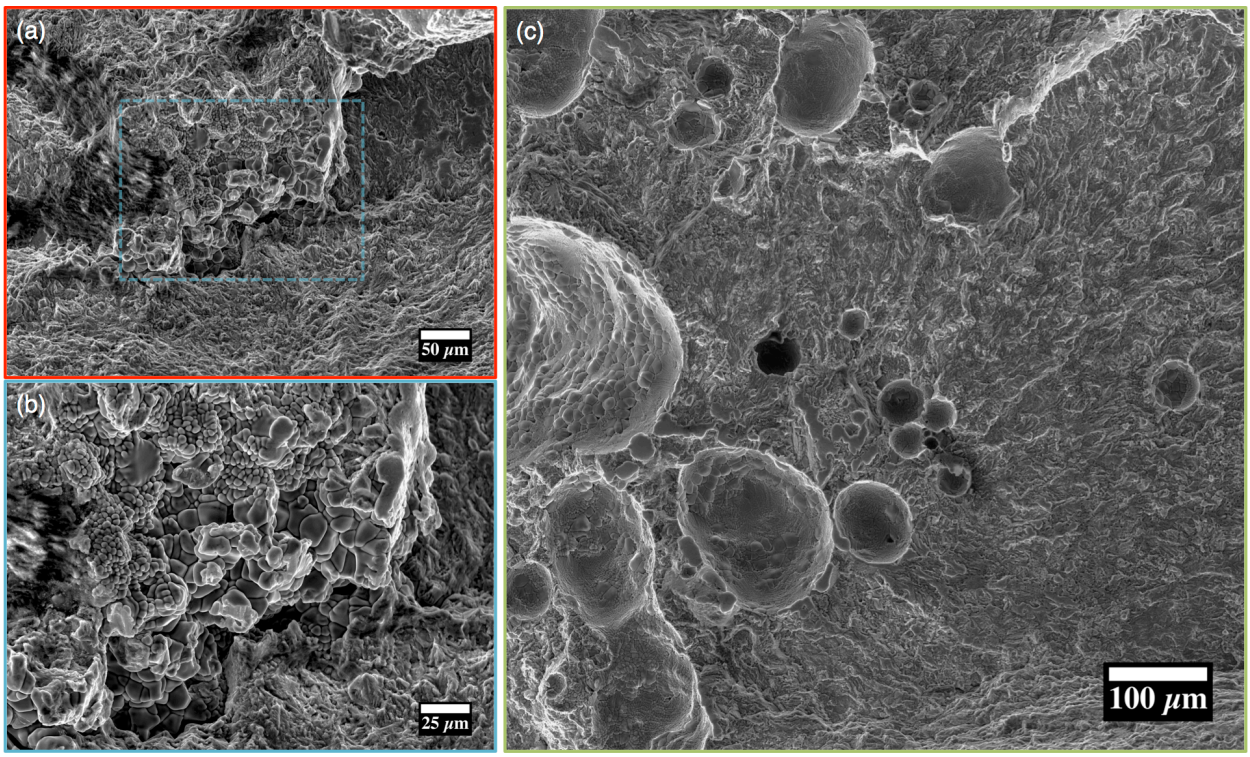

Figure 4.17 – Pore regions marked 3 (a,b) and 4 (c) from Figure 4.16. Region 3 (a, b) examines a region approximately 500 μm from the micronotch. Region 4 (c) displays a micrograph adjacent to the large porosity present in the sheet surface.

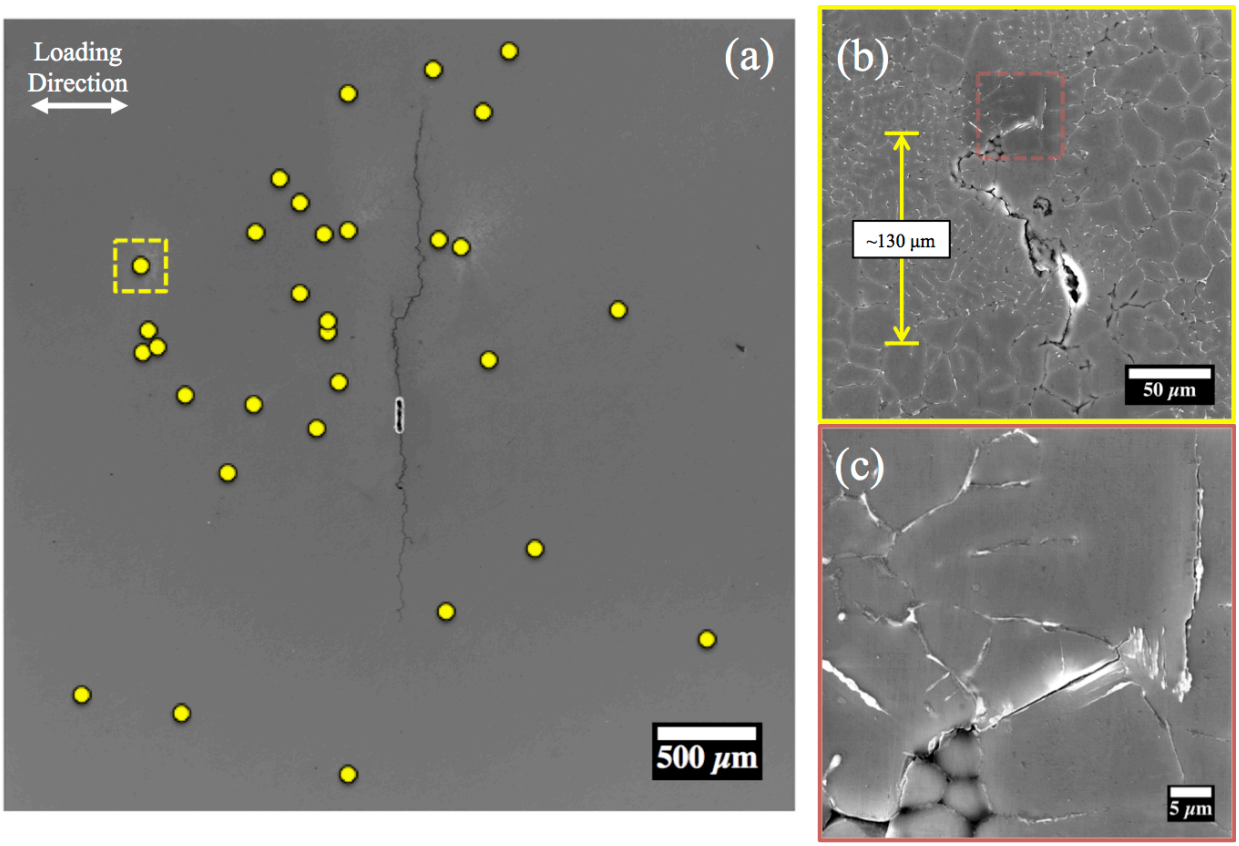

Figure 4.18 - 4x4mm surface SEM image of 6111 RSW S15. (a) Shows the location of welding pores in relation to the micronotch (yellow dots); one example is highlighted in (b) and (c). Growth from this region was limited to two grains.

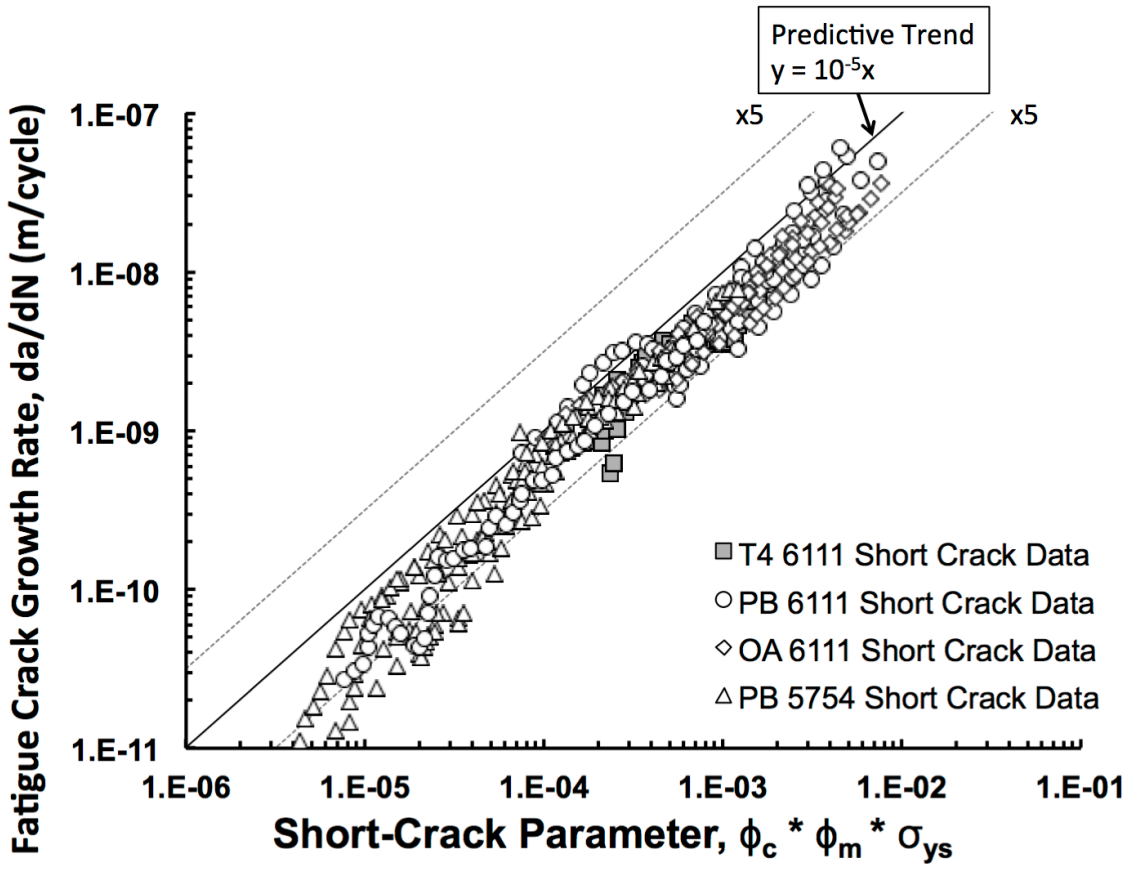

Figure 4.19 – Short crack growth rates plotted against the unified parameter for the parent 5754 and 6111 aluminum alloy sheet.

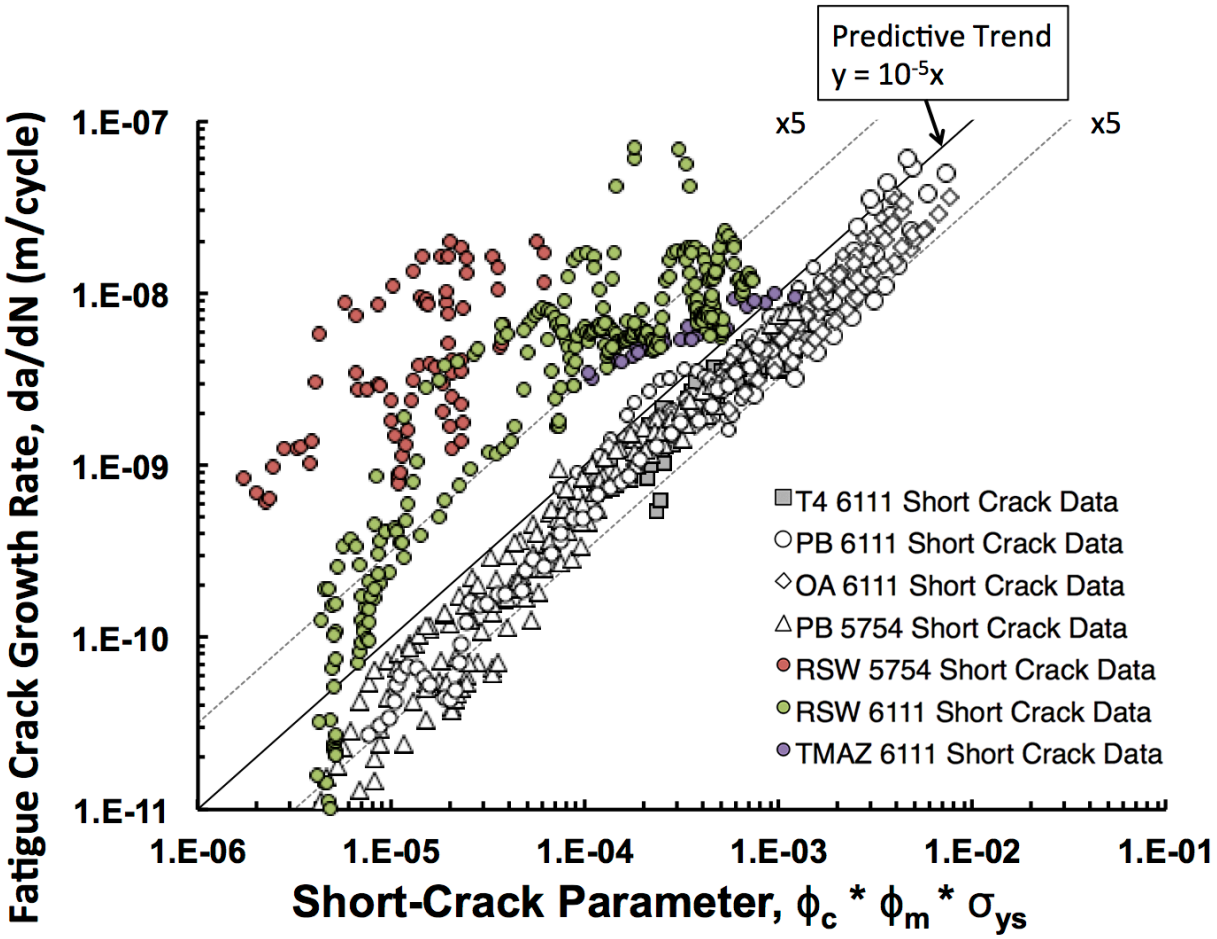

Figure 4.20 - Short crack data of the RSW and parent 5754 and 6111 alloys. The growth rate is plotted vs. the unified parameter. Good agreement exists between for the parent material but there is clear deviation for the spot welded conditions.

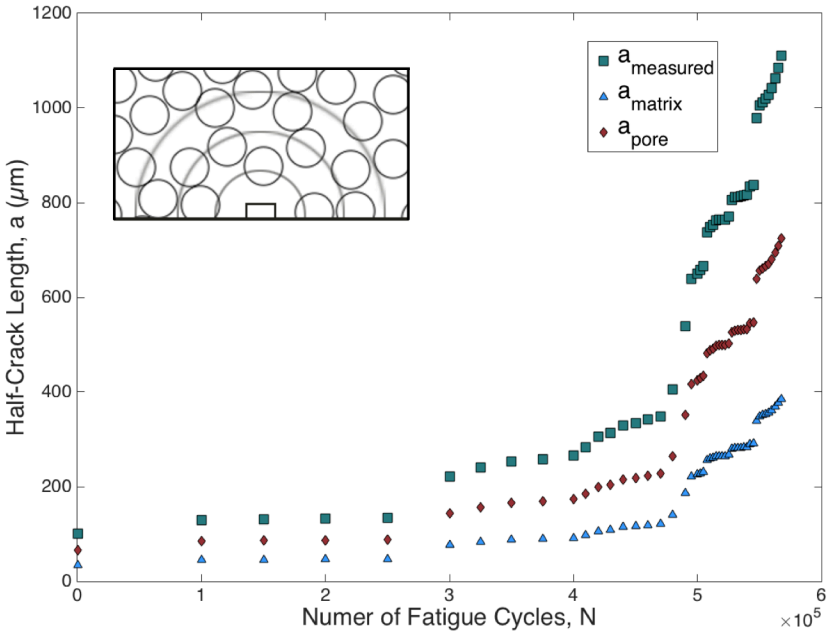

Figure 4.21 – Schematic showing contributions to crack growth from the matrix, from pores and total crack length vs. number of cycles to failure.

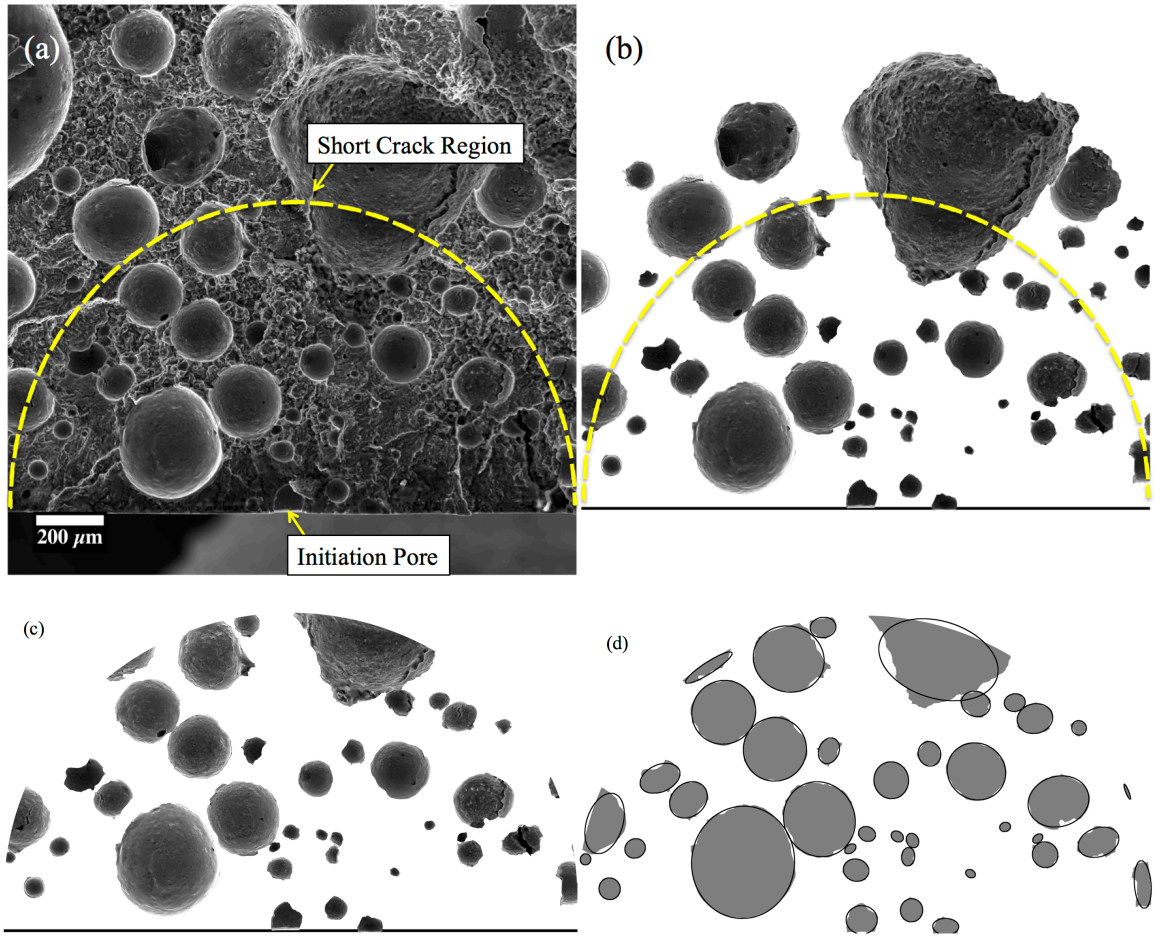

Figure 4.22 - Determination of the fraction of porosity present in the short crack regime from the fracture surface of 5754 RSW S1.

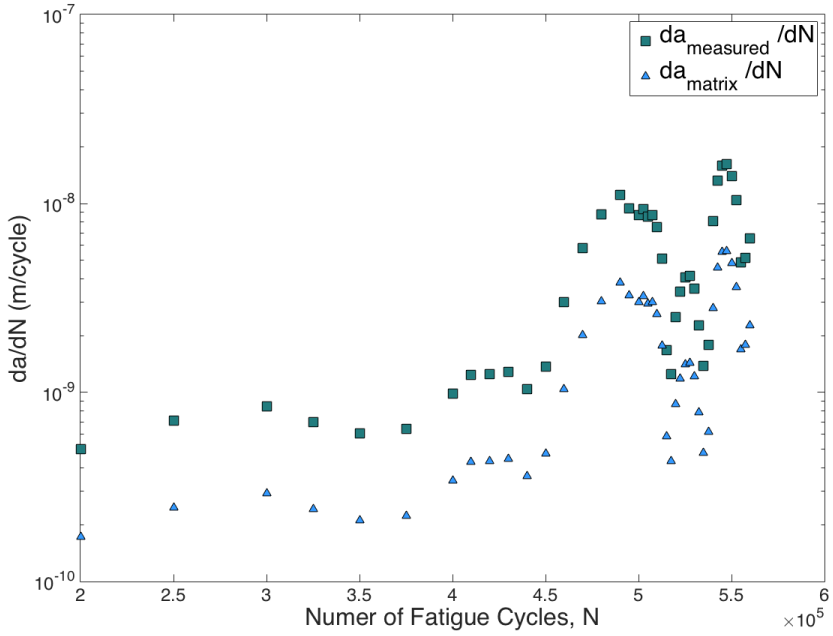

Figure 4.23 - SFCG rate from the measured and calculated matrix contribution for 5754 RSW S1. The matrix component has been adjusted by a factor of $(1-f^{1/2})$.

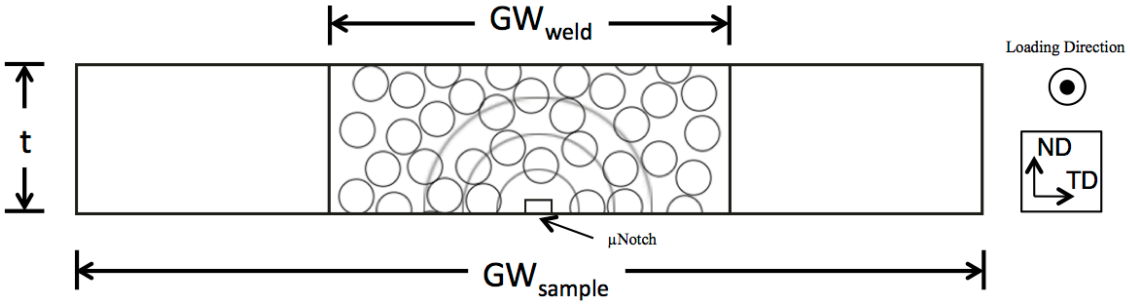

Figure 4.24 - Schematic of cross section through nominal crack plane indicating the porous weld and non-porous wrought regions. The micronotch and progressive crack front are noted.

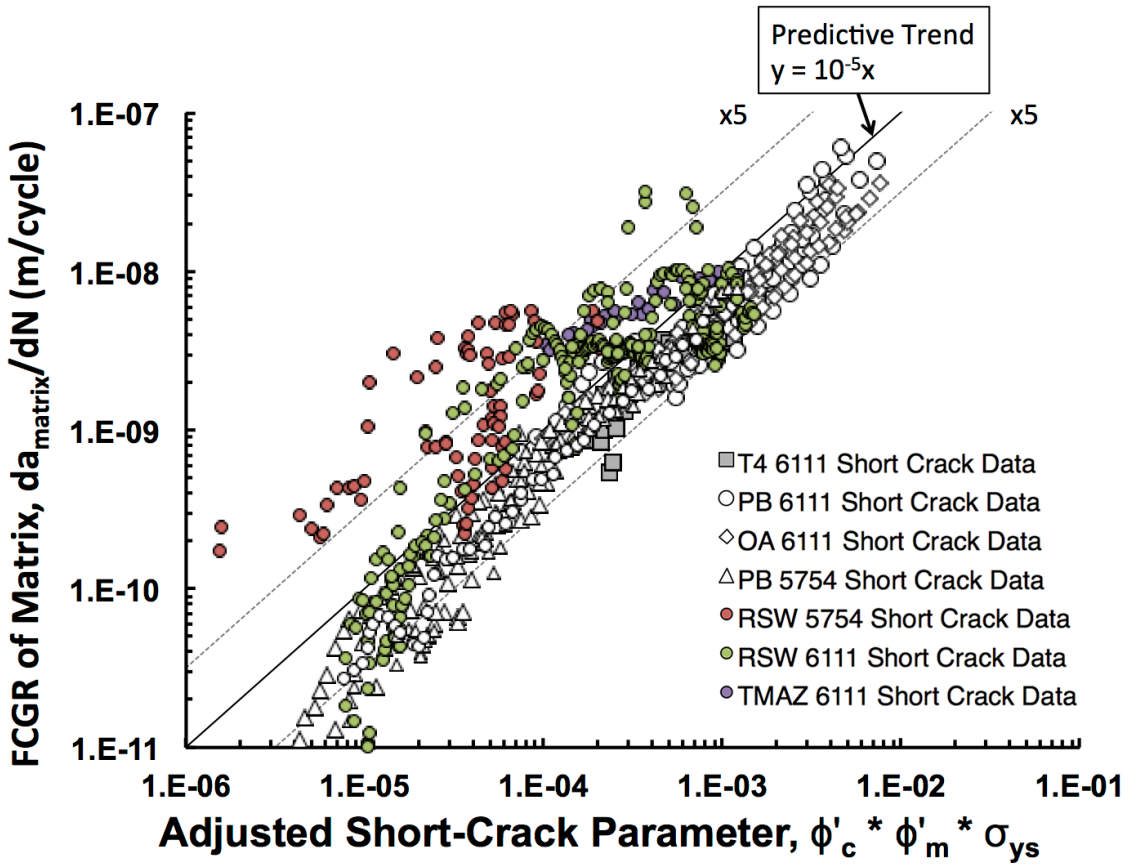

Figure 4.25 – Crack propagation through the matrix plotted vs. the adjusted unified parameter. Better agreement between the spot welded alloys, parent conditions and the predictive trend line from Shyam et al. [48] are apparent.

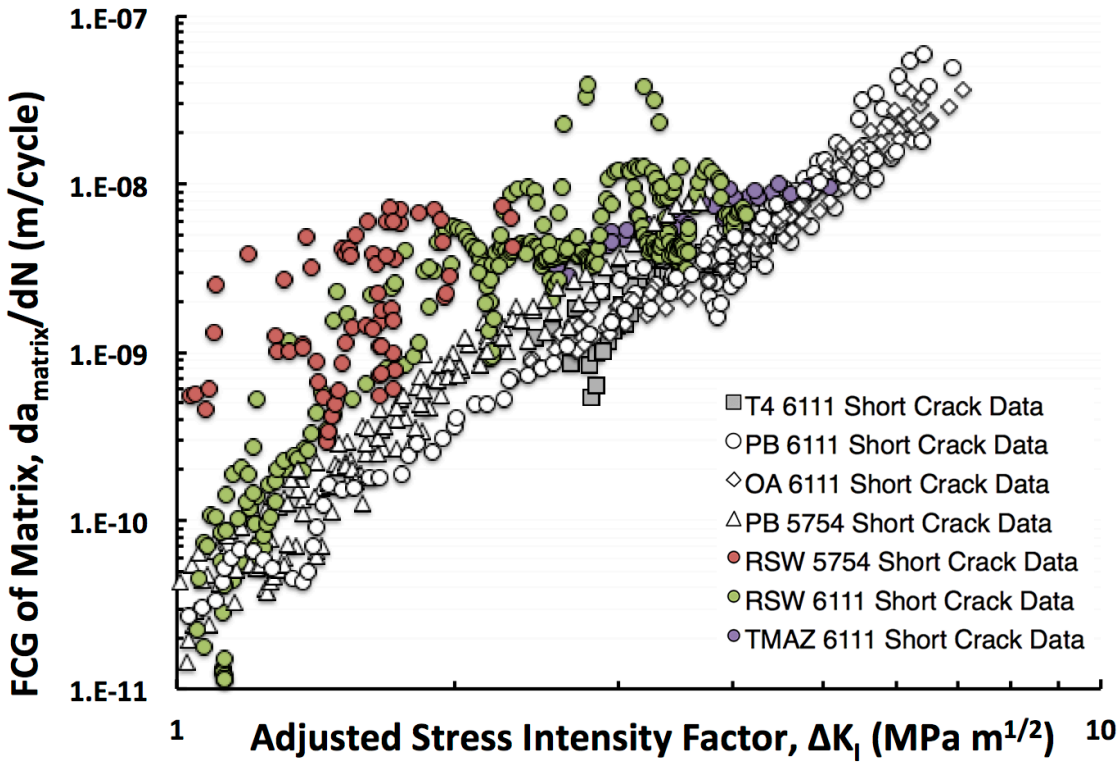

Figure 4.26 – Short crack growth rate through the matrix vs. adjusted ΔK. Better agreement is also observed but not as clear as with the unified short crack parameter.

Chapter 5

Development Of A Structural Stress Master Fatigue Life Relationship For Modeling Durability Of Resistance Spot Welded Joints In Aluminum Alloys

This chapter covers the construction, calibration and validation of a structural stress based master fatigue life relationship for modeling eyebrow cracking in spot welded aluminum lap-shear specimens with finite element analysis and short fatigue crack growth data. Section 5.1 covers the competing modes of failure for lap-shear specimens and the structural stress approach being undertaken in this research. Section 5.2 discusses the finite element model used to determine the structural stress and ultimately the fatigue life. Section 5.3 discusses the experimental fatigue life tests used to calibrate the model. Section 5.4 details the equivalent initial flaw size method used to estimate an appropriate starting point for integrating fatigue crack propagation life. Finally, Sections 5.5 and 5.6 discuss the results from the fatigue life tests and finite model to create the master fatigue life curve.

5.1 Introduction

Resistance spot welding (RSW) is a widely employed joining technique in the automotive industry for joining multiple pieces of sheet metal components. The RSW process consists of joining the sheet metal together with (a) pressure from two copper electrodes on opposite ends of the sheet stack-up, (b) application of a current through the electrodes, the resistance to which

generates heat at the center of the sheet metals (c) melting of the sheet material from the resistance heat and (d) re-solidification of the melt pool once the current is stopped, forming a weld nugget [1].

Most vehicles in North America typically contain between 4-5,000 spot welds. The strength of spot welds determines the integrity of structural performance for the application of use. Over the years, RSW fixtures have been successfully used for various steel grades to deliver high-quality joints [2,3]. Steel spot welds are higher strength than their parent material counterpart, while this is not observed for aluminum alloys. In 5000 series aluminum spot welds the strength in the fusion zone is comparable to the parent material strength [4]. In 6000 series aluminum, the fusion zone is softer than the parent material. This loss in strength is usually attributed to the dissolution of strengthening precipitates [5].

In service, spot welded joints experience both tensile and bending stresses, and this stress state coupled with joint geometries leads to stress concentrations and eventual fatigue cracking at the perimeter of the spot weld. Three competing modes of fatigue failure have been observed: interfacial failure (fracture via crack propagation through the weld nugget), nugget pullout (the weld nugget is completely pulled out from one of the metal sheets), [6,7] and eyebrow cracking. The dominant mode is dependent on the applied stress level and cyclic life. At moderate stress levels and lives of at least 10^4 cycles, the most commonly observed failure mode is eyebrow cracking. This type of failure is defined by crack initiation at the edge of the spot weld and propagation through the sheet thickness [8]. This failure mode occurs primarily due to the stress concentration provided by the "notch" that occurs due to sheet separation from indentation at the faying surface (contact surfaces between the joint), shown in Figure 5.1.

Prediction of joint durability for any welded structure can be a challenging task due to the complicated stress state [9–12] that exists throughout the volume of the weld and the complex microstructure that forms in and around the spot weld. This is especially true for aluminum alloy sheet structures, which, until recently (such as in the Ford F-150 [13]), have not been widely used in mass production vehicles. The structural stress method, a common approach for dealing with durability prediction of joints [14], has not been fully explored for use with spot welded aluminum structures. The structural stress method aims to simplify the stress state at the crack initiation location as a function of the loading mode and geometry in a linear elastic analysis [14]. The simplification of the stress state is done through the process of stress linearization. This process delineates the through thickness stress distribution (see Figure 5.2) from a finite element model into a membrane ($\Delta\sigma_{mem}$) and bending component ($\Delta\sigma_{bend}$) that are the equilibrium equivalent to the local stress distributions [12]. The aggregate of these two stress components compose the structural stress ($\Delta\sigma_{ss}$).

A multitude of approaches to structural stress modeling have been developed. Sheppard [9,15] was one of the first to propose this approach, utilizing linear elastic element models to simulate the forces around the weld nugget. Rupp [10] modeled the spot welded joint as a rigid inclusion determined local structural stresses using cross-sectional forces and moments from beam, sheet and plate theory. Lin and Pan [16–18] analytically determined the structural stresses using elasticity and fracture mechanics theory.

The model used in this research is the so-called Battelle method proposed by Dong [12,19], in which the structural stress is calculated from the nodal forces and moments derived from linear elastic finite element analysis that satisfy equilibrium conditions. More details of this

approach can be found in Section 5.2.2. The critical mode for fatigue crack propagation at the critical node with this approach is Mode I loading.

The aim of this research is to create a new, fatigue crack growth / fracture mechanics based approach for developing a master fatigue life curve or relationship for the eyebrow cracking failure mode, for use with a structural stress method of life prediction for joints. We demonstrate this approach for predicting join durability in spot-welds joining the aluminum alloys 5754 (Al-3Mg) and 6111 (Al-1Mg-1Si). These alloys are used for inner and outer body panels, respectively.

Validation and calibration of the master fatigue life relationship consisted of fatigue life testing of lap-shear specimens (Figure 5.3) of both alloys. Joints with four geometric parameters (sheet thickness and nugget diameter), two load level and two mean stresses were tested to calibrate and validate this approach. Standard engineering practice [20] dictates the weld nugget diameters to be at least 4 times the square root of the sheet thickness ($4t^{1/2}$). For this research, the nominal weld nugget diameters (d_{wn}) tested were set to between $4t^{1/2}$ or $5t^{1/2}$.

5.2 Finite Element and Structural Stress Model for Fatigue Life Calculation

5.2.1 Finite Element Model

Often the data needed to determine the fatigue lifetime of spot welded joints is unavailable. This is especially the case for new applications of spot welded aluminum structures where there is limited information for new alloys and structures. In order to reduce the time necessary to generate such data, finite element (FE) models have been utilized to accurately

model the durability based on the service loads to which these joints would be subjected. In the current investigation, FE modeling was performed using the commercial FE software, Abaqus®. Traditional evaluation of spot welded joints has been performed with detailed 3-dimensional finite element model that necessitates large computation time and complications due to changing geometric parameters [18,21–23]. For full-scale vehicle modeling, a more computationally efficient and robust FE methodology is utilization of a shell model. Shell elements can be used instead of solid elements when the dimensions of the two-dimensional plane being modeled are at least 20 times greater than the third direction [24], which in the context of this research is true for 1 and 3mm thick welds. This reduces the computational time required by reducing the number of finite elements (and thus the number of equations that must be solved).

Lap-shear specimens were designed using S4R elements (reduced integration four-node shell element). A representative FE mesh is shown in Figure 5.4. Previous research [10,18] has shown that eyebrow cracking occurs approximately at the edge of the spot weld nugget and orthogonal to the loading axes, and thus this region needs to be accurately modeled. However, utilizing finite elements to represent this region may result in a dependency of the stress state on the mesh size. To circumvent this issue, a "spider method" [25,26] was used to represent the weld nugget, as shown in Figure 5.5. With this method, a rigid area equal to the size of the spot weld is created with S4R elements in a spoke pattern at the center interface between the two sheets. For this research, 24 nodes are used along the spot-weld circumference. The rigid areas are then connected from the weld nugget perimeter nodes to a central node for each sheet via a multi-point constraint (MPC) beam element, points O and O'. The central nodes for each spider weld nugget are then connected via another MPC beam element. These constrain the displacement and rotation of the first node to the displacement and rotation of the second node

[26]. The boundary conditions for this model include the MPC's associated with the spot-weld, a fixed end where all 6 degrees of freedom are constrained, and the end where the external load is applied which is fixed in all directions, except in the X-direction where the load is being applied to represent the uniaxial stress condition.

5.2.2 Structural Stress Model

The structural stress methodology, as discussed in section 5.1, is primarily used to simplify the stress state at the weld nugget periphery into a membrane and bending stress component. Values from the FE model were directly used to calculate the structural stress using a method developed by the Battelle [12,19,27], shown below:

1) Determine the values for the nodal forces and moments within an element that can be attributed to the stresses within that element [28] (also known as the NFORC values) along the weld periphery nodes. These values are in reference to the global coordinate system.
2) Convert the NFORC values from the global coordinate system to a local coordinate system such that the structural stresses are normal to the weld line.
3) Convert the local NFORC values to distributed forces in terms of line forces and moments. This was accomplished using a MATLAB script. The details of this conversion are given in [19].

The individual components for the structural stress calculation (σ_{ss}), the membrane and bending term, are determined from this conversion as shown in Equation [5.1:

[5.1] $$\sigma_{ss} = \sigma_{membane} + \sigma_{bending} = \frac{(f_x')}{t} + \frac{6(m_y')}{t^2}$$

where f'_x is the line force in the direction of the local x-axis and m'_y is the line moment about the local y-axis. Each node at the weld nugget periphery contains a value for the structural stress for a given external load. The objective is to determine the node that has the highest structural stress and consider that node the critical node for calculation of the fatigue life of the joint.

Figure 5.6 displays a representative image of the FE model (a) showing the structural stress around the weld nugget circumference and (b) the values for membrane, bending, and structural stress. The values denote that the highest structural stress node is parallel to the applied load, and illustrates the critical node utilized to determine the fatigue life of the joint. This critical node was found in a consistent location across all thicknesses, weld nugget diameters, and applied loads. It should also be noted that a significant portion (>75%) of the structural stress is comprised of the bending component.

Four different FE models were created to match the thickness (1 and 3mm) and weld nugget diameter variation ($d_{wn} = 4t^{1/2}$ and $5t^{1/2}$) used for model validation. An applied load between 50 and 3050 N was applied to produce a nominal applied stress between 1 and 20 MPa. The area used to convert between applied load and stress was the gage width (25.4 mm) and the combined sheet thickness (i.e. 2 or 6 mm). The values for each geometric condition and applied load are shown in Table 5.1.

A relationship was developed between the nominal stress range and the structural stress range, as shown in Figure 5.7. The correlation from nominal to structural stress at the location of interest is given by structural stress based stress concentration factor, K_g [27]. This is different from the traditional stress concentration factor in that it is meant to quantify the influence of a structural detail, discontinuity or arrangement between components and acts as a conversion factor between nominal and structural when the nominal stress is well defined, as in the case of

the lap-shear geometry. For the geometries modeled, K_g varies from 17.28 in the "thickest" condition and peaks at 25.87 in the "thinnest" condition; that is, K_g increases with decreasing sheet thickness and weld nugget diameter. This indicates that the structural stress decreases with increasing thickness and nugget diameter, which is consistent with the literature [3,29–32]. The implication to this is that for a thinner sample, the structural stress at the critical location is higher compared to a thicker sample, which presumably will result in a shorter predicted fatigue lifetime.

The main reason for the differences in K_g at the critical node for each geometric condition is due to the proportion of the stress state that is comprised of bending. The contribution by bending, defined as the bending ratio R_b, is defined by ratio of bending stress to the overall structural stress and is a function of the geometric conditions and has been found to be constant for any given nominal stress, as shown in Figure 5.8.

[5.2] $$R_b = \frac{\Delta\sigma_{bend}}{\Delta\sigma_{ss}}$$

5.2.3 Fatigue Life Modeling

As noted, the aim of this research is to create a predictive master fatigue life curve or relationship for use with the structural stress approach for eyebrow cracking in spot-welded aluminum components. The structural stress approach simplifies the geometry and loading mode in which the far field and critical region stresses are evaluated [33]. The new concept here is the use of fracture mechanics-based short fatigue crack growth relationship to develop the predictive master curve. Compared to previous approaches (discussed in Chapter 2), the importance of this approach is that it provides a simple, rapid and robust means of develop the master fatigue life

relationship that can be used for new materials and geometries. The fatigue life model operates under the assumption that the crack growth lifetime dominates the fatigue life, as seen in literature [16,23,34], and that the crack growth rate is a function of the Paris' law, such that the crack propagation of an eyebrow crack can be represented by the mode I stress intensity factor solution. This is the most critical mode of through thickness fatigue crack propagation for sheet metal [33].

$$[5.3]\ \frac{da}{dN} = C(\Delta K)^m$$

Stress intensity solutions for an elliptical crack were constructed based upon parametric analysis from Wang and Lambert [35], using elliptical crack solutions for a finite thickness plate similar to Figure 5.9. These solutions were found to be approximately equivalent to the Newman-Raju solutions [36]. ΔK at the depth of the crack (point B) is at its maximum, therefore solutions for that point are considered to be the driving factor for fatigue life calculations. The solutions from Wang and Lambert are presented below:

$$[5.4]\ \Delta K = \Delta\sigma_{ss}\sqrt{t}\sqrt{\frac{\pi\frac{a}{t}}{Q}}\left[Y_o - 2R\frac{a}{t}(Y_o - Y_1)\right]$$

Where t is the plate thickness, a is the crack depth, R is the bending ratio, $\Delta\sigma_{ss}$ is the structural stress range, Y_0 and Y_1 are defined as the geometry correction factor for the semi-elliptical crack faces under stress and is a function of the ratio of crack depth to thickness (a/t) ratio and aspect ratio (a/c) and Q is the elliptical crack front shape factor.

From Equations [5.3 and [5.4, we can integrate to find the number of cycles to failure:

[5.5] $$N_f = \frac{1}{C}\int_{a=a_i}^{a=t} \frac{da}{\left(\Delta\sigma_{ss}\sqrt{t}\sqrt{\frac{\pi\frac{a}{t}}{Q}\left[Y_o - 2R\frac{a}{t}(Y_o - Y_1)\right]}\right)^m}$$

Some questions still remain on how to determine the overall fatigue life from the structural stress based FEA model approach:

1. What is the aspect ratio of the fatigue crack?
2. What proportion of the overall crack grows through the RSW and through the base material?
3. What short crack growth power-law fit exponents should be used?
4. What value should be used for a_i ?

Questions 1-3 are answered through fracture surface analysis of the experimental lap-shear specimens intended for model validation. Question 4 will be examined later in Section 5.4.

5.3 Experimental Fatigue Life Tests

5.3.1 Experimental Approach

To parameterize and validate this model, fatigue tests were conducted using lap-shear specimens for aluminum alloys 5754 and 6111 in the paint baked heat treatment condition (artificial aging at 180°C for 30 minutes). Lap-shear specimens were manufactured by spot welding similar alloy sheets with the same thickness. Lap-shear specimens were provided by Dr. Elizabeth Hetrick at the Ford Research Innovation Center in Dearborn, MI. A schematic of the lap-shear specimen used is provided in Figure 5.3.

The geometry, stress level, and alloy of base material were chosen to investigate the individual effects of these variables on the fatigue lifetime. The thickness of both sheets, t, was between 1 and 3mm, and the weld nugget diameter, d_{wn}, was between $4t^{1/2}$ or $5t^{1/2}$. The samples were cycled at a maximum stress of between 10 and 20 MPa, and load ratio, R, between 0.1 and 0.3 to develop an experimental fatigue life curve. These geometries and stress levels were chosen due to past experimental fatigue life tests performed [4] on aluminum lap-shear specimens that led to eyebrow failure. This test matrix resulted in four geometries per alloy type, each tested at four different stress amplitudes, as shown in Table 5.2. A total of 130 for samples were tested.

Fatigue life testing was performed on an MTS servo hydraulic testing system at a load frequency of 30 Hz for all specimens tested. Fatigue load amplitudes were determined to be constant during this test. Specimens were cycled until failure (completely separated in two parts) or to 10 million cycles, which was considered a run-out.

Post-failure fractographic analysis was performed to determine the final aspect ratio of the crack front for each condition as well as to determine the portion of the overall fatigue life that spanned the weld regime and parent material.

5.3.2 Fatigue Life Results

The fatigue life curves for the lap-shear specimens are presented in Figure 5.10 (a) and (b). The arrows represent fatigue run-out (10 million cycles without failure). All joint fatigue failures were due to eyebrow cracking with the exception that for the two highest stress levels ($\Delta\sigma_{app}$ = 14 and 18 MPa), failure due to eyebrow cracking was not observed for the 1-1mm, $4t^{1/2}$ specimens of either material. Rather, these samples failed via button pullout. An applied load vs. fatigue life curve is presented (Figure 5.10 (a)) as a visual aid and shows the influence of

thickness and alloying on joint lifetimes. It has been observed that the lifetimes of the thinner, 1-1mm, specimens were lower than that of the 3-3mm specimens. This was the expected result based upon findings from the literature and the structural stress results in Section 5.2.2. It was also noticed that alloy 5754 specimens failed earlier than alloy 6111 samples. This result was not anticipated, as literature in both steel [3,37,38] and aluminum [4,39] spot welds suggests that the parent material strength should have no significant effect on the fatigue life.

The nominal applied stress vs. fatigue life is displayed in Figure 5.10 (b). It was observed that the range of lifetimes for a given stress amplitude spanned approximately one order of magnitude. A large number of results are clustered in this plot, and thus, as a visual aid, the lifetimes were averaged per stress level (3-5 specimens) for a given geometric and alloying condition and shown in Figure 5.11. The difference in lifetime for both the thinner and 5754 Al specimens can more clearly be discerned in Figure 5.11. What can also be observed is that the effect of weld nugget diameter appears to be negligible, as the average lifetimes between samples with only dissimilar nugget diameters fall within the standard deviation. The standard deviation for each condition (Table 5.3) at each stress level generally decreases with increasing stress level. This does not apply to the sample sets there were predominantly run-outs.

The applied nominal stress for the experimental lap-shear specimens can be converted to structural stress through the structural stress based stress concentration factor, K_g, as discussed in Section 5.2.2. The calculated structural stress versus fatigue life behavior is presented in Figure 5.12. The structural stress curve (Figure 5.12 (a)) was fit to a power law curve with a coefficient of determination, $R^2 = 0.85$, indicating that the conversion from nominal to structural stress generates a reasonable power law fit. S-N data from literature (axial testing at R = 0) for 5454-O (un-notched plate) [40] and 6061-T6 (un-notched cylinder) [41] was compared to the structural

stress vs. fatigue life data in Figure 5.12 (b). The overlap indicates that the experimental structural stress curve obtained is within the expected range of lifetimes from analysis of similar parent materials. It should also be noted that the lap-shear specimens are considered notched due to the faying interface and thus would be expected to have a steeper slope compared with un-notched conditions.

Traditionally [9,10,14,34], this power law fit represents the "master curve". However, this would only be valid for the joints and alloys tested. The aim of this research is to create a predictive master fatigue life curve that can be implemented for different alloys and geometries with minimal experimentally testing. To accomplish this, a fracture mechanics/short fatigue crack growth approach is proposed, as described below.

It was observed that, for eyebrow cracks, fatigue cracks propagate in a semi-elliptical manner. Optical images were taken to determine the final crack aspect ratio for different thickness samples. Representative fracture images of each thickness are presented in Figure 5.13. For the purposes of this research, the assumption is made that the aspect ratios measured are representative of the aspect ratio of a pure semi-elliptical crack. Thus, the crack aspect ratio used in this study for base material propagation is 0.13 and 0.3 for 1-1mm and 3-3mm sheets, respectively.

Another feature observed from SEM fracture surface analysis is the proportion of the crack life that is spent propagating in the spot weld regime versus the parent material. It was found that, on average, the fracture surface spans approximately 100-300 μm in the 1-1mm samples and 500-1000 μm in the spot welded regime for 3-3mm samples, as shown in Figure 5.14. Based on these values, an assumption is made that the spot welded region encompasses 25% of the overall fracture surface. Features indicative of the spot weld are adherence to the

faying interface, surface inclined at approximately 45° with respect to the loading direction, and a darker appearance compared to the parent material. Once the crack propagates onto the parent material, the fracture plane is approximately orthogonal to the applied stress and displays a brighter appearance.

It was observed from qualitative assessment of the failed samples that no porosity exists on the fracture surface. The frequency of porosity increases towards the center of a spot weld [7] due to the thermal gradients and volumetric expansion of the liquid metal during welding. Thus, the region in which the eyebrow crack propagated is the edge of the weld nugget, where there is growth solely through the fusion zone matrix. Therefore, the adjusted short fatigue crack growth data (growth solely through the weld matrix assuming a pore volume of 0%) from Chapter 4 for the 5754 and 6111 welds will be used to quantify the lifetime of the eyebrow crack as it propagates through these regions.

5.4 Equivalent Initial Flaw Size

The questions posed at the end of Section 5.2.3 for completion of the master fatigue life curve are now revisited: the aspect ratios have been determined to be 0.13 and 0.3 for 1-1mm and 3-3mm sheet stack-ups, respectively; the spot weld spans approximately 25% of the initial propagation while the parent material the propagation until failure. An amended equation (from Equation [5.5) is proposed to account for these effects:

[5.6] $$N_f = \int_{a_i}^{0.25t} \frac{da}{C(\Delta K)^n}\Big|_{Spot\ Weld} + \int_{0.25t}^{t} \frac{da}{C(\Delta K)^n}\Big|_{Parent\ Material}$$

[5.7] $$N_f = f\left(t, \frac{a}{c}, \Delta\sigma_{ss}, R, a_i, [C, n]_{Spot\ Weld/Parent}\right)$$

It is assumed, for the initial fatigue crack propagation in the spot welded regime, the crack aspect ratio is 1, while for propagation through the parent material, the crack aspect ratio is assumed to be 0.13 or 0.3 for the 1-1mm and 3-3mm sheets, respectively. Combining these variables, the master fatigue life curve can be constructed through:

- Structural stress values determined through finite element analysis.
- Short fatigue crack growth data adjusted for porosity previously ascertained in Chapter 4.
- Integration of the fatigue crack growth relationship with ΔK to determine cycles to failure.

The question of what to use for the initial flaw size, a_i, still remains. Using a value of zero is not a valid solution because ΔK would be zero and the predicted propagation lifetime would be infinity. To address this issue, the concept of an Equivalent Initial Flaw Size (EIFS) is introduced.

EIFS was first proposed by Rudd and Grey [42,43] in 1976 to quantify the quality of fastener holes. The assumption that the US Air Force used for durability prediction at that time was that initial flaws exist as a result of manufacturing and processing operations, and thus small imperfections of 0.127 mm were assumed to exist at every hole in structures of interest. The total fatigue life of a structural component is composed of the time to initiate a crack (N_i) plus the time to propagate the crack to failure: (N_p):

[5.8] $N_f = N_i + N_p$

Fracture mechanics approaches for predicting crack propagation have proven reasonable for most structural applications. Predictions of crack initiation, however, are far more difficult. The initial goal of EIFS was to account for the initiation life of fatal cracks within an LEFM fatigue

crack propagation life prediction methodology for structural details (i.e. fastener holes in the original study) with high stress concentrations.

The EIFS is the size of a hypothetical flaw size that, if in existence at the beginning of the fatigue loading history, would result in the measured lifetime by extrapolating the crack length versus cycles back to 0 cycles. The originally proposed process consisted of fractographic reconstruction of the fatigue crack growth rate through the measurement of fatigue striation spacing. The fatigue crack growth data is then analytically extrapolated back to zero cycles, yielding the EIFS value for a given condition. An example of the back calculation is given in Figure 5.15 [44]. The primary objective is to define an equivalent parameter that accounts for the crack initiation phase of total fatigue life.

More recently, EIFS has been used as an analytical tool to utilize statistical [45–48] and finite element [49–51] approaches for determination of ranges of flaw sizes for a set of fatigue life data with a given input history of parameters including material, residual stress, environment and loading history. These approaches do not necessitate back extrapolation of the EIFS and aim to iteratively determine the distribution of EIFS.

In the context of this research, the EIFS concept was utilized by fitting the predicted lifetimes (using the N_f calculation from Equation [5.6) to the average lifetimes experimentally determined from lap-shear specimens (Figure 5.11, Table 5.3). This was accomplished with a Mathematica script that performed the numerical integration of the predicted lifetime equation for a given geometric and material condition. The results for EIFS fitting against the structural stress range are presented in Figure 5.16. The data was fit to a power law curve as it represented the greatest calculated fit, having a correlation of determination, $R^2 = 0.74$.

[5.9] $a_i = 9.84 \cdot 10^{-21}(\Delta\sigma_{ss})^{5.43}$

In this way, we have determined that there is a correlation between the EIFS and the structural stress value, which allows a reduction in the number of variables for the N_f equation by substituting $a_i = f(\Delta\sigma_{ss})$. It was observed that the EIFS fitting parameter is independent of alloy. For either alloy, the fitting parameters are essentially unchanged.

5.5 Discussion

5.5.1 Fatigue Life Data

Fatigue life testing was performed on lap-shear RSW specimens with variable thicknesses, weld nugget diameters and compositions, the effects of each parameter can be quantified and analyzed. It has been observed that, as shown in Figure 5.10 and Figure 5.11, the 1-1mm samples had a lower average fatigue life at all stress levels, and the Al 5754 samples had a lower average fatigue life than the Al 6111 at the two highest stress levels ($\Delta\sigma_{amp}$ = 14 and 18 MPa). This difference was determined to be statistically significant. At the lower stress levels ($\Delta\sigma_{amp}$ = 7 and 9 MPa) the average fatigue lives of Al 6111 were higher than Al 5754, however, this difference is not a statistically significant difference.

An increase in the fatigue life with an increase in thickness was observed for all conditions. As the weld nugget diameter has been fabricated such that it is dependent on the sheet thickness, it is posited that the thickness effect is actually a weld nugget diameter effect. This is explained by the fact that the spot weld nugget transfers the forces and moments between sheets, and thus a larger weld nugget diameter means a higher joint loading capacity and stiffness. The increase in fatigue life with an increase in sheet thickness has also been observed

for steel and aluminum spot welds in the high cycle regime [3,4,31,37,39,52,53]. There exists no statistically significant difference in average fatigue lives for the different weld nugget diameters on similar thickness and alloying sheets, except in one condition (Figure 5.11). Future experiments could be performed such that the weld nugget diameter is held constant for varying sheet thicknesses to discern the thickness effect more clearly. Tests where the weld nugget diameter is varied with a constant sheet thickness could also be performed to better understand the effect of weld nugget diameter on the fatigue life of the lap-shear joints.

The observed difference in welded joint fatigue lifetimes for the two aluminum alloys investigated is unusual, as this has not been previously reported. Research on aluminum spot welds suggest that the effect of base material strength has no effect on the fatigue life of spot welded lap-shear and coach-peel aluminum samples [4,39]. The effect of alloying, and thereby strength, has on steel spot welds [3,37,38,54] corroborates this previous research in aluminum spot welds, noting that the fatigue life is similar for a wide range of steel alloys. Bonnen [3] suggested that the fatigue life of spot welded specimens is dominated by crack propagation due to the stress concentration provided by the "notch" that occurs due to sheet separation from indentation at the faying surface. For the wide range of steels with varying strength tested in their study, they all had a Paris exponent of approximately 3, explaining the similar lifetimes for seemingly very different steel alloys. From Chapter 4, the Paris exponent for wrought and adjusted 5754 RSW is 4.41 and 3.96, respectively, while for wrought and 6111 RSW it is at 3.82 and 3.63 (Table 4.3). This indicates that, for a given stress level the eyebrow crack is propagating faster in 5754 specimens than in 6111 specimens, explaining the disparity in lifetimes. This is further supported by the EIFS calculation, which included crack propagation information as part of the calibration technique (Section 5.4) and thus included the quantitative differences in

alloying from SFCG testing. Further investigation is needed to clarify this effect, for example performing fatigue life tests on aluminum alloys that have significantly different strengths than the 5754 and 6111 Al tested here (i.e. for 7068-T6 Al, $\sigma_{YS} \approx 680$ MPa). More detailed analysis on the mechanisms controlling the fraction of the eyebrow crack that propagates through the spot welded region would also elucidate on the effect of alloying on fatigue life.

5.5.2 Structural Stress Model

Converting from nominal to structural stress based on the methods described in previous sections aims to normalize the effect of sheet thickness and weld nugget diameter. Indeed, what is found is that the experimental fatigue life is, on average, shorter for the thinner sample due to a reduction in the load transferring capability. The bending ratio also decreases with decreasing sheet thickness, indicative of an increase in the percentage of structural stress attributed to the membrane component. Transforming to structural stress shifts the relative values of the 1-1mm and the $4t^{1/2}$ diameter samples, such that, for a given nominal stress level, the thinner and smaller diameter samples have a higher structural stress value. Thus, this conversion to the structural stress domain provides a more unified representation of the fatigue life for both sheet thicknesses and alloys.

The thickness effect that is found to exist from fatigue life data is usually accounted for in additional steps in the Battelle structural stress methodology. In particular, additional thickness corrections are required for different joints. Hobbacher [55] recommended utilizing a thickness correction method for complex weld geometries, such as butt joints, T-joints, or cruciform joints. Those types of welds were investigated by Potukutchi [2], Hong [56,57] and Kim [58] and it was found that this additional thickness correction was necessary. This was tested in the current

investigation, such that the thickness correction was applied to the structural stress as prescribed in the Battelle method [27]. This correction was performed by dividing the structural stress range by a factor related to the sheet thickness as described below:

$$[5.10]\ \Delta\sigma_{SS}^{TC} = \frac{\Delta\sigma_{SS}}{t^{2-m/2m}}$$

Where t is the sheet thickness in mm, and m is the Paris exponent for crack growth determined experimentally. From Chapter 4, the Paris exponent (m) for wrought and adjusted 5754 RSW is 4.41 and 3.96, respectively, while for the paint-baked wrought and adjusted 6111 RSW it is 3.82 and 3.63, respectively (Table 4.3). Assuming propagation occurs in the resistance spot weld region along 25% of the thickness for eyebrow failure, the values for m become 4.29 and 3.77 for propagation in the 5754 and 6111 lap-shear specimens, respectively. Figure 5.17 (a) displays the original structural stress curve for the experimental data while Figure 5.17 (b) displays the thickness adjusted structural stress values. The values for the thickness correction parameter and fitting parameters for the power law fit for the structural stress curve for the two Paris exponents, along with the industrial standard m = 3.6 [59], are presented in Table 5.5.

In the current investigation, this additional effect of thickness did not need to be further compensated for, as the lap-shear specimen was the only geometry of interest. Furthermore, adjustments for the thickness would result in only minimal changes (Table 5.5) from the original experimentally determined structural stress curve due to the small range of thicknesses tested. If the thickness difference was more pronounced for the structural stress-life curve, or there were substantial differences in specimen geometry, then an additional thickness correction may indeed be necessary.

The objective of this research is to create a predictive master fatigue life relationship that can be implemented for different materials and geometries that have not been experimentally tested. Traditionally, converting from nominal to structural stresses as a correlating parameter for fatigue life data would be enough to be considered a "master curve" [4,10,14,60]. The main shortcoming of this approach is that it is only valid for the materials, geometries and stress levels tested. Since crack propagation plays a dominant role in determining the fatigue life of spot welded specimens [3,4], it is useful for crack propagation behavior to be incorporated in predicting the fatigue life response. The porosity corrected spot weld and parent 5754 and 6111 Al short crack data from Chapter 4 are used to as part of the predicted master fatigue life curve, accounting for the varying growth rates of the different materials in the different regimes. The implication is that crack growth behavior can be implemented to predict the fatigue lifetime response of spot welded joints with significant differences in joint geometry and crack propagation behavior.

The other material parameters being used in this model are the crack aspect ratio and the percentage of propagation life that occurs in the spot weld region versus in the parent sheet. Simple assumptions (such as a constant crack aspect ratio and the percentage of propagation that spans in the spot welded regime) are made based upon fracture surface analysis of the differing geometric conditions. Potential improvements could be made to more accurately define the crack aspect ratio similar to other studies [61–63] that have used FE models to predict the crack aspect ratio evolution in non-symmetrical stress fields, as well as isolating the variables responsible for controlling the fatigue crack propagation path through the spot welds. The methods used in this investigation, however, have been found to be adequate for modeling the fatigue lifetime.

The EIFS technique is used as the initial flaw size in the predicted fatigue life equation and is acts as a surrogate means for accounting for the crack initiation phase of total life. Previous EIFS was determined from fractographic back extrapolations via striation spacing measurement [42,43,64] depend on experimental samples to derive and show an increasing value with increasing applied stress. Molent [65] utilized marker bands on a variety of 7050 aluminum specimens to determine the EIFS in a similar method, but found that the EIFS was approximately constant for a given sample and that the value was highly dependent on the surface condition. Measuring the crack growth from failed samples, however, is expensive and time consuming. Recently, statistical and finite methods [44–51] have been developed to use crack propagation data to estimate the distribution of EIFS. These models necessitate information from C(T) specimen propagation data, such as the Paris' exponents. An analogous approach has been developed in this research, most closely represented by Shahani [46] and Fawaz [48], who compared the measured life with predicted life measurements from FASTRAN and AFGROW lifetime prediction programs. The EIFS values obtained for the fatigue life specimens ranged over three orders of magnitude. One aspect that is consistent with the EIFS model in this research is the observation that the EIFS increased with increasing applied stress level. As this method is designed to account for crack initiation, this type of behavior is expected because the proportion of overall lifetime spent in incubating a crack at an area of localized deformation decreases with increasing stress levels. This is expected, because the contribution to the total stress is primarily elastic in nature.

5.5.3 Model Validation

In order to evaluate the approach used, the experimental fatigue life was compared with the predicted fatigue life, presented in Figure 5.18. Each data point was translated to the predicted

lifetime through its geometric (thickness and weld diameter) and material data (Al 5754 or 6111). As is apparent from the 1:1 comparison line, there was generally good agreement between the predictions and experimentally measured joint life. Bounding lines were chosen to account for the majority of experimental data and reflect the approximately 10x variation on measured life for any one condition. It can be seen that there is good agreement with the predicted model across all structural stress levels tested. The predicted life for the 5754 Al, 3-3mm $5t^{1/2}$ data is generally higher than the measured value but with the 5x bounds.

The validation plot demonstrates that this physics based approach is a reasonable predictive method for fatigue life and is a good approach for future investigations of varying alloys, geometries and loading modes. While standard industrial practice dictates that weld nugget diameters are tied to the sheet thickness, theoretical fatigue lives of diameters far smaller could be modeled by this approach to determine the practical impact of this requirement, without the need for large experimental data sets. This model could also be utilized with other design approaches to further predict and optimize joint lifetime via Integrated Computational Materials Engineering (ICME). For example, spot weld input parameters (i.e. current, hold time) could be adapted to configure the nugget diameter, which could then be translated to fatigue life. Furthermore, the number and locations of the spot welds in a full scale vehicle model could be optimized to determine the ideal size and spacing of the welds depending on the stress state.

5.6 Conclusions

An analytical, physics-based model of joints was developed for estimating the master curve for structural stress based durability analysis of RSW lap-shear joints in aluminum sheet. To develop this approach, finite element modeling of lap-shear RSW aluminum alloys was

completed in Abaqus. The "spider" method was used to represent the spot-weld nugget, consisting of rigid beam elements connecting the periphery to central nodes, while 4-node shell elements were used to represent the remainder of the specimen. Structural stress calculations were conducted using the Battelle method as described by P. Dong [12] for four different geometric configurations at nominal stresses ranging from 1 to 20 MPa. The structural stresses and short crack growth data were used to determine the overall fatigue life through ΔK integration over the thickness. The initial flaw size was calibrated through experimental fatigue life tests and the data was validated through comparisons with experimental data. Overall, an approach for the development of a physics-based constitutive master fatigue life curve is proposed that, when combined with a structural stress methodology, accurately predicts the lifetime of lap-shear aluminum spot welds of varying geometries and load levels.

References

[1] Florea RS, Bammann DJ, Yeldell A, Solanki KN, Hammi Y. Welding parameters influence on fatigue life and microstructure in resistance spot welding of 6061-T6 aluminum alloy. Mater Des 2013;45:456–65. doi:10.1016/j.matdes.2012.08.053.

[2] Potukutchi R, Agrawal H, Perumalswami P. Fatigue Analysis of Steel Mig Welds in Automotive Structures 2004. doi:10.4271/2004-01-0627.

[3] Bonnen JJF, Agrawal H, Amaya MA, Iyengar RM, Kang H, Khosrovaneh AK, et al. Fatigue of Advanced High Strength Steel Spot-Welds 2006;2006.

[4] Shi Y, Guo H. Fatigue performance and fatigue damage parameter estimation of spot welded joints of aluminium alloys 6111-T4 and 5754. Fatigue Fract Eng Mater Struct 2013;36:1081–90. doi:10.1111/ffe.12089.

[5] Wu SN, Ghaffari B, Hetrick E, Li M, Jia ZH, Liu Q. Microstructure characterization and quasi-static failure behavior of resistance spot welds of AA6111-T4 aluminum alloy. Trans Nonferrous Met Soc China (English Ed 2014;24:3879–85. doi:10.1016/S1003-6326(14)63546-9.

[6] Chao YJ. Failure mode of spot welds: interfacial versus pullout. Sci Technol Weld Join 2003.

[7] Zhang H, Senkara J. Resistance Welding: Fundamentals and Applications. vol. 65. 2nd ed. Boca Raton: 2006. doi:10.1017/CBO9781107415324.004.

[8] Tovo R, Livieri P. A numerical approach to fatigue assessment of spot weld joints. Fatigue Fract Eng Mater Struct 2011;34:32–45. doi:10.1111/j.1460-2695.2010.01488.x.

[9] Sheppard DS, Strange M. Fatigue Life Estimation in Resistance Spot Welds: Initiation and Early Growth Phase. Fatigue Fract Eng Mater Struct 1992;15:531–49.

[10] Rupp A, Storzel K, Grubisic V. Computer Aided Dimensioning of Spot-Welded Automotive Structures. SAE Tech Pap 1995;950711. doi:10.4271/950711.

[11] Kang H, Lee Y. Fatigue Life Prediction Methods of Resistance Spot-Welded Joints. Elsevier Inc.; 2012. doi:10.1016/B978-0-12-385204-5.00011-2.

[12] Dong P. A structural stress definition and numerical implementation for fatigue analysis of welded joints. Int J Fatigue 2001;23:865–76. doi:10.1016/S0142-1123(01)00055-X.

[13] Donovan R, Fortune R, Trout R. Elevated Temperature Effects on the Mechanical Properties of Age Hardened 6xxx Series Aluminum Alloy Extrusions. California State University, 2015.

[14] Radaj D, Sonsino CM, Fricke W. Fatigue assessment of welded joints by local approaches. Woodhead; 2006.

[15] Sheppard SD. Further Refinement of a Methodology for Fatigue Life Estimation in Resistance Spot Weld Connections "Further Refinement of a Methodology for Fatigue Life Estimation in Resistance Spot. Weld Connect Am Soc Test Mater 1996:265–

82.

[16] Lin P-C, Pan J. Closed-form structural stress and stress intensity factor solutions for spot welds in commonly used specimens. Eng Fract Mech 2008;75:5187–206. doi:10.1016/j.engfracmech.2008.08.005.

[17] Lin P-C, Pan J. Closed-form structural stress and stress intensity factor solutions for spot welds under various types of loading conditions. Int J Solids Struct 2008;45:3996–4020. doi:10.1016/j.ijsolstr.2008.02.006.

[18] Lin P-C, Lin S-H, Pan J. Modeling of failure near spot welds in lap-shear specimens based on a plane stress rigid inclusion analysis. Eng Fract Mech 2006;73:2229–49. doi:10.1016/j.engfracmech.2006.03.017.

[19] Kang H, Dong P, Hong J. Fatigue analysis of spot welds using a mesh-insensitive structural stress approach. Int J Fatigue 2007;29:1546–53. doi:10.1016/j.ijfatigue.2006.10.025.

[20] Weld button criteria, recommended practices for test methods for evaluating the resistance spot welding behavior of automotive sheet steel metal. 1997.

[21] Pan N. Spot welds fatigue life prediction with cyclic strain range. Int J Fatigue 2002;24:519–28. doi:10.1016/S0142-1123(01)00157-8.

[22] Sripichai K, Asim K, Pan J. Stress intensity factor solutions for estimation of fatigue lives of laser welds in lap-shear specimens. Eng Fract Mech 2011;78:1424–40. doi:10.1016/j.engfracmech.2011.02.022.

[23] Wang DA, Pan J. A computational study of local stress intensity factor solutions for kinked cracks near spot welds in lap-shear specimens. Int J Solids Struct 2005;42:6277–98. doi:10.1016/j.ijsolstr.2005.05.036.

[24] Sadowski AJ, Rotter JM. Solid or shell finite elements to model thick cylindrical tubes and shells under global bending. Int J Mech Sci 2013;74:143–53. doi:10.1016/j.ijmecsci.2013.05.008.

[25] Andersson J, Deleskog J. Fatigue Life and Stiffness of the Spider Spot Weld Model. Chalmers University of Technology, 2014.

[26] Huang L, Shi Y, Guo H, Su X. Fatigue behavior and life prediction of self-piercing riveted joint. Int J Fatigue 2016;88:96–110. doi:10.1016/j.ijfatigue.2016.03.015.

[27] Dong P, Huther M. Guide for Application of the Mesh Insensitive Methodology: Structural Stress. vol. 33. 2012.

[28] Dassault Systèmes Simulia. Abaqus CAE User's Manual. Abaqus 612 2012:1174.

[29] Orts DH. Fatigue Strength of Spot Welded Joints in a HSLA Steel. Soc Automot Eng INC 1981. doi:10.4271/810355.

[30] Kang H. Fatigue Damage Parameter of Spot Welded Joints Under Proportional Loading. Int J Automot Technol 2005;6:285–91.

[31] Jung WW, Jang PK. Fatigue Failure and Reinforcing Method of Spot Welded Area at the Stage of Vehicle Development 1996.

[32] Swellam MH, Aś GB, Lawrence F V. a Fatigue Design Parameter for Spot Welds. Fatigue Fract Eng Mater Struct 1994;17:1197–204. doi:10.1111/j.1460-2695.1994.tb01408.x.

[33] Dong P, Hong JK, Cao Z. Stresses and stress intensities at notches: "anomalous crack growth" revisited. Int J Fatigue 2003;25:811–25. doi:10.1016/S0142-1123(03)00130-0.

[34] Zhang S. Fracture mechanics solutions to spot welds. Int J Fract 2001;112:247–74.

[35] Wang X, Lambert SB. Stress intensity factors and weight functions for high ratio semi-elliptical surface cracks in finite-thickness plates. Eng Fract Mech 1997;57:13–24. doi:http://dx.doi.org/10.1016/S0013-7944(97)00018-0.

[36] Newman JC, Raju IS. An empirical stress-intensity factor equation for the surface crack. Eng Fract Mech 1981;15:185–92. doi:10.1016/0013-7944(81)90116-8.

[37] Davidson JA, Imhof EJ. The Effect of Tensile Strength on the Fatigue Life of Spot-Welded Sheet Steels 1984. doi:10.4271/840110.

[38] Gentilcore M. An Assessment of the Fatigue Performance of Automotive Sheet Steels. SAE Int Conf 2004. doi:10.4271/2004-01-0629.

[39] Shi Y, Guo H. Stress Intensity Factor Based Spot Welds Fatigue Life Prediction Model 2013. doi:10.4271/2013-01-0389.

[40] Sanders WW, Lawrence Jr F V, Lawrence, Jr. Fatigue Behavior of Aluminum Alloy Weldments. In: Hoeppner DW, editor. Fatigue Test. Weldments, 1978, p. 22–34.

[41] Handbook Metallic Materials and Elements for Aerospace Vehicle Structures. 2003.

[42] Rudd JL, Gray TD. Equivalent Initial Quality Method. Air Force Flight Dyn Libr AFFDL-TM-76-83 1976.

[43] Rudd JL, Gray D. Quantification of Fastener-Hole Quality. J Aircr 1978;15:143–7.

[44] Johnson WS. The history, logic and uses of the Equivalent Initial Flaw Size approach to total fatigue life prediction. Procedia Eng 2010;2:47–58. doi:10.1016/j.proeng.2010.03.005.

[45] Mattos JD, Chaves CE. Towards a methodology for the practical applications of the EIFS (Equivalent Initial Flaw Size) concept. Lat Am J Solids Struct 2013;10:845–57.

[46] Shahani AR, Moayeri Kashani H. Assessment of equivalent initial flaw size estimation methods in fatigue life prediction using compact tension specimen tests. Eng Fract Mech 2013;99:48–61. doi:10.1016/j.engfracmech.2013.01.007.

[47] Liu Y, Mahadevan S. Probabilistic fatigue life prediction using an equivalent initial flaw size distribution. Int J Fatigue 2008;31:476–87. doi:10.1016/j.ijfatigue.2008.06.005.

[48] Fawaz SA. Equivalent initial flaw size testing and analysis of transport aircraft skin

splices. Fatigue Fract Eng Mater Struct 2003;26:279–90. doi:10.1046/j.1460-2695.2003.00637.x.

[49] Sankararaman S, Ling Y, Mahadevan S. Statistical inference of equivalent initial flaw size with complicated structural geometry and multi-axial variable amplitude loading. Int J Fatigue 2010;32:1689–700. doi:10.1016/j.ijfatigue.2010.03.012.

[50] Alves ASF, Sampayo LMCMV, Correia JAFO, De Jesus AMP, Moreira PMGP, Tavares PJS. Fatigue Life Prediction Based on Crack Growth Analysis Using an Equivalent Initial Flaw Size Model: Application to a Notched Geometry. Procedia Eng 2015;114:730–7. doi:10.1016/j.proeng.2015.08.018.

[51] Correia J, Blasón S, De Jesus A, Canteli A, Moreira P, Tavares PJ. Fatigue life prediction based on an equivalent initial flaw size approach and a new normalized fatigue crack growth model 2016. doi:10.1016/j.engfailanal.2016.04.003.

[52] Pollard B. Fatigue Strength of Spot Welds in Titanium-Bearing HSLA Steels. SAE Int Congr Expo 1982. doi:10.4271/820284.

[53] Zhang Y, Taylor D. Sheet thickness effect of spot welds based on crack propagation. Eng Fract Mech 2000;67:55–63. doi:10.1016/S0013-7944(00)00029-1.

[54] Nordberg H. Fatigue Properties of Stainless Steel Lap Joints . Spot Welded , Adhesive Bonded , Weldbonded , Laser Welded and Clinched Joints ff Stainless Steel Sheets-. Engineering 2005;2005. doi:10.4271/2005-01-1324.

[55] Hobbacher A. Recomendations for Fatigue Design of Welded Joints and Components. 2015. doi:10.1007/978-3-319-23757-2.

[56] Hong JK. Evaluation Of Weld Root Failure Using Battelle Structural Stress Method. J Offshore Mech Arct Eng 2013;135:7. doi:10.1115/OMAE2010-20387.

[57] Hong JK. Fatigue Evaluation Procedure Development for Aluminum Alloy Spot Welds Using the Battelle Structural Stress Method Fatigue Behavior of Aluminum Alloy Spot Welds. SAE Int Conf 2015. doi:10.4271/2015-01-0545.Copyright.

[58] Kim S-M, Kim M-H. Incorporating mesh-insensitive structural stress into the fatigue assessment procedure of common structural rules for bulk carriers. Int J Nav Archit Ocean Eng 2015;7:10–24. doi:10.1515/ijnaoe-2015-0002.

[59] Dong P, Prager M, Osage D. The Design Master S-N Curve In ASME Div 2 Rewrite And its Validations. Weld World 2007;51:53–63. doi:10.1007/BF03266573.

[60] Radaj D, Vormwald M. Advanced Methods of Fatigue Assessment. Berlin: Springer-Verlag; 2013. doi:10.1007/978-3-642-30740-9.

[61] Toribio J, Matos JC, González B. Aspect ratio evolution associated with surface cracks in sheets subjected to fatigue. Int J Fatigue 2016;92:588–95. doi:10.1016/j.ijfatigue.2016.03.028.

[62] Wallbrink C, Peng D, Jones R, Dayawansa PH. Predicting the fatigue life and crack aspect

ratio evolution in complex structures. Theor Appl Fract Mech 2006;46:128–39. doi:10.1016/j.tafmec.2006.07.004.

[63] Mahmoud MA, Hosseini A. Assessment of stress intensity factor and aspect ratio variability of surface cracks in bending plates. Eng Fract Mech 1986;24:207–21. doi:10.1016/0013-7944(86)90052-4.

[64] Moreira PMGP, de Matos PFP, de Castro PMST. Fatigue striation spacing and equivalent initial flaw size in Al 2024-T3 riveted specimens. Theor Appl Fract Mech 2005;43:89–99. doi:10.1016/j.tafmec.2004.12.005.

[65] Molent L, Sun Q, Green AJ. Characterisation of equivalent initial flaw sizes in 7050 aluminium alloy. Fatigue Fract Eng Mater Struct 2006;29:916–37. doi:10.1111/j.1460-2695.2006.01050.x.

Tables

Table 5.1 - Structural stress and its components values for an applied force / stress for each geometric condition.

		1-1mm, 4 $t^{1/2}$			1-1mm, 5 $t^{1/2}$		
F_{app} (N)	σ_{app} (MPa)	σ_{mem} (MPa)	σ_{bend} (MPa)	σ_{SS} (MPa)	σ_{mem} (MPa)	σ_{bend} (MPa)	σ_{SS} (MPa)
50.8	1	5.86	20.01	25.87	5.03	17.97	22.99
76.2	1.5	8.80	30.01	38.81	7.54	26.60	34.14
101.6	2	11.73	40.02	51.75	10.05	35.47	45.52
152.4	3	17.59	60.02	77.62	15.08	53.20	68.28
228.6	4.5	26.39	90.03	116.43	22.62	79.80	102.42
304.8	6	35.19	120.05	155.24	30.16	106.40	136.56
508	10	58.65	200.08	258.73	50.26	177.33	227.60
762	15	87.97	300.12	388.09	75.40	266.00	341.40
1016	20	117.30	400.16	517.45	100.53	354.67	455.20

		3-3mm, 4 $t^{1/2}$			3-3mm, 5 $t^{1/2}$		
F_{app} (N)	σ_{app} (MPa)	σ_{mem} (MPa)	σ_{bend} (MPa)	σ_{SS} (MPa)	σ_{mem} (MPa)	σ_{bend} (MPa)	σ_{SS} (MPa)
152.4	1	4.09	15.19	19.29	3.61	13.67	17.28
228.6	1.5	6.14	22.79	28.93	5.41	20.51	25.92
304.8	2	8.19	30.39	38.57	7.22	27.35	34.56
457.2	3	12.28	45.58	57.86	10.82	41.02	51.84
685.8	4.5	18.42	68.37	86.79	16.23	61.53	77.77
914.4	6	24.56	91.16	115.72	21.65	82.04	103.69
1524	10	40.93	151.94	192.87	36.08	136.74	172.81
2286	15	61.40	227.91	289.31	54.11	205.11	259.22
3048	20	81.86	303.88	385.74	72.15	273.47	345.62

Table 5.2 – Test matrix of conditions investigated with fatigue life experiments for the structural stress based fatigue life model.

Material	Sheet Thickness	Weld Diameter	
Al 5754	1-1 mm	$d_{wn} = 4\ t^{1/2} = 4$ mm	$d_{wn} = 5\ t^{1/2} = 5$ mm
Al 6111	1-1 mm	$d_{wn} = 4\ t^{1/2} = 4$ mm	$d_{wn} = 5\ t^{1/2} = 5$ mm
Al 5754	3-3 mm	$d_{wn} = 4\ t^{1/2} = 6.93$ mm	$d_{wn} = 5\ t^{1/2} = 8.66$ mm
Al 6111	3-3 mm	$d_{wn} = 4\ t^{1/2} = 6.93$ mm	$d_{wn} = 5\ t^{1/2} = 8.66$ mm

Table 5.3 - Average lifetimes and standard deviations for eyebrow failed or run-out lap-shear specimens per condition per stress level.

	Cycles to failure, N_f			
$\Delta\sigma_{app}$ / Condition	**7 MPa**	**9 MPa**	**14 MPa**	**18 MPa**
Al 5754 1-1mm, $4t^{1/2}$	3.67×10^6 $\pm 1.01 \times 10^6$	1.88×10^6 $\pm 1.09 \times 10^6$	- -	- -
Al 5754 1-1mm, $5t^{1/2}$	4.4×10^6 $\pm 1.51 \times 10^6$	1.9×10^6 $\pm 4.90 \times 10^5$	5.6×10^4 $\pm 8.41 \times 10^3$	2.4×10^4 $\pm 3.02 \times 10^3$
Al 5754 3-3mm, $4t^{1/2}$	8.1×10^6 $\pm 7.15 \times 10^5$	3.1×10^6 $\pm 3.03 \times 10^5$	9.5×10^4 $\pm 2.34 \times 10^4$	4.1×10^4 $\pm 4.10 \times 10^3$
Al 5754 3-3mm, $5t^{1/2}$	1.00×10^7 ± 0	2.74×10^6 $\pm 1.82 \times 10^6$	9.65×10^4 $\pm 6.04 \times 10^3$	3.76×10^4 $\pm 2.02 \times 10^3$
Al 6111 1-1mm, $4t^{1/2}$	4.35×10^6 $\pm 1.01 \times 10^6$	2.62×10^6 $\pm 1.10 \times 10^6$	- -	- -
Al 6111 1-1mm, $5t^{1/2}$	6.10×10^6 $\pm 2.55 \times 10\ 6$	2.51×10^6 $\pm 3.33 \times 10\ 5$	8.81×10^4 $\pm 5.75 \times 10\ 3$	$3.69 \times 10\ 4$ $\pm 1.53 \times 10\ 3$
Al 6111 3-3mm, $4t^{1/2}$	$9.91 \times 10\ 6$ $\pm 9.29 \times 10^4$	$3.90 \times 10\ 6$ $\pm 9.39 \times 10^5$	1.98×10^5 $\pm 3.22 \times 10^4$	7.39×10^4 $\pm 1.69 \times 10^3$
Al 6111 3-3mm, $5t^{1/2}$	1.00×10^7 ± 0	4.56×10^6 $\pm 1.55 \times 10^6$	3.34×10^5 $\pm 7.90 \times 10^4$	6.79×10^4 $\pm 5.76 \times 10^3$

Table 5.4 – EIFS (in meters) per geometric condition and stress level.

	EIFS, a_i (m)			
Condition \ **$\Delta\sigma_{app}$**	**7 MPa**	**9 MPa**	**14 MPa**	**18 MPa**
Al 5754 1-1mm, $4t^{1/2}$	4.71×10^{-9}	3.73×10^{-8}	-	-
Al 5754 1-1mm, $5t^{1/2}$	5.63×10^{-9}	4.34×10^{-8}	2.31×10^{-6}	1.99×10^{-6}
Al 5754 3-3mm, $4t^{1/2}$	9.5×10^{-9}	3.5×10^{-8}	-	-
Al 5754 3-3mm, $5t^{1/2}$	4.22×10^{-9}	1.11×10^{-8}	2.04×10^{-7}	8.66×10^{-7}
Al 6111 1-1mm, $4t^{1/2}$	5.1×10^{-9}	7.7×10^{-9}	8.3×10^{-7}	8.9×10^{-7}
Al 6111 1-1mm, $5t^{1/2}$	6.83×10^{-9}	4.33×10^{-8}	2.26×10^{-7}	3.01×10^{-6}
Al 6111 3-3mm, $4t^{1/2}$	9.54×10^{-9}	6.84×10^{-8}	5.00×10^{-7}	2.88×10^{-7}
Al 6111 3-3mm, $5t^{1/2}$	7.51×10^{-9}	7.71×10^{-9}	4.14×10^{-7}	1.38×10^{-6}

Table 5.5 - Thickness correction comparison. The variables A and B represent the power law fit exponents for the experimental structural stress fit ($\Delta\sigma_{ss} = A(N_f)^B$). The first row represents no thickness correction.

m	**$(1mm)^{(2-m)/2m}$**	**$(3mm)^{(2-m)/2m}$**	**A**	**B**
-	-	-	1757	-0.157
3.6	1	0.78	2119	-0.157
4.2975	1	0.75	2304	-0.158
3.7725	1	0.77		

Figures

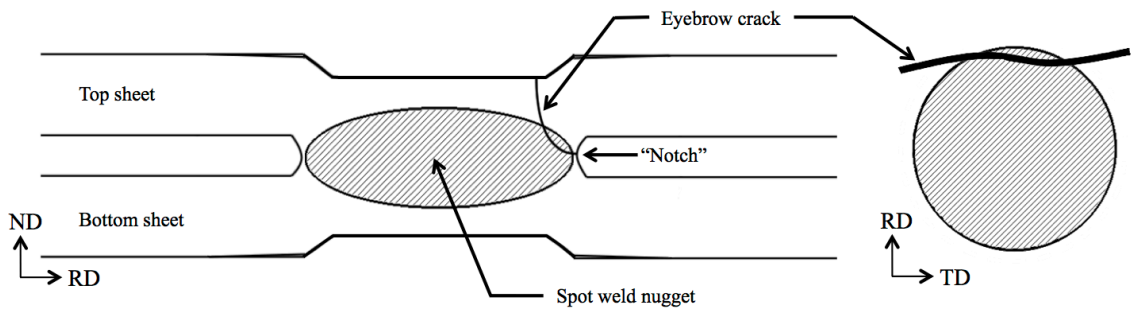

Figure 5.1 - Schematic of lap-shear specimen noting the faying surface, notch from nugget indentation and the crack path of an eyebrow crack.

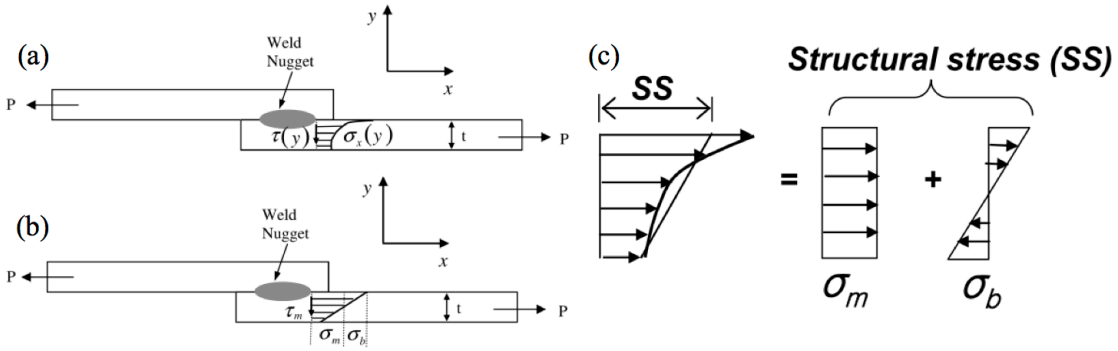

Figure 5.2 - Schematic of stress linearization. (a) Non-linear state at the spot weld edge, (b,c) linearized stress state.

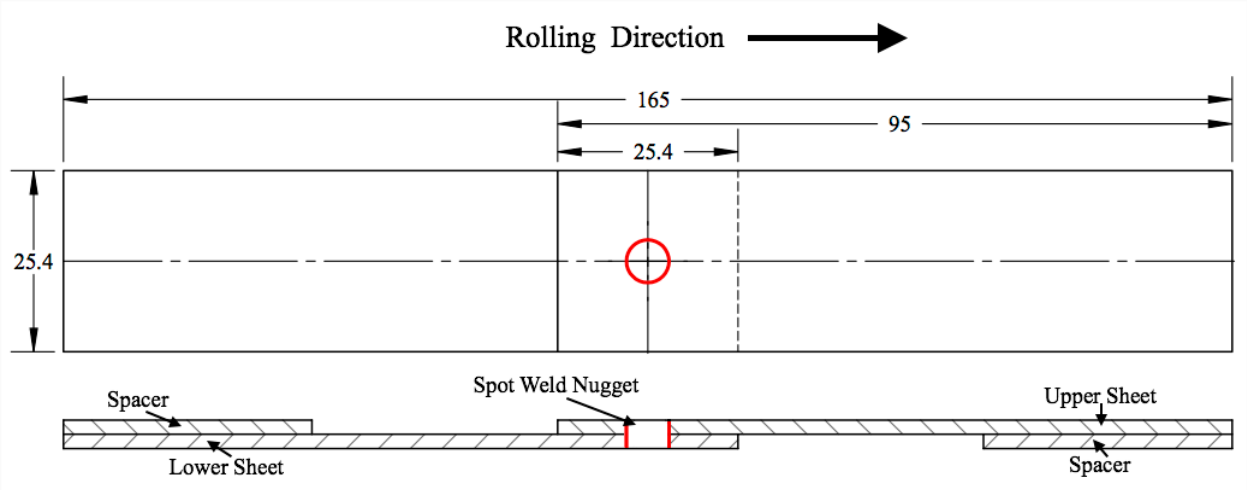

Figure 5.3 - Lap-shear specimen design. Units are in mm.

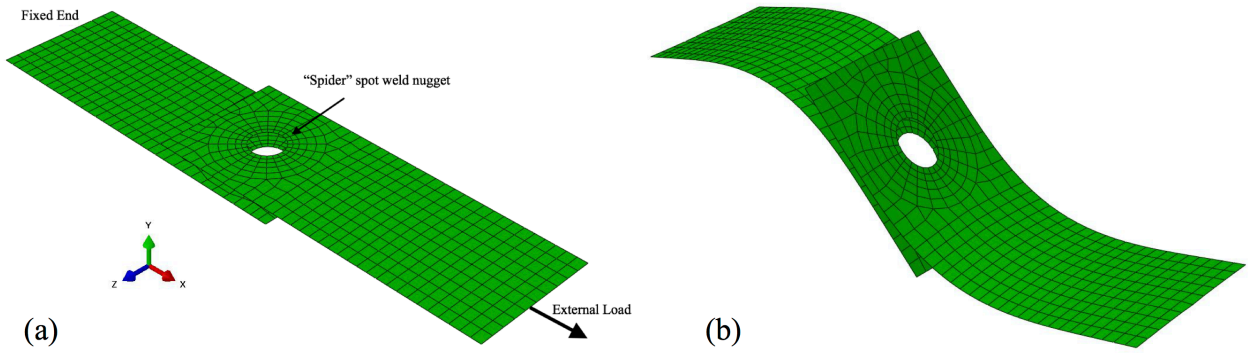

Figure 5.4 - Representative FE mesh of lap-shear specimen. (a) Undeformed model, noting the boundary conditions and "spider" mesh representing the spot weld nugget, (b) the specimen shape under the effect of an applied load. (displacements are exaggerated)

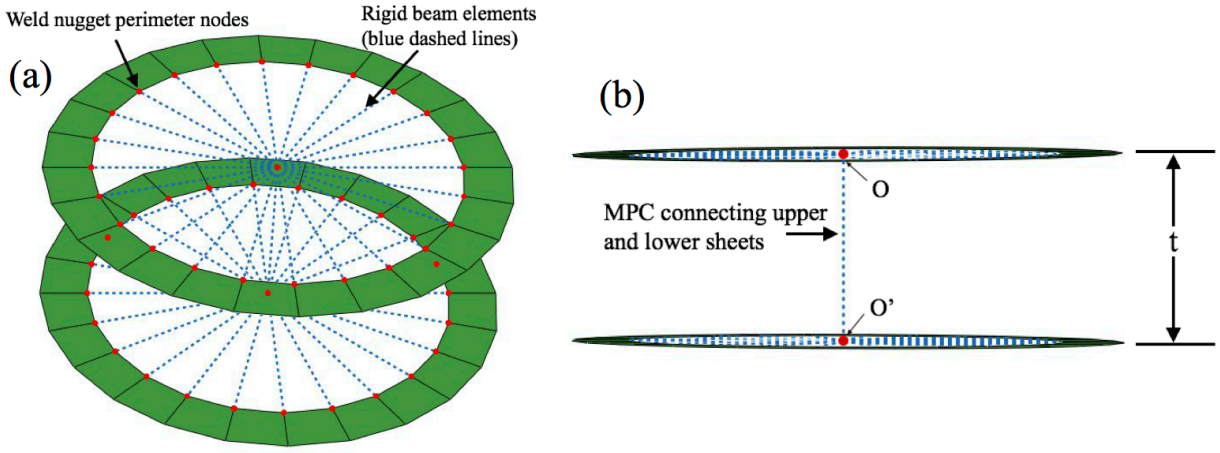

Figure 5.5 - Spider method with rigid beam (MPC) elements (a) connecting the weld periphery to central nodes (b) connecting the central nodes between sheets together

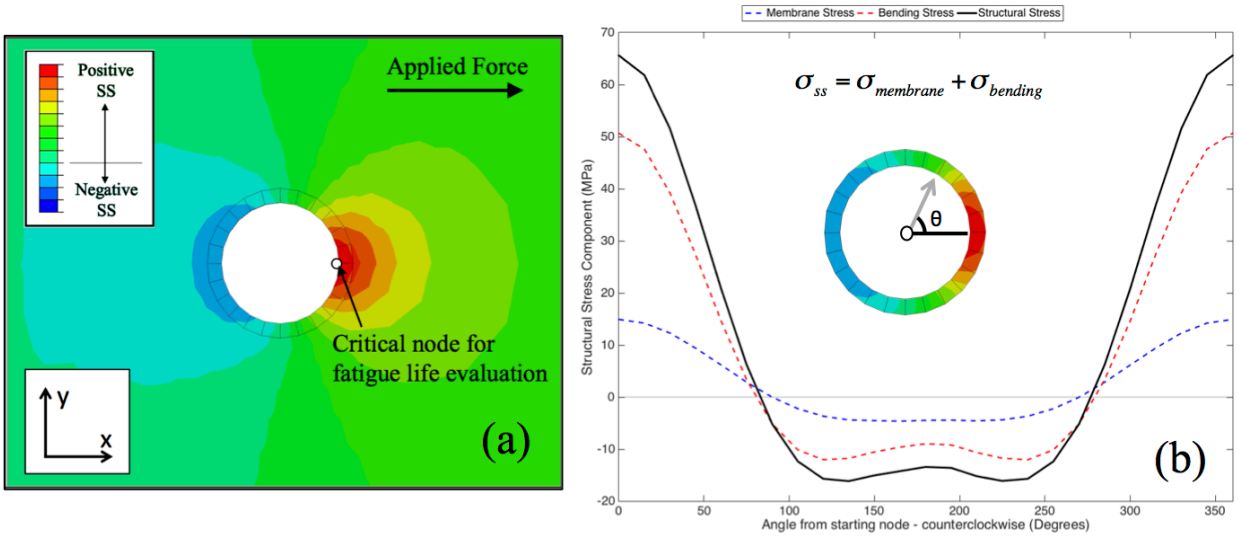

Figure 5.6 - Determination of the critical node for structural stress calculation. (a) FE mesh showing the distribution of structural stresses around the weld nugget perimeter and (b) variation of the structural stress and its components versus node position.

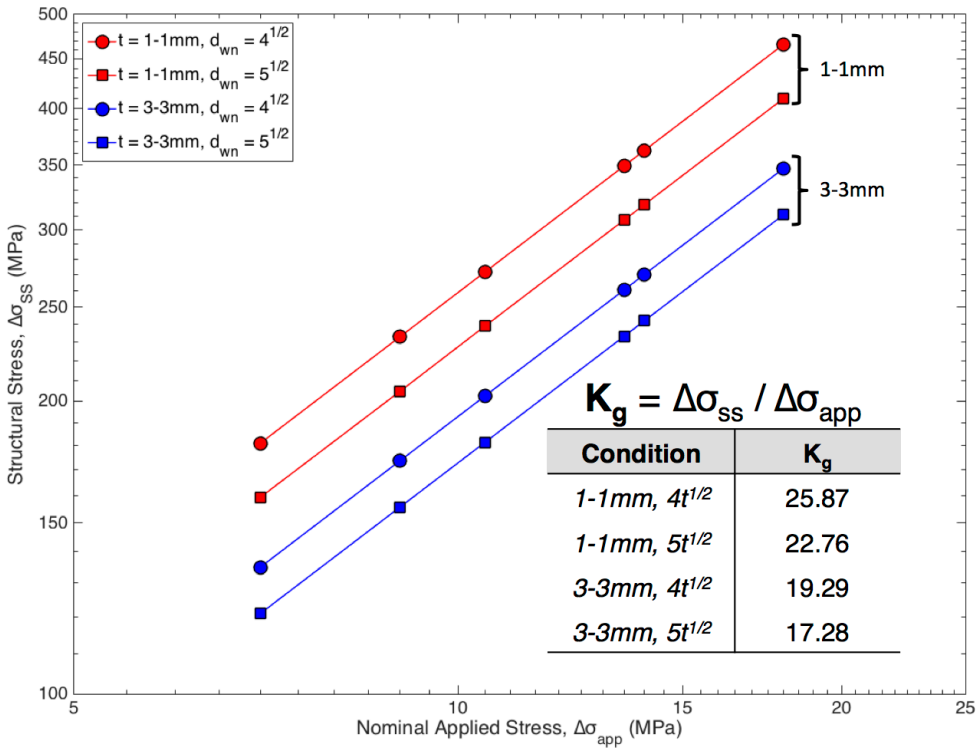

Figure 5.7 - Relationship between nominal applied stress and structural stress. The structural stress based stress concentration factor, K_g, is listed for each geometric condition.

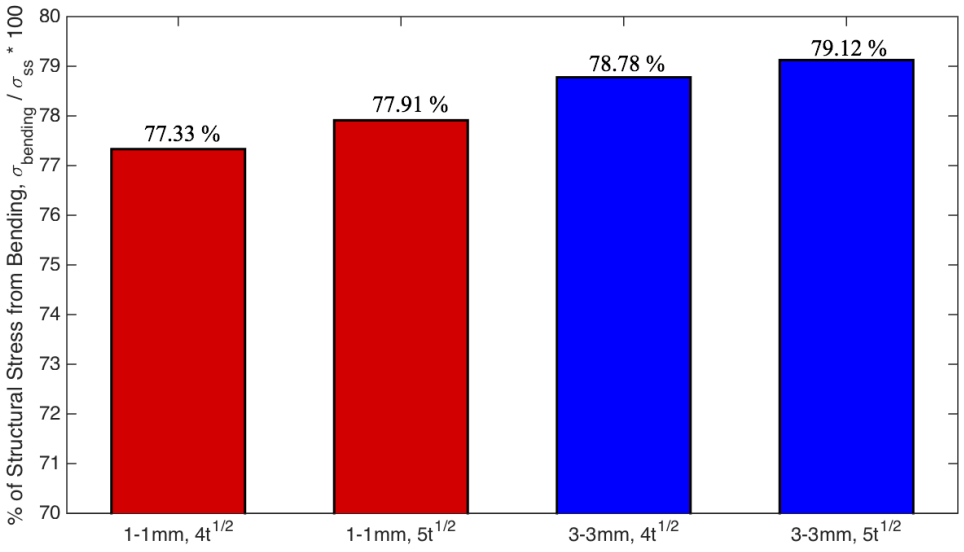

Figure 5.8 - Contribution of bending stress to the structural stress for each of the geometric conditions.

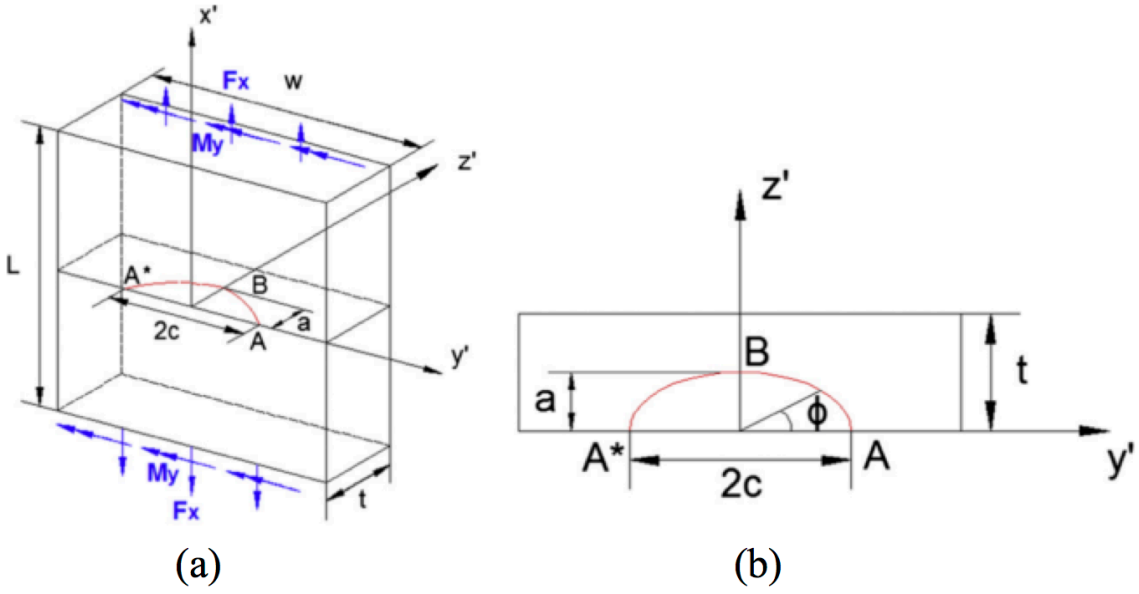

Figure 5.9 - Schematic of semi-elliptical crack shape [26]. (a) Semi-elliptical surface crack under remote tension and bending (b) Crack front plane. The surface point, A, and deepest point, B, are labeled.

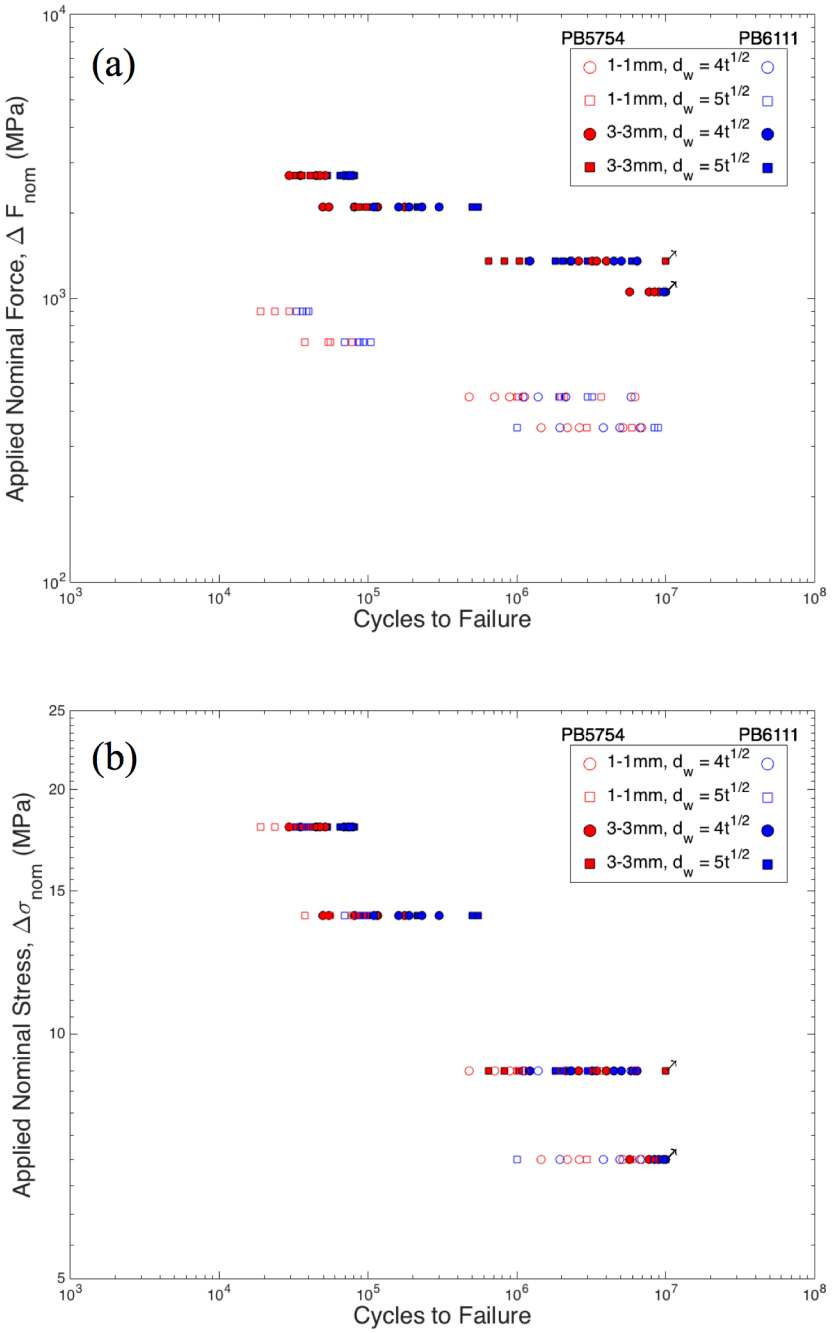

Figure 5.10 - Fatigue life curves for experimental lap-shear RSW specimens. (a) Applied force amplitude vs. cycles to failure (b) Applied nominal stress amplitude vs. cycles to failure. Arrows indicate run-outs (10 million cycles without failure)

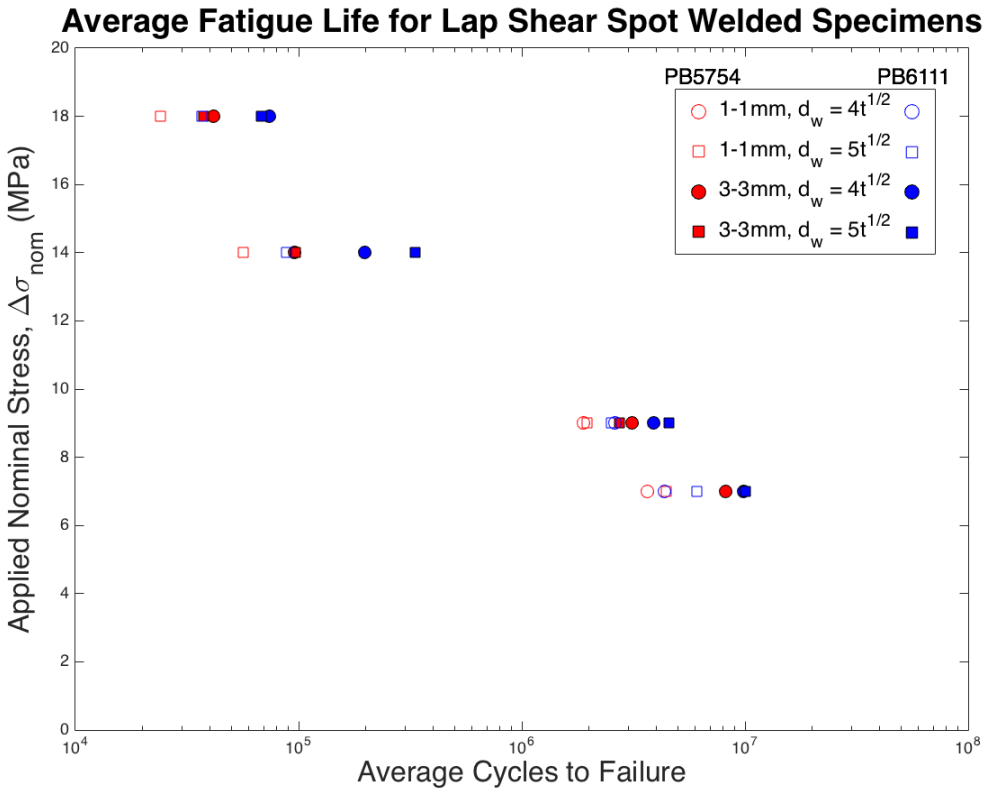

Figure 5.11 - Average fatigue life at each applied stress level for each geometric/alloy condition.

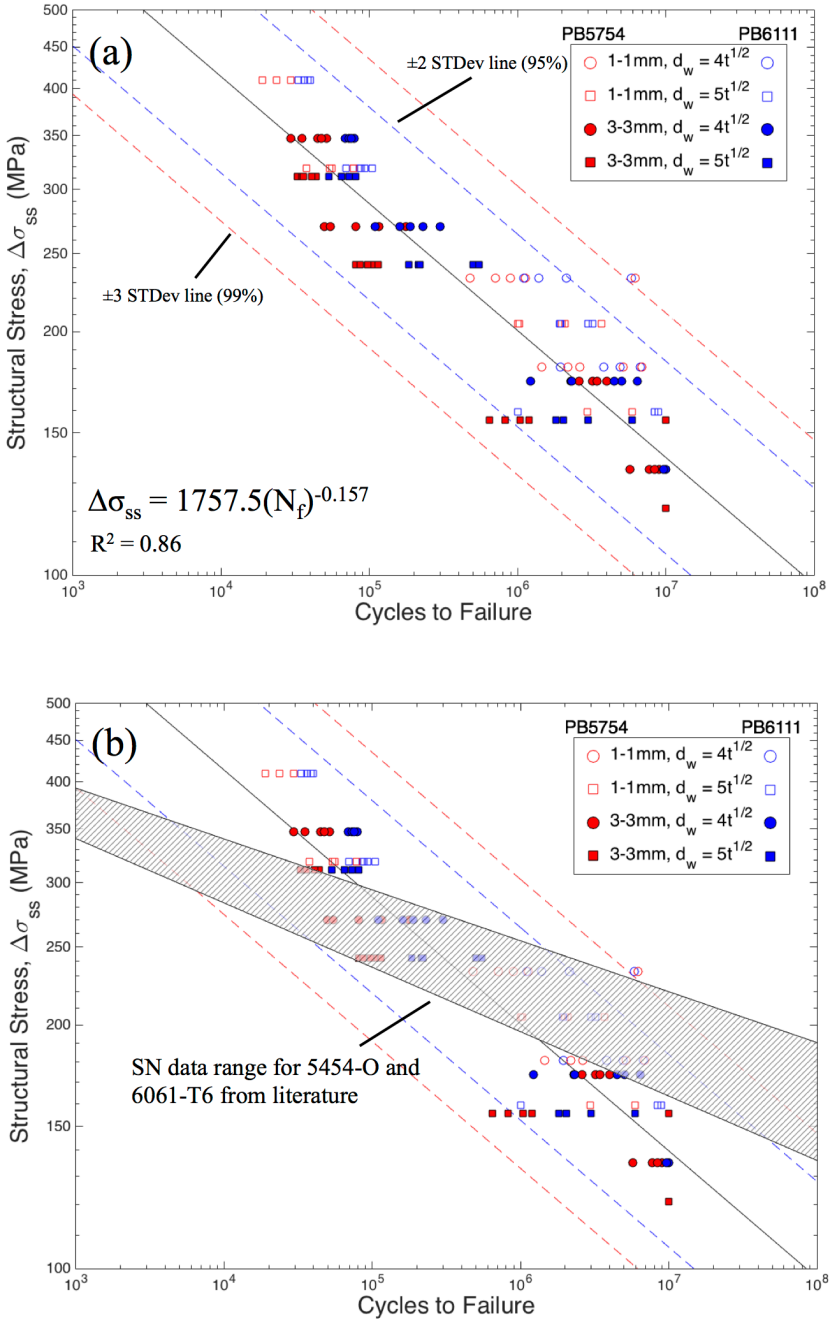

Figure 5.12 - Fatigue life plotted versus calculated structural stress for all experimental lap-shear specimens. (a) The structural stress conversion represents a good representation of the lifetime, as shown by the power law fit, (b) comparison to S-N data from 5754-O [40] and 6061-T6 [41] unnotched specimens (R = 0).

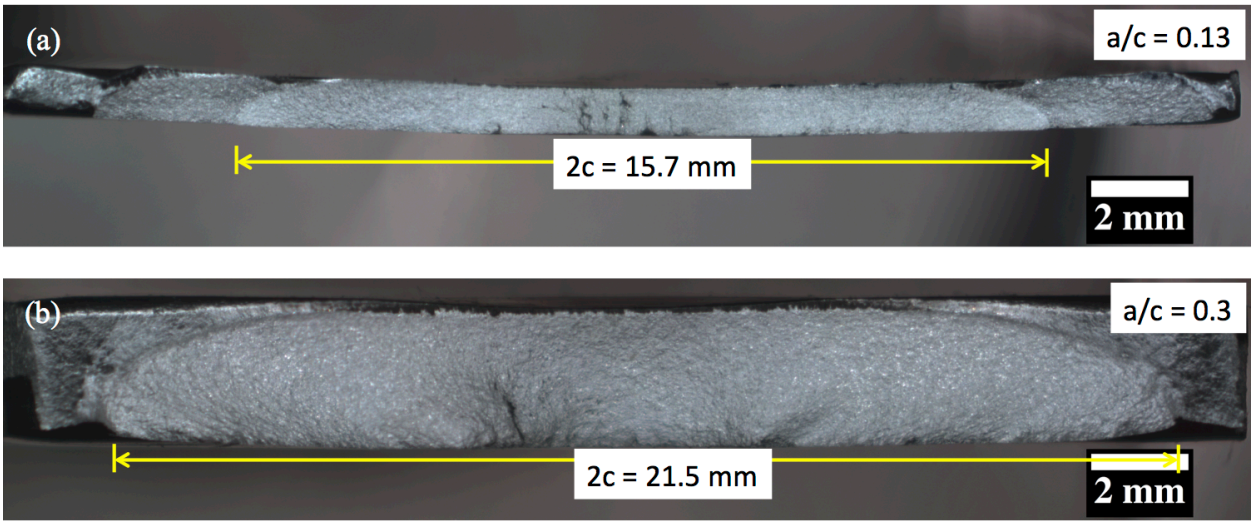

Figure 5.13 - Representative fractographs of lap-shear specimens to determine aspect ratio (a) 1-1mm $5t^{1/2}$ 5754 failure at 3,692,008 cycled at $\Delta\sigma_{app}$ = 9MPa (b) 3-3mm $4t^{1/2}$ 6111 failure at 218,902 cycled at $\Delta\sigma_{app}$ = 14 MPa.

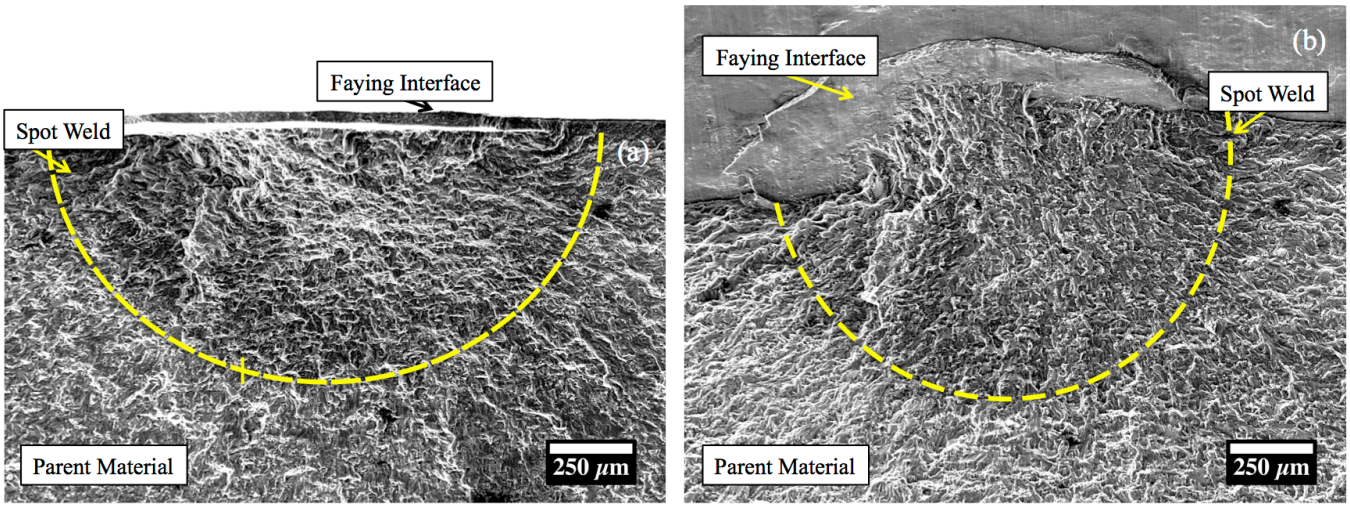

Figure 5.14 - Representative fractograph of weld region of the eyebrow crack and transition to the crack in the parent sheet. 3-3mm $5t^{1/2}$ 5754 failed at 2,000,747 cycles cycled at $\Delta\sigma_{app}$ = 9 MPa. (a) Fracture surface normal to the loading direction, (b) the same surface surface tiled 40°.

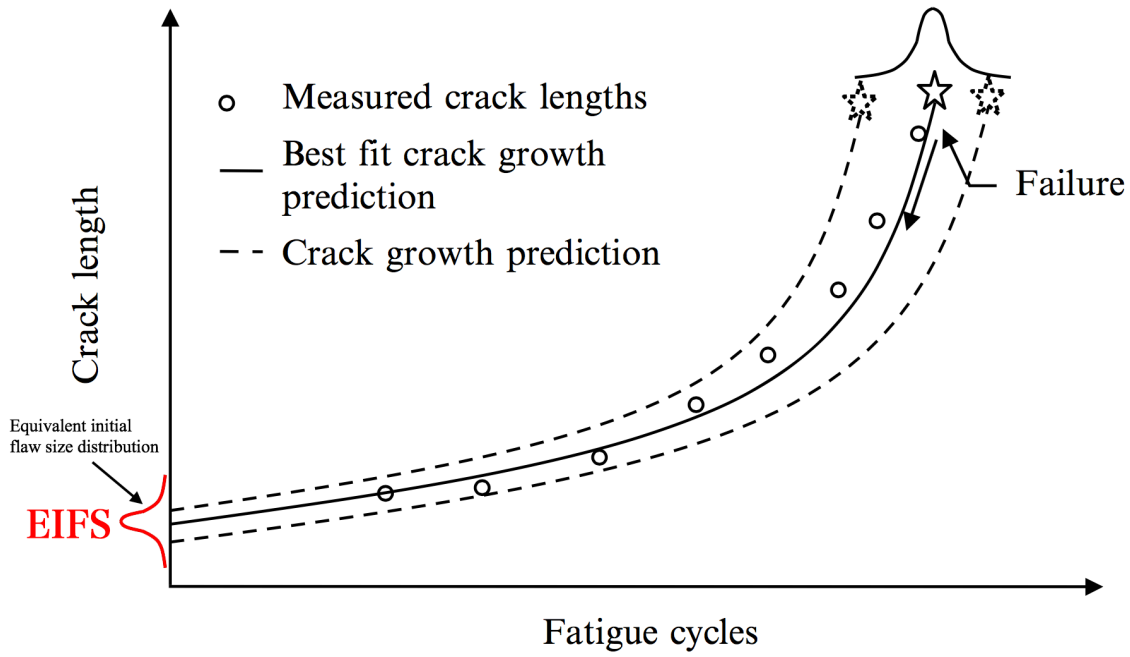

Figure 5.15 - Example of backtracking to analytically determine the EIFS [48].

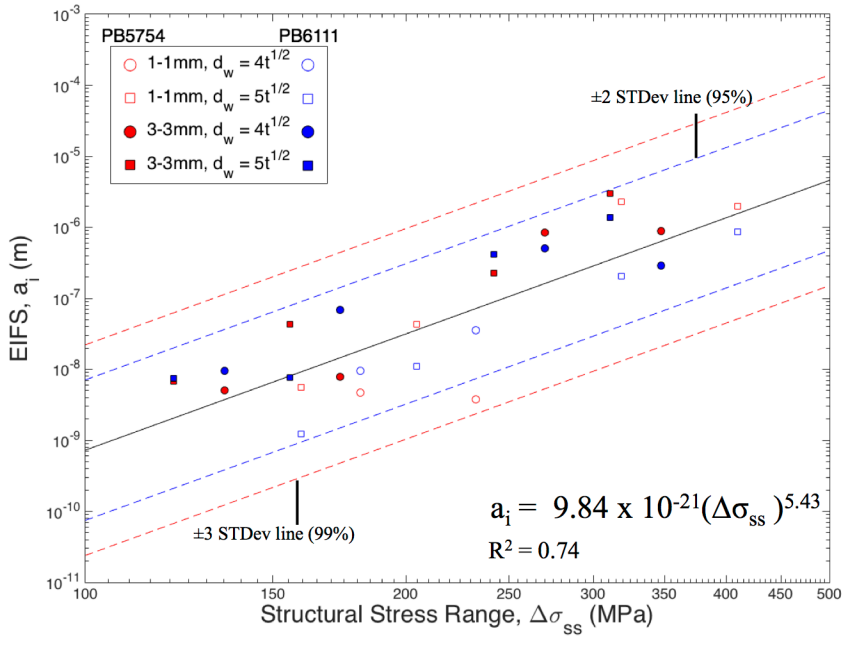

Figure 5.16 - Equivalent initial flaw size (EIFS) fit for all geometric and material conditions.

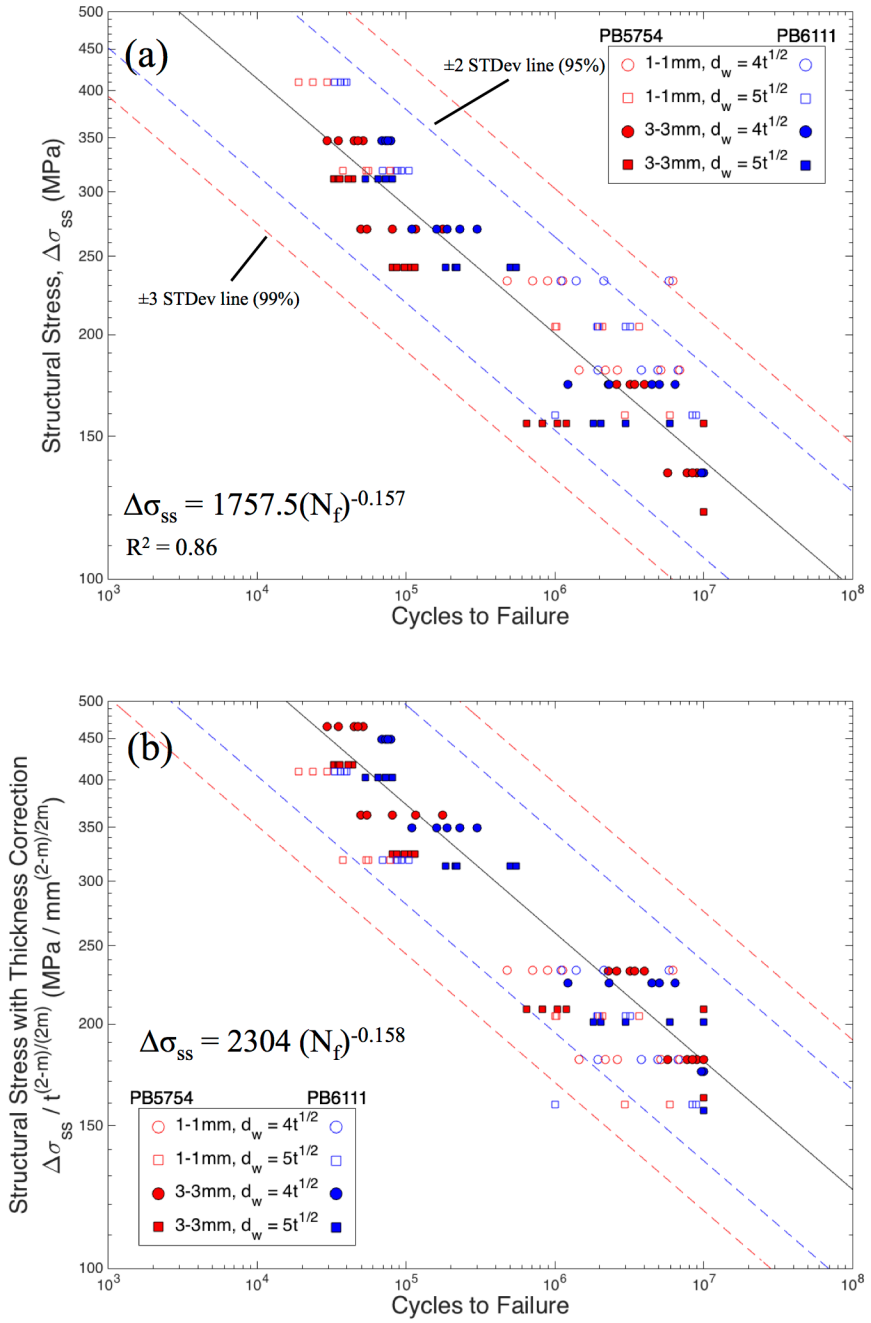

Figure 5.17 – (a) Experimentally determined structural stress curve and (b) the thickness adjusted structural stress curve.

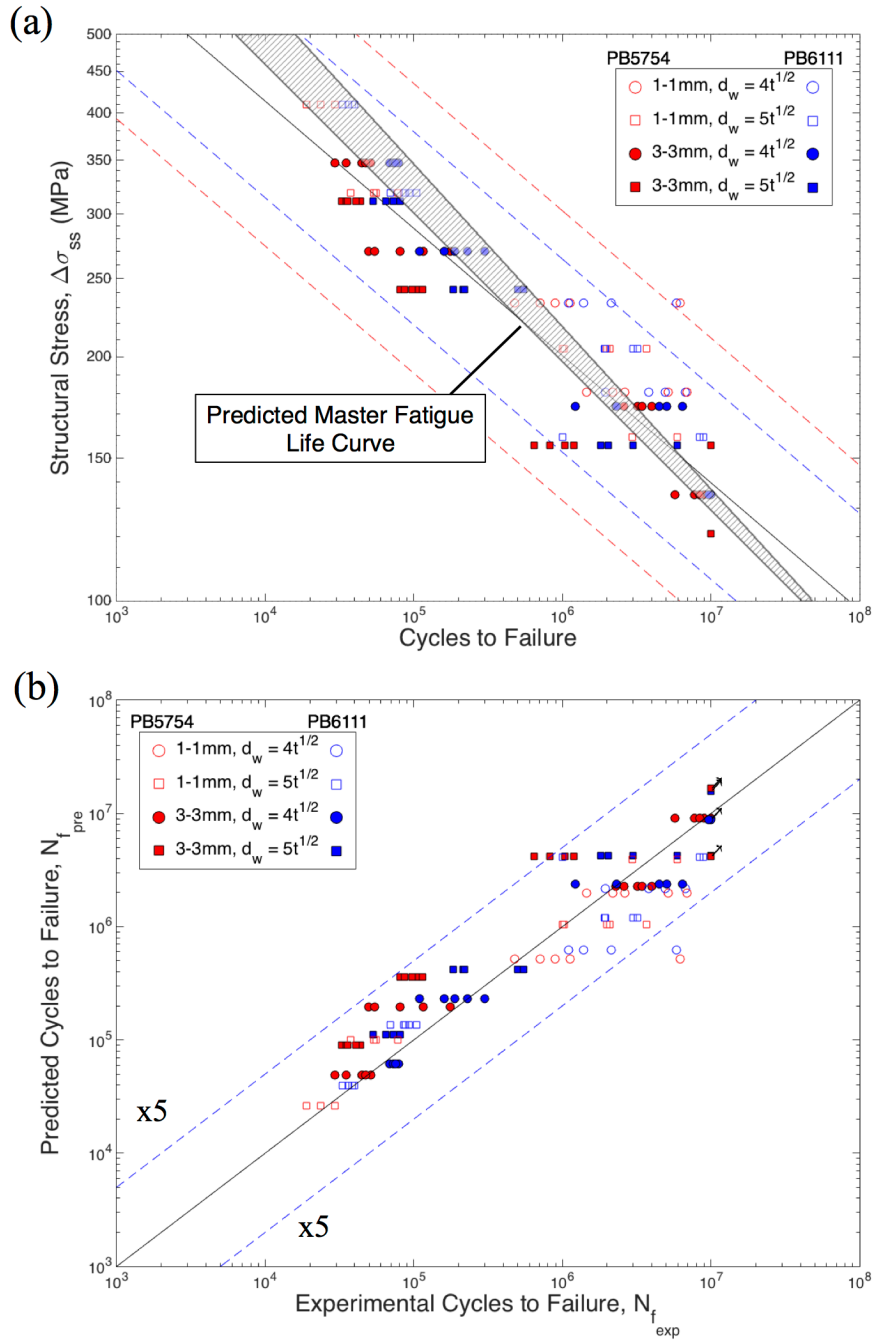

Figure 5.18 – (a) The predicted master fatigue life curve overlaid on the experimentally determined structural stress curve and (b) predicted vs. experimental fatigue life for lap-shear specimens with varying geometric and alloy conditions.

Chapter 6

Conclusions and Future Work

6.1 Conclusions

A study of the short fatigue crack growth behavior performed on wrought and resistance spot welded 5754 and 6111 aluminum alloys was conducted to characterize the propagation behavior of spot welded joints and a structural stress based master fatigue life relationship was developed to predict the lifetime of future joints with varying geometries and alloying elements. The specific conclusions were found:

1. Short fatigue crack growth rates for the two wrought aluminum alloys were similar for a given driving force, indicating that the propagation behavior is not strongly affected by alloying, heat treatment or stress level.

2. Short fatigue crack growth for the two weld fusion zones, however, is strongly influenced by porosity within this zone. The amount of porosity in 5754 RSW is appreciably higher than in 6111 RSW and this is reflected in the higher crack propagation rates and scatter compared to the associated wrought material.

3. A predictive unified short crack growth model was adjusted to account for the porosity found in the spot welded alloys. The adjustment showed good agreement with the predicted trend, indicating that the adjusted model can be used in industrial applications to predict short crack growth for a variety of engineering alloys.

4. Lap-shear eyebrow cracking failure does not appear influenced by the inherent porosity found in the weld fusion zone. This is related to the observation that the eyebrow crack intersects the fusion zone only at its periphery.

5. A structural stress based master fatigue life relationship for welds that fail due to eyebrow cracking was developed based on the adjusted short crack data assuming that the pore volume fraction is zero. A stress dependent initial equivalent flaw size parameter was also developed and used effectively to predict the durability of a variety of lap-shear joint geometries for both alloys.

6.2 Recommendation for Future Work

Based on the findings of this dissertation, the following recommendations are made for future research:

1. Performing SFCG experiments on the two alloys under different parameters to fully characterize the crack propagation behavior
    a. Performing testing under bending conditions instead of uniaxial tension – the lap-shear specimens undergo a significant amount of bending and thus bending testing might better distinguish the propagation behavior.
    b. Testing under different load ratios – the lap shear-specimens were tested at two different load ratios but the short crack growth rate for R = 0.1 was

applied to the R = 0.3 case. In order to distinguish any load ratio effects on the short crack propagation response additional testing is recommended.

2. Utilization of the adjustments to the unifying SFCG model, such as:
    a. Validation with different porous media including: metallic foams, alloys created via powder metallurgy or additive manufacturing, and other welds.
    b. Accounting for bending to yield more applicability to multi-axial fatigue applications. The model is predicated on the Bilby-Cottrell-Swinden (BCS) [1] model, which is related to the dislocation density at a crack tip under uniaxial tension. Thus, the unified model is only physically valid for uniaxial tension conditions.
3. 3D computed tomography to determine the presence, variability and distribution of welding defects (i.e. porosity, cracking, tearing) in the spot welded alloys. Radiographic imaging was used to evaluate the welding defects, but those 2 dimensional images are not enough to fully characterize the effect on SFCG.
4. X-ray synchrotron testing of the RSW alloys in order to better characterize the crack propagation behavior. For the RSW 5754 samples, even after adjusting for the porosity found on the fracture surface, the SFCG rates are still higher than the wrought parent material. Performing synchrotron testing and doing 3D reconstruction may produce new insight into the mechanisms of propagation with porosity.
5. Improvements to the structural stress based durability model by utilizing specimens of much more varying thickness and geometry, such as coach peel specimens, and load ratios to isolate and understand the effects of these variables on the durability model.

References

[1] Bilby BA, Cottrell AH, Swinden KH. The Spread of Plastic Yield from a Notch. Proc R Soc London 1963;272:304–14.